UNIVERSITÀ DEGLI STUDI DI NAPOLI FEDERICO II
DIPARTIMENTO DI INGEGNERIA CHIMICA

TESI DI DOTTORATO IN INGEGNERIA CHIMICA (XXI CICLO)

Physicochemical characterization of combustion generated inorganic nanoparticles

2005-2008

Francesco Carbone

Comitato Scientifico

Prof. Antonio D'Alessio - Relatore

Università degli Studi di Napoli Federico II - Dipartimento di Ingegneria Chimica

Prof. Andrea D'Anna

Università degli Studi di Napoli Federico II - Dipartimento di Ingegneria Chimica

Ing. Federico Beretta

Consiglio Nazionale delle Ricerche - Istituto di Ricerche sulla Combustione - Napoli

Ing. Christophe Allouis

Consiglio Nazionale delle Ricerche - Istituto di Ricerche sulla Combustione - Napoli

To the memory of my Professor Antonio D'Alessio,
a friend, an example and a guide.

Abstract

Combustion generated particulate matter is widely recognized to be the major pollutant in urban areas because of stationary combustor and vehicular traffic sources. Particularly the ultrafine fraction was proven to have the highest impact on human health since its ability to deeply penetrate the lung and the circulatory system. It is also the most reactive fraction, enriched in toxic condensable species, because of the large specific surface area. Up to recent times the nanometric fraction, i.e. below 10nm, was not taken in consideration, despite it is the most toxic, because it was assumed that such small particles meet and coagulate at gas kinetic rate so that their lifetime was negligible small. Some recent results on carbonaceous nanometric particles generated in laboratory flames showed that, at high temperatures, their coagulation as well their collection efficiencies drops dramatically orders of magnitude as their size decreases below 5nm. Consequently they could escape from combustors and filters and survive in the atmosphere in a not negligible amount.

It is well know that metals, present as ashes or additives into practical fuels, brought at high temperature in combustion devices, generate a large range of particulate which extend in the ultrafine range. The fraction with size smaller than 10nm of such inorganic particles was not yet studied. The measurements routinely performed at the exhaust of combustors does not extend in this size range despite it is well known that the addition of trace amount of metals into a flame causes nanoparticles formation. The objective of the research described in this thesis is to characterize such small toxic metal nanoparticles and to verify if they could be released at the exhaust of combustion systems because of coagulation and collection efficiencies following, at high temperature, the same trend of carbonaceous nanoparticles.

The thesis is composed of three main parts, roughly corresponding to the three year of the research activities. The first two chapters contains the background information on combustion generated particles and aerosol dynamic. The chapters two and three describe the experimental methodologies while the third parts contain the obtained results and their discussion.

Reactors consisting of flat laminar premixed flames doped with real fuels or toxic metal particles precursors were developed and successively investigated. They allow performing spatially resolved measurements, at several residence times in flame, of incipient inorganic nanoparticles generated in a well controlled environment. Diagnostics with high sensitivity to particles of few nanometers in size were chosen to this aim. They are on-line sampling probe high resolution Differential

Mobility Analysis and in- situ Laser Light Scattering. Particles thermophoretic collection for extra-situ Atomic Force Microscopy Analysis was widely used too.

Three main results have been obtained.

- ✓ Toxic metal nanoparticles behave quite similar to carbonaceous nanoparticles. Both their coagulation and collection efficiencies decrease by orders of magnitude with decreasing sizes below 5nm.
- ✓ The values of those efficiencies quantitatively agree between the three different generated toxic metal nanoparticles and with that of carbonaceous nanoparticles. This imply that the physic behind the nanoparticles long lifetime and rebound on surfaces is stronger influenced by size more than by chemistry.
- ✓ Flames doped with pulverized coal contain a prevalent number of particles with size lower than 10nm whose contribution to volume fraction is not negligible too. Thus combustors burning ash containing fuels may be a source of such small nanoparticles whose emission involves a not negligible pollution problem.

Table of Contents

List of Tables

List of Figures

Acknowledgments

There are many people who contributed to the production of the research activity reported in this thesis both from a scientific and a human point of view. The few words written here cannot describe how I learned from people during my PhD activities.

Among all, I have to acknowledge the Prof. Antonio D'Alessio, my scientific tutor, passed away just few months before this thesis was deposited and to whom it was dedicated. He introduced me in the field of nanoparticles research transmitting me his curiosity and need to understand. Thanks for all I learn from you and, above all, to be a friend, an example and a guide. I will never forget the time spent together for our walks and lunches, discussing about life, science and research.

Acknowledgments are also due to the other member of my scientific committee:

To Prof. Andrea D'Anna because he always addressed me towards the right scientific direction and of his precious advice. He also taught me how to overcome the involved difficulty by ourselves and that it is always possible to do more and better;

To Eng. Federico Beretta for his daily rebukes and the help in all cases of experimental and administrative emergencies. I learned by him how to be a good experimentalist and that people may be quite different to that they seem; To Eng. Christophe Allouis because he taught me that a bad start do not always imply a bad end.

I have also to thank all people of the laboratory: Rocco Pagliara, to be a friend and for his daily help in solving problems and in building the components I needed; .Mario Commodo, because it was always available in listening my problems and in giving information; Alberto Barone, for all thermophoretic samplings performed together and the AFM analysis; Andrea De Filippo and Lee Anne Sgro, for the help in using the DMAs and the hospitality which I enjoyed at the UC Berkeley; Patrizia Minutolo and Annalisa Bruno, for helpful discussion on optical diagnostics; Gianluca Lanzuolo, for his availability.

Other people of the Chemical Engineering Department and of the Consiglio Nazionale delle Ricerche contributed to my research activities and require to be acknowledged: Prof. Pierluca Maffettone, Prof. Nino Grizzuti, Prof. Gennaro Russo, PhD. Fabio Montagnaro, PhD. Francesco Di Natale, Doct. Luciana Lisi, Rosalba Barbella, Sabato Russo, Massimo Urciolo, Antonio Cammarota, Vito Stanzione, Andrea Bizzarro, my PhD students colleagues and many others that I apologize to miss.

Thanks are due to my graduate students particularly to Umberto Gammieri, Massimo Iovane, Salvatore Grimaldi, Fabio Brando and Valeria Capasso because of their help in performing measurements during their thesis work and to my friends because they were whenever I needed.

I also acknowledge my Professors Carlo Meola, Renato Fiorenza and Beatrice Lignola and PhD. Gennaro Coppola because of all I learned from them and of their advices and continuous encouragements in performing the research activity. I feel a sincere esteem and affection towards them.

Finally I have to thanks my family because of their daily moral and economical support. They helped me in following my crazy passion for the scientific research.

Chapter 1

Combustion generated Atmospheric Particles

1.1 Introduction

The earth atmosphere is the complex system surrounding our planet and greatly influencing the establishment and persistence of life. It consists of a gaseous mixture, trapped by gravitational force and commonly labeled *air* for the *troposphere*[1], in which particles and droplets of several sizes and chemical compositions are naturally dispersed or suspended. This *Particulate Matter* (PM) may be generated and transformed into the atmosphere itself consequently to random, sudden or periodic, i.e. daily or seasonal, physical condition changing, such as temperature, humidity, composition and sun radiance. This is the case of cloud formation and rain cycles. Another fraction of PM originates from atmosphere direct interaction with the earth crust because of volcanic eruptions, spontaneous fires, rock erosion and dust, sea sprays and biological matter transport by wind.

Human activities may perturb the natural earth atmosphere equilibrium, on local or global scales, modifying both its gaseous composition and the amount and characteristics of suspended matter. This environmental problem, commonly labeled *air pollution*, is worldwide recognized and it could involve immediate and long term effects on favorable conditions to life, mainly because of pollutant toxicity and influence on climate change. Many countries legislatures, individually or jointly, are committed in defining *pollutant emissions limits* and *air quality standards* in order to restrict potential pollution dangerous consequences. The main air pollutant source is fossil fuel combustion related to some fundamental activities influencing human welfare such as energy generation, urban and industrial heating and transports, whose demand was exponentially growth during the last decades because of emerging countries developing, principally China and India.

Combustion of fossil fuel, containing mainly hydrocarbons, involves the emission of pollutant species also in ideal condition, at least because of *carbon dioxide* (CO_2) production. This gas is naturally contained into the earth atmosphere in average volume concentration of ~380ppm and it is not toxic up to 0.5%÷3% concentrations, depending on exposure time. Nevertheless carbon dioxide is one of the main *greenhouse gases*, together with *water* (H_2O) and *ozone* (O_3), and its concentration greatly influences the earth atmosphere radiative balance and, then, temperature. For this reason the observed increase of carbon dioxide atmospheric content in the last two century, since the industrial revolution and the wide employ of fossil fuels combustion, is believed the main responsible for the simultaneous earth overheating. This problem is so accepted and worrying that almost every country in the world, with the exception of United States and some minor nations, had signed and ratified the Kyoto protocol limiting the total carbon dioxide worldwide annual emission and consequently the fossil fuel consumption. Some attempts to store combustion generated CO_2 at the exhaust were performed to solve this problem. Unfortunately, this approach requires very expensive gas separator apparatus, also lowering the global efficiency of plants, or the use of not yet well developed oxy-combustion technologies.

Depending on the fossil fuel type, especially on its composition, and on the combustion condition, at least other three categories of combustion generated pollutant have to be considered: other gaseous species, carbonaceous particles (*soot*) and inorganic aerosols. The main classes of gaseous pollutants are *sulfur oxides* (SO_x), *nitric oxides* (NO_x), *carbon monoxide* (CO) and *volatile organic compounds* (VOC). The formers two have also an influence on particle nucleation in the atmosphere and on acid rains. The VOC, like carbon monoxide, originates in fuel rich conditions because of not complete hydrocarbon oxidation and it includes a large class of compounds. They range from simple *unburnt hydrocarbons* (HC), consisting of 1 to 6 carbon atoms, to *polycyclic aromatic hydrocarbons*

---

[1] The *troposphere* is the atmosphere layer closest to earth surface whose average deep is ~10km. Most of the information given in this chapter, concern this layer. The outer earth atmosphere layers are *stratosphere*, *mesosphere* and *ionosphere* accounting for the subsequent ~35km, ~40km and ~600km of its thickness, respectively.

(PAHs), already contained in the fuel or generated by the fuel oxidative pyrolysis (the most toxic and representative PAH is benzo(a)pyrene), up to complex organic structures including heteroatoms like oxygen, nitrogen, sulfur, chlorine or metals. Among these compounds, particular attention, especially from waste incineration, is due to *polychlorinated dibenzodioxins* (PCDD) and *polychlorinated dibenzofurans* (PCDF), commonly known as *dioxins* and *furan*s, because of their extremely high toxicity. It is possible to reduce gaseous pollutant emission adding exhaust aftertreatment, such as scrubbers and catalysts.

Progressively more complex and less volatile carbonaceous structure form with the increase of fuel to oxidant molar ratio beyond the stoichiomentric value, i.e. *equivalence ratio* (Φ) beyond one. This complex growth continues up to particles inception that take place also burning very clean fuels such as natural gas or light hydrocarbons, when the equivalence ratio exceed a critical threshold depending on the fuel itself. The surface of these particles may enrich, at lower temperature in the exhaust, with some toxic condensable species, particularly VOC and, if present, metallic compounds. Combustion generated carbonaceous particles with size larger than 10nm are worldwide labeled *soot* and their thermal radiation is responsible for yellow light emitted by sooting flames such as a burning candle. The flame local equivalence ratio always exceed the sooting threshold when fuel is not premixed with oxidizer and, sometimes, because of not perfect mixing, also when the overall equivalence ratio is lower than one. This is the case for a great number of real combustors, at least not premixed ones and that employing liquid and solid fuels. They are responsible of not negligible soot emissions (Bockhorn et al., 2008).

Inorganic particles are generated at high temperature anytime the fuel contains elements whose oxidation products are not volatile, mainly metallic compounds and minerals. This matter may undergo several physical and chemical transformations in the combustion chamber, but it is released as solid or liquid, substantially in the same amount. *Bottom* and *volatile ashes* are the terms commonly used to indicate the fractions of this matter that deposits in the combustor itself and that is emitted at the stack with the exhaust gasses, respectively (Linak and Wendt, 1993). Thus the formation of inorganic aerosol is almost unavoidable burning ashes containing fuels, such as coal, biomass, waste or crude oils. This class of fuels is the most employed for electrical power generation and this problem is involved also adding metal containing additives into hydrocarbons fuels.

Both carbonaceous and inorganic aerosols emissions may be reduced using filtering devices, such as scrubbers, cyclone separators, fabric collectors and electrostatic precipitators. Unfortunately the filtering efficiency of these equipments decreases with decreasing particles sizes, particularly below 100nm (Zhuang et al., 2000). Many research efforts have been spent to gain deeper inside in particles inception in order to develop combustion technology able to reduce particles production itself. In any case, there is not a definitive theory on the gas/liquid to particle transition and the only evidence is that such transition occurs on nanometric length scales.

1.2 Atmospheric Particles

One of most important parameter in considering atmospheric particulate is their lifetime also influencing the distance that PM can be carried from its source. The time required for particulate to vanish depends on removal mechanisms. The main of these processes is inertial settling because of gravitational force. A simple force balance on particles, assuming spherical shape, conducts to calculate a sedimentation velocity proportional to the square of diameter. Particle lifetime in the atmosphere, being inversely proportional to this velocity, depends on the reciprocal of the square of diameter.

Another particles removal mechanism is their growth, via coagulation, surface reaction or condensation, causing disappearing of the particulate smallest fraction. This process, discussed in the next chapter, is prevalent for submicrometric particles, having too slow sedimentation velocity and it is also strongly influenced by particles size. Rain could be seen as the result of these two processes and constitutes itself a way to remove atmospheric particulate by the *rain out* and the *wash out* mechanisms. The former take place when particulate provides cloud condensation nuclei, the latter when particulate was captured by already formed water droplets.

Particles size is the first of parameters that have to be considered in order to determine particulate lifetime and, more generally, PM behavior and sources. Another parameter to be considered, at least to have an indication on PM source, is particles chemical composition (Hinds, 1999).

1.2.1 Classification

The total amount of substances suspended or dispersed in air, both solid and liquid, is commonly labeled *total suspended particulate matter* (TSP), or simply PM, and it may be ***natural*** or ***anthropogenic***. Both kind of PM are classified in:

- ✓ ***Primary*** particulate, released in the atmosphere in the same physical, chemical and morphological status they are generated by the source;
- ✓ ***Secondary*** particulate, generated in the atmosphere itself, mainly from nitrates and sulfates.

Apart from these two rough but fundamental classifications, there are many others considering both sizes, concentration, source, chemical and physical nature of PM. This thesis is mainly focused on *aerosols*. This term generally indicates the mixture of particles and droplets, with sizes smaller than 1μm and concentration less than 100ppm, with the gas, usually air, in which they are suspended. For this reason often the term particles is used to label both solid and liquid particulate. Aerosol bulk properties, such as density and viscosity, are normally assumed equal to that of pure gas because of very low particles concentration values. The most practical PM classification is based on particles size. The *equivalent aerodynamic diameter*[2] is usually used in defining particles size. Several PM fractions are generally identified:

- ✓ ***Coarse particles***, having diameters larger than 2.5μm.
- ✓ **PM_{10}**, particles smaller than 10μm, also labeled *thoracic fraction*;
- ✓ **$PM_{2.5}$** or ***fine particles***, smaller than 2.5μm, also labeled *respirable fraction*;
- ✓ **$PM_{0.1.}$** or ***ultrafine particles***, the PM fraction with sizes smaller than 100nm;
- ✓ **Nanoparticles** or **Hyperfine particles**, up to 10nm in diameter.

---

[2] The particle equivalent aerodynamic diameter is the diameter of a unit density sphere moving in a gas like the particle itself.

The fractions identified in that way, roughly correspond to several mode of the particles size distribution usually observed in urban areas and shown in Figure 1.

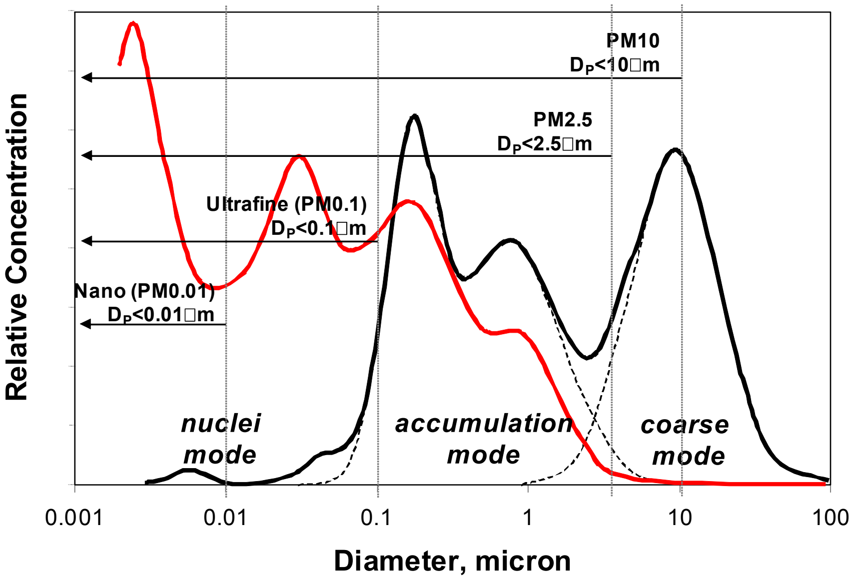

Figure 1 – Typical size distribution of atmospheric particles in urban areas (black: mass concentration, red: number concentration) (D’Anna, 2008).

The ultrafine fraction comprises the *nucleation modes* whose name depends on the origin of this class of particles. They are mainly due to particles inception from the vapor phase, directly in the atmosphere or because of human activities, mainly combustion. Their lifetime is commonly believed to be very short because of their fast growth. Indeed, their small mass involves an intense Brownian motion and, then, a high collision frequency causing their fast coagulation into larger structures. Consequently they represent a negligible percentage in mass of TSP but they still are the most abundant in number because of their small volume. Moreover, D’Alessio et al. (2005) showed that flame generated carbonaceous nanoparticles may have a coagulation efficiency order of magnitude lower than unity and, consequently, lifetimes and concentrations in atmosphere much longer and higher than expected, respectively.

The *accumulation modes* include fine particles whose sizes involve very long lifetime because both coagulation and inertial settling are very slow. Therefore this class of particles tends to accumulate in the atmosphere and to represent a significant amount of PM both in mass and in number. They mainly originate from smaller particles growth into the atmosphere itself or at the source itself.

The *coarse mode* is substantially composed of coarse particles having a short lifetime in air because of their fast sedimentation. They have mainly natural origin, but some of them may be generated by growth of smaller particles or by some human activities involving dust generation (Hinds, 1999).

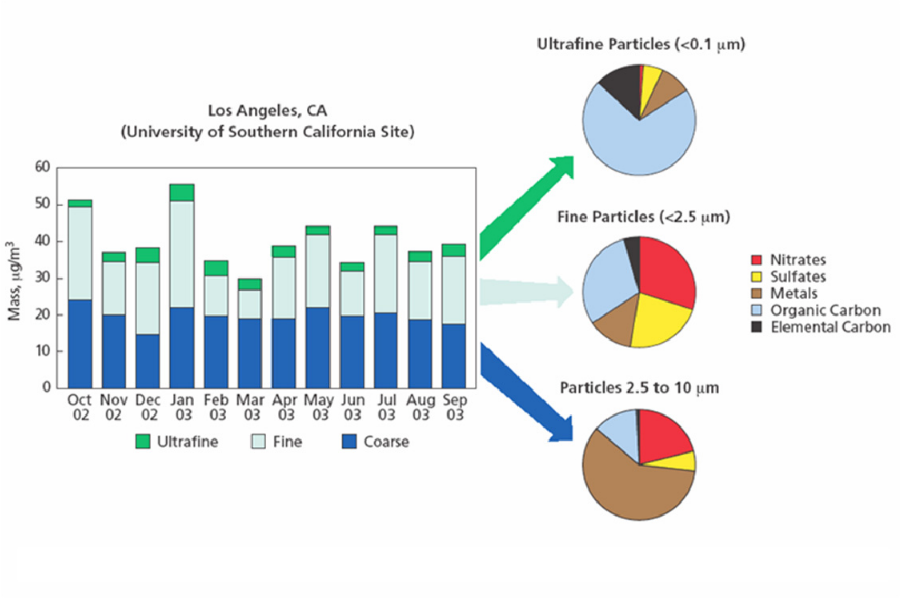

Figure 2 - Mass concentration and chemical composition of ultrafine, fine and coarse particles (EPA, 2004).

Carbonaceous particles are mainly generated by combustion, while the most part of geological PM is inorganic. Thus PM chemical composition changes with geographical collocation. The main trend is the increase of the carbonaceous fraction moving from remote to urban areas. This trend is due to anthropogenic sources, mainly combustion. Figure

2 show the mass concentration and the composition of ultrafine, fine and coarse particles in an urban area. Carbonaceous PM is much more abundant with decreasing of particles sizes. Therefore combustion generated particles are mainly fine and ultrafine.

1.2.2 Human health and environmental effects

Since the early nineties in the United States were conducted epidemiological studies highlighting the relationship between the high PM_{10} concentrations and the increase of respiratory and cardiac diseases. More recent toxicological studies showed both chronic and acute effects of PM inhalation. Acute effects are asthma, bronchitis, pleurisy, vascular disorder, increase in heart beats and cardiac infarction. Chronic diseases, such as chronic bronchitis, pulmonary emphysema, pneumonia and lung cancer, are associated with long exposure time (Kennedy, 2007). The PM effects may be increased by toxic substances like some metals, such as Pb, Hg, Cr, Cd, Ni and As, and VOC that could enrich particles surface or form particles themselves.

Once again particles size is a very important parameter in determining their toxicity (Oberdorster, 2000). Indeed, coarse particles are barred from the first airways, i.e. nose and pharynx, while the smaller ones can reach the lungs, thus the label thoracic and respirable fraction for PM_{10} and $PM_{2.5}$, respectively. The body is able to remove extraneous material but that removal is never complete and involve inflammation response. Ultrafine particles may also penetrate the lungs epithelial cells reaching, transported by blood, other organs such as spleen, liver and heart. They could also infiltrate inside cells, depending on their size, shape and surface composition, directly producing mitochondrial damage or DNA modification. In some cases the particles are able to reach directly the brain through the olfactory nerves.

Ultrafine particulates, based on mass concentration, has by far the most dramatic impact on human health because of its high specific surface and capacity to cross the tissues than larger particles (Oberdorster, 2005). Moreover, it represents the fraction more enriched in surface with volatile toxic substances enhancing their red-ox activity. Recent studies show that PM health impact increases with reducing of particles sizes and it is proportional to their numerical concentration rather than mass concentration. Brown et al.

(2001) showed that even ultrafine particles of not toxic materials, such as polystyrene, play a pro-inflammatory activity.

The main environmental effects regard flora, fauna, visibility and climate change. Particles interaction is similar with any kind of cell, thus animals may suffer effects similar to that on men. Moreover, PM may hinder the photosynthesis irreversibly damaging vegetation. The most alarming environmental effects are on climate change (Jacobson, 2001). Indeed, particles are able to modify both local and global earth radiative balance because they change the atmosphere optical properties and promote cloud and fog formation. They also involve visibility decay because of the same reason. The particulate overall effect could be the earth average temperature lowering, mitigating the greenhouse effect. Anyway, PM perturbs the delicate earth climate equilibrium.

1.2.3 Air quality regulation and guidelines

The European Commission has set limits for PM_{10} and other pollutants in urban air with directives 1999/30/CE and 96/62/CE. Some limit values were reported in Table 1.

Table 1 – **European Union pollutant limits value for air quality.**

Pollutant	Averaging time	Limit value	Allowed annual day exceeding limit value	Entering in force from
PM_{10} phase 1	Annual	40 $\mu g/m^3$	35 day	January 2005
PM_{10} phase 1	24h	50 $\mu g/m^3$	-	January 2005
PM_{10} phase 2	Annual	20 $\mu g/m^3$	7 day	January 2010
PM_{10} phase 2	24h	50 $\mu g/m^3$	-	January 2010
Pb	Annual	0.5 $\mu g/m^3$	-	January 2005

The directive 2004/107/CE also quantifies the goal values for the total content of PM_{10} fraction, on annual average, of particular toxic compounds, mainly metals: Arsenic (6ng/m^3); Cadmium (5ng/m^3); Nickel (20 ng/m^3); Benzo(a)pyrene (1ng/m^3); Mercury.

At present the European Commission is looking forward to introduce limit values also for $PM_{2.5}$ that could enter in force in the period from 2010 to 2020, because of the observed higher health impact of fine particles respect to larger ones. From this point of view the United States is in the forefront.

The Environmental Protection Agency (EPA) set standards for both PM_{10} and $PM_{2.5}$ concentrations with the Clean Air Act (Title 40 of the Code of Federal Regulations). The pollutants limit values, some of which were reported in Table 2, are completely listed in the National Ambient Air Quality Standards (NAAQS), Part 50 of the Clean Air Act.

Table 2 – **United States National Ambient Air Quality Standards.**

Pollutant	PM_{10}	$PM_{2.50}$	$PM_{2.5}$	Pb
Averaging time	24h	24h	Annual	Annual
Standard	150 $\mu g/m^3$	35 $\mu g/m^3$	15 $\mu g/m^3$	1.5 $\mu g/m^3$

The emissions of Hazardous Air Pollutant species (HAPs) are also regulated in Part 61 and 63 of the Clean Air Act. Such National Emissions Standards for Hazardous Air Pollutants (NESHAP) involves metals contained in fuels, particularly As, Be, Cd, Co, Cr, Hg, Ni, Mn, Pb, Sb and Se, and many organic compounds.

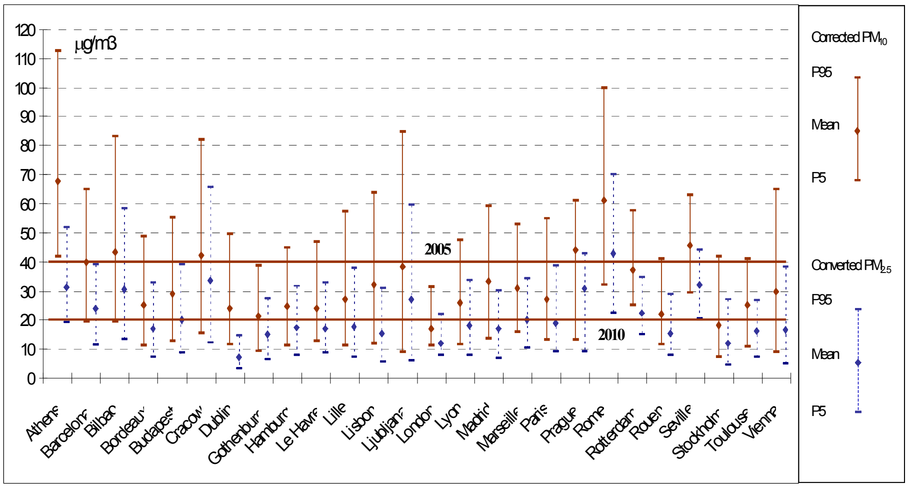

Figure 3 - Annual mean levels, 5th and 95th percentiles of the PM_{10} and $PM_{2.5}$ distributions (horizontal solid lines represent phase 1 and phase 2 of EC directives on PM_{10} limits) (APHEIS, 2006).

Figure 3 and Figure 4 show, for several European cities, the annual mean levels, the fifth and the ninety-fifth percentiles of the PM_{10} and $PM_{2.5}$ distributions and a plot of the number of days, during the year, in which the PM_{10} concentration exceed the 24h limit values, respectively.

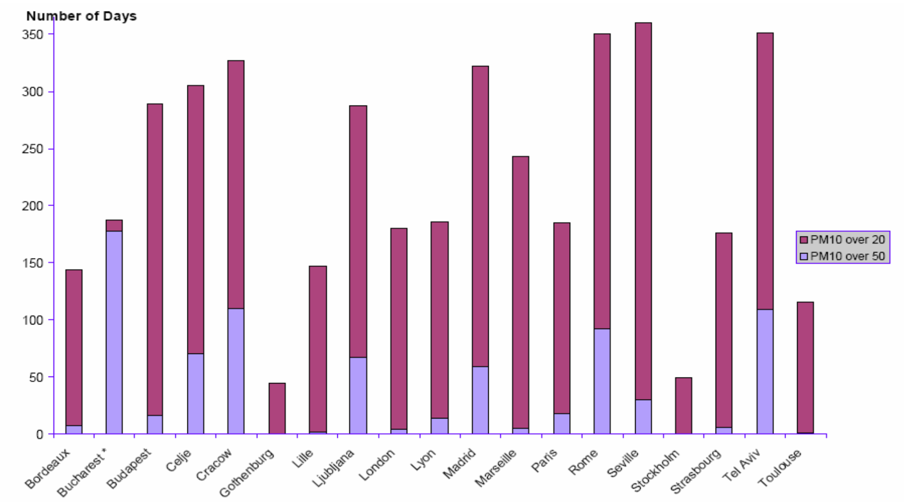

** For Bucharest, measurements were only available for four weekdays (Monday to Thursday).*

Figure 4 – Annual number of day in which PM_{10} concentration exceeds limit values in several European cities (blue PM_{10} over $50\mu g/m^3$, red PM_{10} over $20\mu g/m^3$) (APHEIS, 2001).

In many cities the PM_{10} mean annual value is over the limits and also $PM_{2.5}$ fraction alone exceeds the phase 2 of the European directive. Moreover the number of out of limits days is well beyond that allowed, both by phase 1 and phase 2 regulations. Considering the percentage increase of carbonaceous PM in urban areas, it results clear that such situation depends on traffic emissions and stationary urban combustion sources. Currently, the combustion generated fine and ultrafine fractions of PM are widely recognized as the mayor urban areas pollutant.

1.3 Combustion generated Particles

Stationary combustion devices such as boiler and furnaces, burning coal, fuel oil, petroleum based fuels, gaseous and liquid hydrocarbons, biomass and waste, and internal combustion (IC) engines, burning both gasoline and diesel, are significant sources of primary PM in urban areas. Valuable papers written by Linak et al. (2007), Quann and Sarofim (1982), Sarofim et al. (1977) studied particulate from coal combustion while Lee et al. (2006) and Wiinikka et al (2006) characterized particles generated in diesel engine and from wood pellet combustion, respectively.

Combustion generated particles are generally smaller than geologically produced dust and have unique chemical composition and morphology. They range from millimeter sized cinders and soot aggregates to ultrafine nucleation mode particles, only a few nanometers in diameter. The largest particles are collected in the combustor itself, as bottom ash or wall deposits. The remaining part is effectively removed from exhaust gas by after treatment devices, while the ultrafine fractions can be emitted at the stack contributing to ambient air pollution on both urban and regional scales (Lighty et al., 2000).

Combustion systems generally emit three classes of primary particles, two generating at high flame temperature and another at low exhaust temperature. The latter category includes particles of condensable organic and inorganic species, volatile at flame temperature, that homogenously or heterogeneously nucleate from vapor phase because of exhaust gas cooling. The total amount of this condensing matter may be quite well described with a thermodynamic approach but a detailed discussion on this topic is beyond the aim of this thesis.

The two particles classes, originating at flame temperatures, are inorganic, mainly metallic compounds and silicates, and carbonaceous particles (soot). The inorganic particulate both nucleates from gaseous phase and may be some residuals of fuel burning. Anyway, for the latter fraction, the thermodynamic approach may only describe particle nucleation but it is usually not effective in predicting the condensing gas mixture composition (Linak and Wendt, 1993). Finally, a detailed chemical kinetic model is always required to describe both carbonaceous particles inception and the total soot yield (Bockhorn, 2004).

1.3.1 Carbonaceous Particles and Soot

Fundamentally two kind of carbon arrangement may be recognized in combustion generated and atmospheric carbonaceous particles:

- ✓ ***Elemental Carbon*** (*EC*) or *Black Carbon*, graphitic hexagonal structure;
- ✓ ***Organic Carbon*** (*OC*), larger number of bond with hydrogen or oxygen.

The former is always observed for combustion generated carbonaceous primary particles larger than 10-20nm, commonly labeled *soot*. The latter has higher health impact effects and it is typical of condensable species that may enrich soot surface or form secondary particles itself, in the exhaust gas or in the atmosphere (Lighty et al., 2000).

D'Alessio et al. (1992; 1998) showed that OC may also generate particles smaller than 5nm at high flame temperatures. Such Nanosized Organic Carbon (NOC) might play a role as soot intermediate and its emission from combustion device could account for the large amount of not yet chemically identified atmospheric OC ultrafine particulate.

Unlike other matter, for which thermodynamic nucleation theories may predict the phase transition condition, combustion generated carbonaceous structures are defined to be particles when they are capable to be measured. The smallest ones that have been observed are in the range between 1nm and 2nm and thus contain about a hundred carbon atoms (Dobbins and Subramaniasivam, 1994).

Carbonaceous primary particles are produced in flames by a sequence of chemical reactions, some of which are essentially irreversible, anytime the local equivalence ratio exceeds a critical value depending on burning fuel. In such condition, hydrocarbon fragments, generated by fuel oxidative pyrolysis, have a greater probability of colliding with other hydrocarbon fragments, rather than being oxidized (Haynes and Wagner, 1981). Thus they generate clusters of increasing molecular weight that grow up to the measurable size range. Clearly, fuels composed by heavier hydrocarbon and with higher condensable aromatic or graphitic structures content, have a higher tendency to generate such carbonaceous particles (Bockhorn et al., 2008).

The kinetic models describing carbonaceous particles inception are not definitive despite large research effort have been spent on this topic. Some models proposed flame positive ions as the initial nuclei sites for particles formation but it is widely accepted only that the PAHs play a fundamental role in particles nucleation and that, for non aromatic fuels, the first aromatic ring formation, usually benzene, is a critical step (Bockhorn, 1994). Models mainly assume that hydrocarbons molecular weight growth may follow two parallel pathways. The former involve Hydrogen Abstraction and aCetylene Addition (HACA mechanism) and it is also effective in describing subsequent soot surface growth. The latter assume PAHs polymerization by means of Resonantly Stabilized Free Radicals (RSFR mechanism, Miller and Melius, 1992) and it is also able to explain the NOC nucleation (D'Anna et al., 2001).

Carbonaceous particles, once nucleated, may suffer the same physical evolutions of other classes of particles, such as coagulation and surface condensation. Nevertheless it is not possible to neglect that they contemporaneously suffer some peculiar chemical interrelated processes. They are: internal structure rearrangement, such as graphitization; surface growth and surface oxidation. The former could explain how NOC, whose structure is not fully characterized, can be involved as intermediate in soot formation (D'Anna, 2008). The latter two were widely described in the large amount of literature on soot itself (Bockhorn et al., 2008). Often, the surface growth is modeled with HACA mechanisms while semi empirical kinetic formulas account for soot oxidation (Park and Appleton, 1973). Soot is generally the final product of such physical and chemical transformations, schematically showed in the left side of Figure 5.

Right side of Figure 5 show a microscopy image of thermophoretically sampled soot. It is normally a micron sized aggregate of hundred or thousand of primary particles with mean size between 10nm and 30nm. Each primary particle is composed by randomly disposed subunit of four or five layered graphitic like clusters, containing hundreds of carbon atoms arranged in a *turbostratic*[3] structure. The hydrogen content may commonly vary from a third down to an eighth depending on soot aging. Other elements, such as oxygen, sulfur and nitrogen, may be included in soot structure and some compounds, mainly VOC or metals, may adsorb on its surface, greatly depending on fuel composition and combustion device configuration.

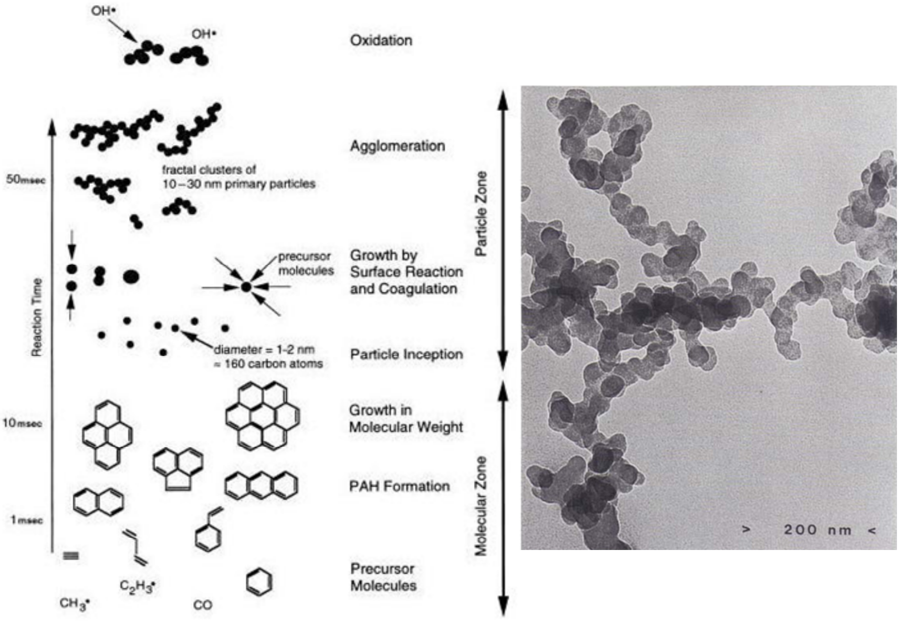

Figure 5 – Left side: Scheme of soot formation process (Bockhorn, 1994); Right side: TEM image of a soot aggregate (Dobbins and Subramaniasivam, 1994).

1.3.2 Inorganic Particles

Also in ideal condition, the major part of not gaseous inorganic matter, mainly metals and minerals, entering in a combustion device, exit the combustor, after suffering several physical and chemical transformations at high temperature, in solid or liquid state as particles with size comprised from few nanometers up to some millimeters. In many case a simple material balance provides a good assessment of the total amount of such *ashes* (Linak and Wendt, 1993). The fraction with largest sizes settles in the combustor itself, from which it has to be removed, and correspond to the *bottom ashes* while the remaining smaller particles, labeled *volatile ashes*, are carried away by exhaust gasses. The physical form in which inorganic matter enters in combustion chamber greatly influences their ultimate fate and it strongly depends on both the used fuel and the combustion device configuration.

[3] A type of crystalline structure where the basal planes have slipped sideways relative to each other, causing

Moreover the evolution of inorganic matter is always coupled with that of carbonaceous matter (Lighty et al, 2000).

Inorganic matter may be contained in both liquid and solid fuels essentially in three forms: inherent, included and excluded. *Inherent inorganic matter* is that chemically bounded to the organic fuel matrix such as, in the case of metals, organo-metallic complexes or ion exchanged metals bound to the organic acids. The mineral crystallites, mainly clays, pyrites and quartz, dispersed within the fuel compose the i*ncluded inorganic matter* while that completely extraneous to the fuel and contained in self staying particles or droplets represent *excluded mineral matter*. Some salts, such as nitrates and pyrites, may dissolve in the fuel itself or in water, if present such as happens for waste incineration, and they violently decompose or viscously melt at high temperature, (Linak and Wendt, 1993). Inorganic matter, not already contained in the fuel, may also be added in reacting mixture both voluntary, as fuel additive, and not voluntary for example because of lubricant infiltration in the combustion chamber (Lee et al., 2006).

The main inorganic particles formation pathways are essentially two in spite of global process complexity: the residual ash and the vaporization-nucleation pathways (Linak and Wendt, 1993). They are schematically represented in Figure 6 and each of the two may be a route to both submicron and supermicron particles generation.

The *residual ash* is the material remaining in a solid or liquid phase throughout all the combustion process. It is clear that, in not ideal condition and depending on combustion efficiency, also carbonaceous particles may be generated in this way because of liquid or solid fuels incomplete oxidation generating *char*[4] residuals (Tognotti et al., 1991a). The residual ash formation pathway leads to formation of both dense and porous particles with crystalline or glassy structures. In addition low density *cenosphere* or *plerosphere*[5], with size up to hundreds of microns, may form when ash viscosity is enough to entrap generating gasses but not so high to hidden bubble growth.

---

the spacing between planes to be greater than ideal.

[4] Char is the solid material remaining after light gases and tar have been driven out from carbonaceous material. Carbonization, charring, devolatilization and pyrolysis are the term used to label the char formation process and taking place during the initial stage of liquid and solid fuels combustion because of local oxygen deficiency.

[5] Cenospheres are hollow ash particles and plerospheres are cenosphere surrounding other ash particles.

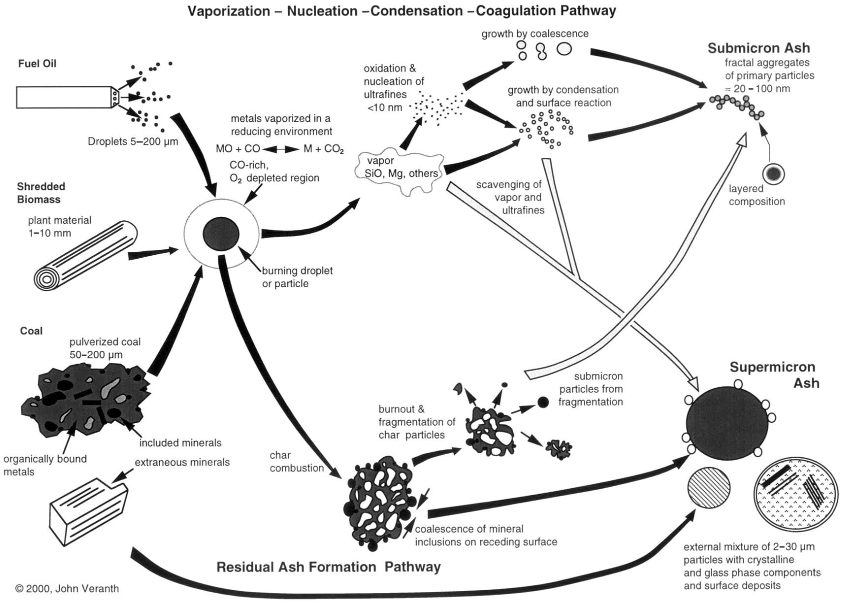

Figure 6 – Scheme of inorganic particles formation pathways (Lighty et al., 2000).

The residual ash particles preferentially have sizes comparable to that of fed fuel, usually in the supermicron range, and they depend both on fuel ash content and on generated ash particles density. The reason of analogous sizes between fed and produced matter is evident for excluded minerals. Moreover, the included minerals may adhere on char or fuel surface and coalesce whit other inclusion while that surface recede because of oxidation. Also the inherent ash can meet that inclusions while diffusing in the fuel matrix and form stable bound with them (Lighty et al, 2000).

The other process determining residual ash sizes is fragmentation. Fuel or char bursting may occur during its oxidation and fragmentation could also directly interest ash particles because of attrition or cenosphere explosion. Many semi empirical models have been developed to describe such process, strongly depending on particles porosity (Kang et al., 1988). Obviously more extensive is fragmentation smaller will be generated particles. Therefore residual ash pathway may also contribute to submicron particles formation.

Submicron ash particle, usually refractory and alkali metals oxides, are preferentially formed following the vaporization nucleation mechanism. It involves all liquid or solid inorganic matter, mainly the metals content of ashes, that pass through the gas phase in the combustor but that is not volatile, thus in the form of particles, at exhaust low temperatures. This matter, in the form of vapor or submicron particles, may also be scavenged both by carbonaceous particles and by larger residual ash because of surface condensation and adhesion, respectively. Soils can also play a role in the adsorption of contaminants (Tognotti, 1991b). Moreover vaporized metals may react on surface of existing particles attaching on it also when their partial pressure do not exceed their vapor pressure. Thus the vaporization nucleation pathway may also contribute to supermicron particles yield.

The physicochemical transformations, occurring to matter following vaporization nucleation pathway, may be quite complex despite the global process conceptual simplicity. These transformations are usually coupled and kinetically controlled and the overall amount of nucleating particles may have little to do with equilibrium. Fortunately the time for the nucleation is small relative to the following particles dynamic (Flagan and Friedlander, 1978) and the final produced particles are only slightly influenced by the details of the early nucleation.

Some inorganic elements, such as Hg, Na, Ca, S and Pb, are volatile and thus vaporize at combustion temperature both when they are included and when they are excluded. Once in the gas phase they can react to form unvolatile oxides or other unvolatile compounds that suddenly nucleates forming tiny particles. They can also survive oxidizing post flame environment as a vapor and successively nucleate or condense on existing particles with the lowering of temperature moving toward the exhaust. The prevalence of nucleation versus surface condensation is greatly influenced by exhaust gasses cooling rate. This simple case may be well described with a thermodynamic approach (Linak and Wendt, 1993).

Other included refractory compounds such as SiO_2, Al_2O_3, CaO, MgO and FeO, being unvolatile at flame temperature, may also be released in gas phase because they are reduced to volatile suboxides (eventually pure metal) in the CO rich, reducing boundary layer that forms close to the burning fuel or char. Once diffused away such boundary layer they undergo the same fate of volatile species mainly being re-oxidized and converted in particles

(Quann and Sarofim, 1982). Clearly such refractory oxides are usually unable to vaporize when are contained in the extraneous minerals.

The presence of some compounds, above all chlorine that can never be neglected, may kinetically influence the vaporization process because they could react with other species involving the formation of more volatile complexes. Moreover some elements that are stably bond, also at high flame temperatures, in an included or excluded mineral structure, may be displaced by another element causing their vaporization. An example is the potassium contained into illite that is displaced by sodium. Finally the release of inherent matter in vapor phase involves complicated chemistry always coupled with that of fuel or char oxidation (Linak and Wendt, 1993).

The transition to vapor phase that define the amount of inorganic matter following the vaporization nucleation pathway, is generally extremely complex and it is just quickly described in this descriptive paragraph. A large amount of literature was produced on this topic. The combustion generated ultrafine inorganic particles are almost completely formed it this way. Once determined the amount and composition of vaporized matter homogeneous and heterogeneous nucleation theory can predict particles inception. Their evolution, together with that of carbonaceous, residual ash and sorbent particles, is determined by coagulation, coalescence, condensation and, if effective, surface reactions. These processes determine the final fate of such vaporized matter, its partitioning between coarse and fine modes and are described in the chapter two.

1.3.3 Fuel effects

Coals, also when pulverized and scavenged and whatever its quality, i.e. anthracite, bituminous, sub- bituminous, lignite and peat, always contain, in addition to sulfur, doses of metals such as Si, Al, Fe, Ca, K, Na, Mg, Ti, Ni, Cr, Zr, Sn, Cu, Mn, Cd, Pb, Hg and As, in a larger amount compared to high oil derivatives. Inorganic matter partitioning between bottom ashes, mainly allumino silicates, and volatile ashes may vary greatly depending on combustor configuration. For coals, the ashes content usually constitutes ~10% on average of the mass. For petroleum, the maximum inorganic mass ranges from 0.05% for a light

No. 4 oil to 0.15% for a No. 5 fuel oil; a typical value No. 6 or residual oil ash content is 0.8% (Lighty et al., 2000).

Representative ash content for biomass is 2.5%, but it varies widely. The latter always have a higher content, up to 30% of total ashes, of alkali metals respect to fossil fuels, particularly potassium, mainly contributing to submicron particle fraction. The supermicron particles generated by biomass combustion mainly contain calcium (Lighty et al., 2000).

Finally, ash content of waste is usually higher than that of fossil fuels. It may vary greatly both in composition and in physical status, depending on the nature of waste itself and on how it is fed in the combustor. Waste may contain water where are dissolved some metals salts such as nitrate and the chlorine content may never be neglected. The latter is of great importance both for metal vaporization and for dioxins and furans formation (Linak and Wendt, 1993).

Chapter 2

Aerosol Dynamic fundamentals

2.1 Particles synthesis in flames

The process conducting to the formation of fine particles in combustion device from gases are generally grouped into the flame aerosol dynamic topic. The flame aerosol technology focuses on methods to control particles formation in combustors. Nearly every flame produces particles as described in the chapter one. They are sometimes quite visible and obvious such in a sooting flame, but often nearly invisible. In many case flames appear to be particle free because our eyes, or the used diagnostics, are not sensitive or specific enough to detect them (Roth, 2007). The combustion community has learned, from a long time, to consider flames not only as a reactive flow with internal energy transfer, but also as reactors producing many unwanted gaseous and particulate pollutants. Many research efforts have been spent to understand the mechanism conducting to particles formation in combustor in order to develop combustion technology involving lower emission of such pollutant particulate matter (Lighty et al., 2000).

From another point of view, flames may be seen as cheap reactors to synthesize particles or powders with desired physical properties. This approach is also the historically oldest since the carbon black production in flames, to prepare inks, can be dated back to the ancient China (Ulrich, 1984). The interest in powder or particles production has largely increased during the last decades because of their wide industrial application. Today, flame technology is employed routinely in large scale manufacture of carbon blacks and ceramic commodities such as fumed silica and pigmentary titania and, to a lesser extent, for specialty chemicals such as zinc oxide and alumina powders. These powders find most of their applications as pigments, reinforcing agents and in the manufacture of optical waveguides, opacities, catalysts, flowing aids, cosmetics products and telecommunication and electronic devices (Pratsinis, 1998). The interest in functional nanoparticles is growing with the diffusion of nanotechnology. The reason for the size effects exhibited by nanoparticles compared to the bulk matter, is their large surface to volume ratio. For a particle of about 4 nm, half of the molecules forming the nanostructure are actually at the surface with consequences for the lattice structure. This causes dramatic changes in the physical and chemical properties compared to the bulk material and changes, e.g., the melting temperature, the mechanical properties, the band gap for semiconducting particles, the magnetic or the optical properties, as well as the catalytic behavior (Roth, 2007).

Among other technique, flame synthesis is the wider used because it is cost-effective and versatile but it is also very difficult to control because particle inception and growth take place extremely fast. The interest in the cheap synthesis of ultrafine or nanoparticles has renewed the research activity on flame aerosol reactors. Many researchers such as Pratsinis (1998), Woldridge (1998), Madler et al. (2002), Stark and Pratsinis (2002), Rosner (2005) and Roth (2007) provided exhaustive reviews on particles synthesis in flames.

The process involved in particles formation, schematically showed in Figure 7, are almost the same both when particles are desirable combustion product and when they are unwanted pollutant particulate matter. The main difference is that powder production is performed in well controlled condition, in term of mixing of the reactants and particles precursors, overall composition and time temperature behavior while pollutant particulate matter formation is heavily influenced by the fuel physical and chemical structure and on combustor configurations that have to primarily satisfy criteria for space, economy and energy release efficiency.

The particles formation starts with some precursor release in vapor phase undergoing chemical decompositions or reactions. Such chemical kinetics can also interact with the kinetics of combustion, e.g., via radical reactions, and it strongly depends on the specific case. Radicals, intermediates and product molecules are formed. The latter may polymerize or nucleate to the form first nuclei clusters. The clusters grow because of both molecular addition on surface and their intense Brownian collision, resulting in the formation of dense nearly spherical primary particles. Finally such primary particles hit each other and undergo surface growth forming larger structures.

The derivation of models accounting all this mechanisms is required to describe the aerosol dynamic. The aim is to predict the particles distributions in dependence of the main variables influencing their properties. Thus at least the particle volume (ν) or the equivalent spherical diameter (ED= $(6\nu/\pi)^{1/3}$) have to be considered. More detailed approaches, able to describe the particles fractal structure, require accounting also for the particles surface as a minimum (Friedlander, 1977).

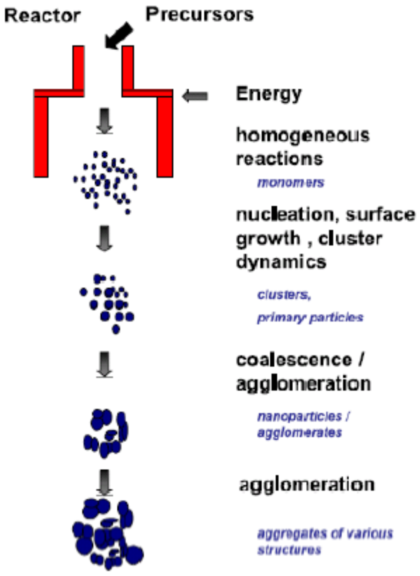

Figure 7 – Scheme of process involved in particles formation (Roth, 2007).

The equations of aerosol dynamic consist of simple population balance on the particles number concentration distribution ($N(\nu,x,t)$). A convective diffusion equation can be obtained by the total particles volume (mass) conservation accounting for the particles velocity (c) and diffusivity (D).

$$\frac{\partial N(v,x,t)}{\partial t} + \nabla \cdot \left[N(v,x,t)\cdot c\right] - \nabla \cdot \left[D \cdot \nabla N(v,x,t)\right] = ADT \qquad (2.1)$$

Many of the aerosol dynamic terms (ADT) on the RHS of equation 2.1 will be described in the following paragraphs. They are that of major interest for the studied topic but other processes, such as fragmentation, thermophoresis, electrophoresis and particles losses for settling, diffusion, inertial impaction, rainout and washout, could be accounted.

2.2 Homogeneous nucleation

The homogeneous nucleation theory deals with the phase transitions occurring in a supersaturated gas or liquid without involving an existing physical surface. It is also known as homogeneous condensation. Homomolecular and heteromolecular nucleation can be distinguished in the formation of a particle with ν volume. The first involves single specie while the latter regards more species simultaneously. The nucleation occurrence involves both the particles number concentration and volume fraction increase and it appears in the population balance equation of a homogeneous aerosol as a source term (Seinfeild and Pandis, 1998).

$$\frac{\partial N(v,t)}{\partial t} = \left(\frac{\partial N(v,t)}{\partial t} \right)_{nucl} \tag{2.2}$$

The nucleation step involves the transformation of a vapor or liquid to stable molecular clusters by a series of reversible steps. Indeed, the attractive forces between molecules involve molecular cluster formation also in unsaturated condition. Such clusters can quickly decompose because of molecules evaporation or be stable and further grow generating nuclei particles, the latter eventuality occurring when the free energy change accompanying the phase transformation is negative. The decisive parameter in determining clusters persistence is the supersaturation ratio (S), defined to be the ratio between the bulk concentration of a species, far from physical surfaces, and the same species concentration on a flat surface at equilibrium between two physical phases. In the case of a condensing gaseous species, it is simply the species bulk partial pressure (P) to its saturation vapor pressure ($P_{0,sat}$) ratio. It is strongly influenced by the temperature (Linak and Wendt, 1993).

$$S = \frac{P}{P_{0,sat}} \tag{2.3}$$

The classical thermodynamic nucleation theory main approximation is the assumption that the clusters temperature and the surrounding medium temperature (*T*) are the same. This is not exactly true because of the latent condensation heat release during cluster formation. The other main approximation is the hypothesis that clusters have spherical shape and the same physical properties of bulk matter. Particularly the *capillary approximation* assumes that the cluster interface free energy is the product of bulk particles surface tension (σ) with the cluster surface area. Furthermore clusters are assumed to interact only with molecules and not each with another.

The nucleation theory is based on a set of equations describing the cluster concentration and accounting for the molecule addition and removal on clusters. The equilibrium is reached at the steady state balance between the rate of molecules addition on clusters and their removal rate. Such balance is reached on clusters with a *critical equivalent diameter* (ED^*), being the diameter of a sphere having the cluster volume. The clusters smaller than critical ED disappear because of the molecules removal faster than their addition. On the contrary the larger clusters continue to grow via molecules addition (condensation).

$$ED^* = \frac{4 \cdot \sigma \cdot \nu_{mol}}{RT \cdot \ln(S)} \tag{2.4}$$

R and ν_{mol} are the universal gas constant and the cluster molar volume, respectively. The equation 2.4 can be rearranged to express the actual saturation vapor pressure (P_{sat}) on a surface with curvature radius $CR=ED^*/2$, in term of that on a flat surface ($P_{0,sat}$). This dependence is known as *Kelvin effect* and it involve the increase of the equilibrium vapor pressure over curved compared to flat surfaces. This effect also occurs inside the capillaries (Friedlander, 1977).

$$\ln\left(\frac{P_{sat}}{P_{0,sat}}\right)=\frac{2\cdot\sigma\cdot\nu_{mol}}{RT\cdot CR} \tag{2.5}$$

The clusters population balance allows also expressing the particles nucleation rate. It is described by a Dirac distribution (δ) centered at the cluster critical volume (ν^*) because only such kind of cluster represent incipient particles (Oxtoby, 1992).

$$\left(\frac{\partial N(v,t)}{\partial t}\right)_{nucl}=A\cdot n^2\cdot\exp\left[\frac{-B}{T^3\cdot(\ln S)^2}\right]\cdot\frac{\exp\left(C\cdot T^{-1}\right)}{S}\cdot\delta\left(\nu-\nu^*\right) \tag{2.6}$$

A, B and *C* are constant depending on the nucleating particles physical properties, such as surface tension, molar volume and density, and *n* is the numerical concentration of the condensing molecules.

The main merit of the thermodynamic homogeneous nucleation theory is to capture the phase transition condition. Particularly it satisfactory describes the nucleation rate dependence on the supersaturation and the second order kinetic respect to condensing vapor concentration.

The main problems related to the use of the classical nucleation theory is that it greatly underpredict the clusters critical size, often conducting to calculate value lower than the molecular size, and it overpredict the nucleation rate. The first problems could be related to the assumption of particles bulk physical properties for the molecular clusters. Some of such properties, such as surface tension, could be devoid of meaning on this length scale involving erroneous results. The classical theory is of value in showing the tendency to nucleate, but not in providing the size of the nuclei. More rigorous approaches are available, such as using density function theory to calculate the free energy of clusters (Oxtoby, 1992). The experimental approach in determining such critical size can be followed too.

The second problem of the thermodynamics approach is that it completely fails in predicting both the nucleation rate absolute value and its temperature dependence. The nucleation rate overprediction is also influenced by the bulk properties assumption and can be corrected substituting the constant *A, B* and *C* with opportunely tuned parameter. The not correct prediction on the temperature effect is probably due to the strong assumption of thermal equilibrium between the clusters and the surrounding medium. As mentioned above, this assumption is not valid because of the latent condensation heat release during the cluster formation.

Some attempts to account not isothermality were performed but a definitive theory is not yet available. Generally the temperature correction account for a cluster temperature slightly higher respect to the surrounding medium. The effect is to enhance molecules evaporation from clusters resulting in a higher critical diameter and a lower nucleation rate (Seinfield and Pandis, 1998).

2.3 Coagulation

The coagulation is the process in which particles, subject to a relative motion, collide with each other and form larger structures. It involves a gradual reduction of the particles number. Three coagulation modalities can be distinguished and they are coalescence, sintering and agglomeration, respectively. The coalescence occurs when the particles melt together forming a larger particle in which they are not more identifiable while particles undergo agglomeration when they stick together preserving their identity. The sintering process is an intermediate one in which the particles merge together only partially. The coagulation is responsible for the final particles physical structure. The coalescence promotes the formation of dense spherical particles while the agglomeration is responsible for the large fractal structure observed for combustion generate particles. The prevailing of one mechanism on another is strongly influenced by some particles and environmental physical properties, mainly temperature and viscosity, and by particles size (Helble and Sarofim, 1989; Helble, 1998). Agglomeration usually prevails for larger particles while the term coagulation is generically used for particles smaller than 10nm always coalescing.

Thermal and kinematic coagulation can also be distinguished depending on the particles collision modality. The thermal coagulation is the result of the Brownian collisions involved by particles thermal motion. The kinematic coagulation occurs if the particles motion is driven by external forces, such as gravity or electrical forces, or medium stretching.

The coagulation equation is a simple population balance describing the temporal evolution of a polydisperse aerosol size distribution (*N(ν,t)*). It is composed of a source and a sink term. Indeed particles having a certain volume (ν) can be generated because of smaller particles coagulation or disappear because they coagulate with a particle of volume (*q*). This simple balance, not accounting for condensation, is described by the Smoluchosky equation in the case of a homogeneous not nucleating aerosol (Hinds, 1999).

$$\frac{\partial N(v,t)}{\partial t} = \frac{1}{2}\int_0^{v} K \cdot N(v-q,t) \cdot N(q,t) \cdot dq - N(v,t) \cdot \int_0^{\infty} K \cdot N(q,t) \cdot dq \qquad (2.7)$$

The coagulation kernel (*K*) represents the coagulation frequency of two particles with unitary numerical concentration. It account for inter particles interactions and strongly depends on particles size and on the coagulation modality. The coagulation kernel can differ from the collision kernel (K_{coll}), representing the collision frequency per unitary concentration, because of not unitary coagulation efficiency (γ_{coag}) depending on particles sizes.

$$K(\upsilon,q) = \gamma_{coag}(\upsilon,q) \cdot K_{coll}(\upsilon,q) = \gamma_{coag}(\upsilon,q) \cdot \left[K_{kin}(\upsilon,q) + K_{th}(\upsilon,q)\right] \qquad (2.8)$$

The coagulation efficiency is commonly assumed to be unitary for particles larger than 10nm, thus the problem is to specify the collision kernel. The latter is usually given by two contributions. The kinematic collision kernel (K_{kin}) is strongly influenced by the flow characteristics but it could be neglected for ultrafine particles. A rigorous derivation of the thermal collision kernel (K_{th}) requires the proper solution of the Boltzmann equations. A simplified approach may be followed assuming spherical particles and accounting for the Knudsen number (*Kn*). It represents the molecular mean free path (λ) to particles equivalent diameter ratio, the latter representing the diameter of a sphere having the same volume of the particles.

$$
\begin{aligned}
ED &= \left(\frac{6 \cdot \nu}{\pi}\right)^{1/3} \\
Kn &= \frac{2 \cdot \lambda}{ED}
\end{aligned}
\tag{2.9}
$$

Three different regimes of interaction between the particle and the fluid can be distinguished depending on Kn value:

- ✓ Kn → 0, continuous regime: the gas behaves as a continuum medium respect to particles (Epstein, 1929). Particles macroscopically diffuse into the medium with a proper diffusivity (*D*) resulting from their thermal collision.

$$K_{th}(ED_i, ED_j) = 2\pi \cdot (ED_i + ED_j) \cdot (D_i + D_j) \tag{2.10}$$

- ✓ Kn ~ 1 transition or Knudsen regime: approximate Boltzmann equation solutions, such as the Fuchs and Sutugin solution, are required. The thermal collision kernel are usually expressed with interpolative formulas (Seinfeld and Pandis, 1998);
- ✓ Kn >> 1 molecular regime: each molecule interacts independently with the particles not disturbing the velocity distribution field. In this regime the particle behave like a molecule itself. They move with a square mean root velocity (*c*) depending on its mass (*m*) and temperature (*T*) as described by the Boltzmann (K_B) gas kinetic theory.

$$
\begin{aligned}
c_i^2 &= \frac{3 \cdot K_B \cdot T}{m_i} \\
K_{th}(ED_i, ED_j) &= \frac{\pi}{4} \cdot (ED_i + ED_j)^2 \cdot (c_i^2 + c_j^2)^{1/2}
\end{aligned}
\tag{2.11}
$$

The Smoluchosky equation solution remains a challenging problem also in the simplifying assumption of unitary coagulation efficiency and pure thermal coagulation. Analytical results can be obtained in the further hypothesis of initial lognormal distribution (Park, 1999). A self preserving size distribution solution, moving towards larger diameters and reached at the steady state, can be obtained by a similar transformation (Friedlander and Wang, 1966). Real problems solutions require a numerical approach and many types of software were developed to this purpose (Gerbard and Seinfeld, 1980).

A lot of preliminary information can be obtained in the hypothesis of initial monodisperse particles with number concentration N_0. Indeed the Smoluchosky equation greatly simplifies in this case and it describes the monodisperse particles number concentration evolution.

$$\frac{dN(t)}{dt} = -K \cdot [N(t)]^2 \tag{2.12}$$

The coagulation kernel is constant because only particles with a defined size are considered, thus the analytical solution is quickly obtained.

$$N(t) = \frac{1}{1 + K \cdot N_0 \cdot t} \tag{2.13}$$

The characteristic decay time of the decreasing number concentration is that required to half the initial value and it is labeled particles half-life (t_{half}).

$$t_{half} = \frac{1}{K \cdot N_0} \tag{2.14}$$

The comparison of the experimentally observed half-life with the gas kinetic ones, obtained using the collision despite the coagulation kernel in the 2.14, is a powerful tool to obtain preliminary information about the coagulation efficiency especially for particles smaller than 10nm.

The coagulation efficiency represents the fraction of collisions followed by coagulation. The eventuality that two particles could stick or not after undergoing a collision is a rather controversial issue. The coagulation efficiency is usually regarded as an empirical parameter usually assigned as unitary assuming that nanoparticles behave similar to larger submicron particles. Indeed such larger particles have a higher possibility to transfer the impact kinetic energy to their internal freedom degrees stabilizing the generated complex (Gay and Berne, 1986). Some approaches account for Van der Walls interactions simply considering an increase in the collision frequency independently of how many collisions result in coagulation (Harris and Kennedy, 1988).

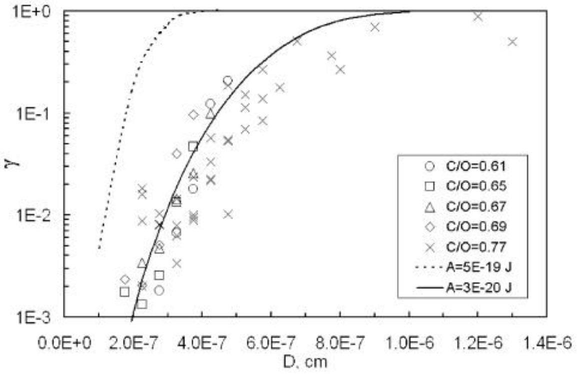

Figure 8 – Adhesion efficiency on substrates of flame generated carbonaceous nanoparticles (D’Alessio et al., 2005).

D’Alessio et al. (2005) experimentally showed that the coagulation efficiency of flame generated carbonaceous particles suddenly decreases for size smaller than 5nm. They also explained such decrease by comparing the particles mean kinetic energy, calculated with gas kinetic theory, with the potential energy of the Van der Walls pair particles interaction (Hamacker, 1937). A collision involves a coagulation event only when such potential energy is higher than particles kinetic energy. D’Alessio et al. (2005) also explained the experimentally observed similar sudden decrease of particles adhesion efficiency on substrates, showed in Figure 8, with the same approach. Such low coagulation and adhesion efficiencies imply that nanoparticles smaller than 5 nm may be easily dispersed into the atmosphere because they have a much longer life-time than generally assumed and may easily bounce on surfaces or filters.

2.4 Surface growth

The compounds in vapor phase may distribute on surface of particles involving their growth because of both chemical reaction and condensation, the latter also known as heterogeneous nucleation. This mechanism is more active for smallest particles because of the specific surface increase with decreasing size. Anyway some results seems to show surface growth infectiveness for size smaller than 10nm implying a longer lifetime of such particles class (Altman et al., 2004).

Surface growth involves the particles volume fraction increase without affecting their number concentration and it is described, in a homogeneous aerosol, by a simple particles number concentration balance equation (Friedlander, 1977).

$$\begin{aligned}\frac{\partial N(v,t)}{\partial t} &= -\frac{\partial}{\partial \text{v}}\left[N(v,t)\cdot\left(\frac{\partial \text{v}}{\partial t}\right)_{surf}\right] \\ \left(\frac{\partial \text{v}}{\partial t}\right)_{surf} &= \frac{1}{\rho}\cdot\left(\frac{\partial m}{\partial t}\right)_{surf}\end{aligned} \tag{2.15}$$

The surface mass source on particles can account also for a negative contribution due to mass loss because of evaporation or surface consumption reactions, such as oxidation. The approach in describing these mechanisms is quite similar to that shown for surface growth.

The surface growth takes place by steps. The first step involves gaseous molecules diffusion toward particle surface. Subsequently the gaseous molecule could diffuse inside the particles itself to reach a reactive site. This is the case only for porous particles. Finally the molecule is captured reacting or condensing on the surface. Each of these processes could represent a limiting step.

The rate of mass addition on the ρ density particle surface, in the case of mass transfer limited process, is equal to the diffusive flux that can be calculated by solving the Boltzmann equations. The diffusive flux of a MW molecular weight vapor with c_∞ bulk concentration and c_{sat} saturation concentration, accounting the Kelvin effect, is well described by the Fuchs-Sutugin interpolation solution for a spherical particle giving good results in the entire size range of combustion generated particles (Fuchs and Sutugin, 1971).

$$\rho \cdot \left(\frac{d\upsilon}{dt} \right)_{surf} = \left(\frac{dm}{dt} \right)_{surf} = 2\pi \cdot \left(c_{\infty} - c_{sat} \right) \cdot D \cdot ED \cdot \frac{1 + Kn}{1 + 1.71Kn + 1.33Kn^2} \cdot MW \quad (2.16)$$

This simple approach is able to capture the first order kinetic in the condensing species concentration differing respect to the second order of nucleation. The competition between homogeneous and heterogeneous nucleation is an issue whenever combustion products with condensable vapors are cooled in the presence of other aerosols. In any case, the prevailing of one mechanism on another is strongly influenced by the vapor cooling rate. Nucleation generally prevails at higher cooling rate thus involving the generation of smaller particles respect to lower value favoring the surface condensation (Linak and Wendt, 1993).

The diffusive flux does not influence the mass addition when the surface reaction rate (k_s) controls the process.

$$\rho \cdot \left(\frac{d\upsilon}{dt} \right)_{surf} = \left(\frac{dm}{dt} \right)_{surf} = \pi \cdot ED^2 \cdot c_{\infty} \cdot MW \cdot k_S \quad (2.17)$$

The expression of surface reaction rate greatly depends on the specific case and it usually involves quite complex chemistry description. Bockhorn et al. (2008) recently edited a book on carbonaceous particles chemistry while Linak and Wendt (1993) reviewed the metal fate in combustors. The literature also covers the cases of combined mass transfer and surface kinetics and the additional complication of pore diffusion in porous surfaces (Seames and Wendt, 2000).

The mass concentration of specie in a particle can be easily calculated by integrating the deposition rate along the particle trajectory dividing this integral to the total mass of the particle.

$$MassConc(ED) = \frac{\int_0^t \frac{dm}{dt} dt}{\frac{\pi}{6} ED^3 \cdot \rho} \qquad (2.18)$$

This relation is not quite useful in predicting particles surface enrichment in real combustor because the trajectory is commonly unknown but it represent a powerful tool to interpret experimental results understanding the limiting step for surface deposition of the species of interest. Indeed substituting the equation 2.16 or 2.17 into the 2.18 the mass concentration results to depend on an ED power function and specifically it is proportional to ED^{-n}, with the concentration increasing as the particle size decreases. The smaller particles are more enriched in volatile matter as qualitatively affirmed before. The value of the exponent obtained from experimental results can be compared with that predicted considering the surface growth limiting mechanism and reported in Table 3. One case concerns the porous particles with the reactions kinetics as limiting step. For this case, the amount of reaction is proportional to volume, and the reacting species concentration is independent of particle size.

Table 3 – **Exponent in size-dependent mass concentration of surface deposited species (Lighy et al., 2000).**

Controlling mechanism	Size range	Concentration $\propto (1/ED^n)$ Exponent n
External Mass Transfer	Ultrafine (Kn >> 1)	1
External Mass Transfer	Supermicron (Kn << 1)	2
External Surface Kinetics	All Sizes	1
Internal Surface Kinetics (porous particles)	All Sizes	0

Chapter 3

Thesis objective and methodologies

3.1 Motivation and objective

The atmospheric aerosols, among other pollutants, are object of a strong research activity because of their influence on climate change (Jacobson, 2001) and their adverse human health effects (Oberdorster et al., 2002; Kennedy, 2007). Combustion systems are the main sources of particulate matter in urban areas released into the atmosphere in a wide size range (Lighty et al., 2000). Recent studies are focused on the ultrafine aerosols because of their differences compared to bulk material. Particularly, combustion generated nanoparticles, shows unique properties with respect to bigger ones (Pratsinis, 1998) and they require to be further investigated. They are more difficult to control or capture because the efficiency of the filtering devices decreases with particles size (Zhuang et al., 2000). Moreover recent toxicological results have shown that particles toxicity depends on their numerical more than mass concentration and increases with decreasing size (Oberdorster et al., 2005; Brown et al. 2001).

Up to recent times the emission of particles with size below 5nm was not taken in consideration because of two reasons. Firstly the commercial diagnostics were able to detect only particles larger than 5nm. On the other hand it was assumed that such small particles meet and coagulate at gas kinetic rate so that their lifetime was negligible small (Hinds, 1999). Recent advances in diagnostics, either with Differential Mobility Analysis (DMA) or with Atomic Force Microscopy (AFM), have extended the field of measurability for nanoparticles in flame down to 1nm (D’Alessio et. al., 2005; Sgro et al., 2007). On these bases it was realized that coagulation rate of carbonaceous nanoparticles at high temperature, as well their adhesion rate, drops dramatically orders of magnitude as their size decreases below 5nm. Consequently those, commonly hidden, nanoparticles may escape from combustors and bounce on filters surviving in the atmosphere in a not negligible amount involving a severe pollution problem.

Carbonaceous particles, produced in fuel rich conditions, have been widely studied in the entire size range they are released (Bockhorn, 1994; Bockhorn, 2008) but few efforts have been spent to investigate inorganic particles with size below 10nm. While coarse and fine fractions of combustion generated inorganic particles are supposed to be formed by fragmentation of coarser material, the ultrafine fraction is mainly generated by metal compounds vaporization and successive condensation (Sarofim et al., 1997; Linak and Wendt, 1993). Metals, always contained into wastes, crude oils, coals and biomass or used as fuel additives, can be introduced into combustion chamber in many physical and chemical forms but, after some transformation at high temperature, they are released as particles substantially in the same amount (Linak and Wendt, 1993).

As described in the previous chapters, the addition of trace amount of metals in a flame causes the formation of nanosized particles, usually composed of their non volatile oxides (Kelly and Padley, 1967). This is an interesting feature when the aim is to produce powders with specific physical and chemical characteristics (Roth, 2007). Unfortunately this probably takes place also burning ashes containing fuels. The classical thermodynamic homogeneous and heterogeneous nucleation theories are able to predict the conditions of phase transition but cannot explain the reason of the incipient particles nanometric sizes. Also mechanisms of coagulation, coalescence and surface reactions involved in nanoparticles growth are not clear and require more investigation in order to develop better control technologies (D'Alessio et al., 2005; Altman et al., 2004).

The main objective of this thesis is to experimentally discover if metal nanoparticles coagulation and adhesion efficiency, at high temperature, follow the same trend of carbonaceous nanoparticles, quickly decreasing for size below 5nm.

Subsequently we will try to proof that the production of such extremely small inorganic nanoparticles could take place burning ash containing fuels and, particularly, our first attempts will be addressed to coal combustion.

Incidentally, we designed flame reactors to produce such small particles that could be a starting point for material science research activity. Indeed primary particles of flame synthesized nanopowder and nanocatalyst commonly have quite larger size than 5nm.

3.2 Methodologies

Many researchers have investigated toxic metal aerosols stack emissions and their formation in post combustion condition (Linak et al., 2007) but only a few researchers have focused their attention on toxic metal aerosol nucleation in a high temperature environment such as a flame. Particularly Buckley et al. (2002), Yu et al. (1998) and Ehrman and Friedlander (1999) focused on lead, chromium and Zn-Cu-Mg mixtures, respectively. Mulholland et al. (1991), D'Anna et al. (1998), Merola et al. (1998) and Kurtz et al. (1999a; 1999b) studied the fate of toxic metals in combustion-like environments heating-up droplets of metal nitrate aqueous solutions into drop-tube furnaces. Probably, nanoparticles have not been detected because they were hidden by larger particles and below the used diagnostic sensitivity. Recently Fennell et al. (2007a; 2007b) have shown the formation of particles smaller than 10nm by feeding metal chloride water solution aerosols into a flame.

On this basis we decided to develop a simple laboratory experiment. It consists in injecting metal salts aqueous solution droplets in hydrocarbons flat laminar premixed flame in lean or stoichiomentric condition to avoid carbonaceous particle formation. The flames provides the droplets fast heating and transformation to particles and it simulates combustion environments, particularly that of waste incineration (Mulholland and Sarofim, 1991). Moreover this experimental configuration allows investigating nanoparticles formation from real fuel combustion. This may be accomplished substituting the aqueous solution with liquid fuels or pulverized solid fuels dispersions/suspensions. The latter eventuality was realized using pulverized coals and preliminary analysis were performed.

The main advantage of using such doped laminar premixed flames is that they allow following the aerosol temporal dynamic by simply performing measurements at several heights above the burner. Indeed, known the flame temperature profile, they univocally correspond to particles residence time in flame. Moreover the laminar flux prevent complex and hard to account turbulent mixing effects occurring in other experimental configuration or in real combustors. In this way we are able to quickly obtain information on nanoparticles grow rate and thus on coagulation efficiency. The experiment also allows studying the influence on nanoparticles behavior of some physical parameter like the temperature simply changing the hydrocarbon flame condition such as stoichiometry and dilution.

The other major advantage of this experimental configuration is that it permit, fixed the amount of fed metal, to evaluate in advance the total mass of produced particles by a simple material balance. This allows obtaining preliminary information on particles adhesion efficiency by comparing the total volume of thermophoretically collected particles with that of particles impinging on the substrate because of thermophoretic force. The use of two diagnostic, one performing particles sizing in flame and the other on collected ones, is obviously required to have more detailed information.

The choice of used diagnostics is a crucial point of this research activity because it is focalized on particles as small as 1nm. The Atomic Force Microscopy (AFM) was preferred to other microscopy technique to perform collected particles dimensional analysis because, producing three-dimensional images, it allow to directly measure their volume (Barone et al., 2003). This feature is suitable to estimate the adhesion efficiency and it also prevents size evaluation errors caused by bi-dimensional imaging of not spherical shaped particles. On the contrary it allows obtaining information on particles morphology. Unfortunately all AFM results regard collected particles and they are influenced by adhesion efficiency.

Optical diagnostics, particularly Laser Light Scattering (LLS), were also used to perform particle sizing. Their main advantage is to be in situ technique but they allow to directly measure, at least in our case of very small particles, only mean value of nanoparticles sizes requiring the knowledge of their optical properties that could be quite different to that of bulk material.

On-line size distributions measurements by high resolution Differential Mobility Analyzer (DMA) were also performed to overcome this limitation. This technique does not require the preventive knowledge of any particle physical property but oblige to use some sampling probe that could heavily perturb the studied reactor and influence the results.

Scanning Electron Microscopy (SEM) imaging together with Energy Dispersive X-Ray Spectroscopy (EDXS) of sampled particle is also employed to obtain information on particles in a larger dimensional range and on their elemental chemical composition.

Chapter 4

Experimental configurations and Diagnostics

4.1 Doped flame reactors

To realize the doped premixed flat flame we used two different burners and a droplets generator. The latter was chosen to be a Berglund Liu type (Berglund and Liu, 1973) because of two reasons. The first and main reason is that it allows to directly controlling the droplets flow rate not requiring a laborious calibration. The other reason is that it generates droplets of equal sizes allowing to investigate the droplets size influence on the results.

4.1.1 Vibrating Orifice Droplet Generator

The Berglund Liu type Vibrating Orifice Aerosol Generator (VOAG) produces monodisperse liquid droplets by a wide range of solutions or dispersion by exploiting the instability of a cylindrical liquid jet induced by a mechanical vibration. The generator used in this research activity is a VOAG Model 3450 manufactured by TSI.

The phenomenon that leads to the rupture of a uniform liquid jet due to a mechanical vibration, schematically shown in Figure 9, was studied for the first time experimentally by Savart and theoretically by Plateau and Rayleigh (Rayleigh, 1874).

Plateau derived, considering the liquid surface tension (σ), the relation between the jet diameter (D_j) and the minimum wavelength (λ_{min}), representing the jet speed (V_j) to vibration frequency (f) ratio, to obtain such jet instability, while Rayleigh calculated its optimal value (λ_{opt}) in the vacuum.

$$\begin{aligned}\lambda_{\min} &= \pi \cdot D_j \\ \lambda_{opt} &= 4.508 \cdot D_j\end{aligned} \tag{4.1}$$

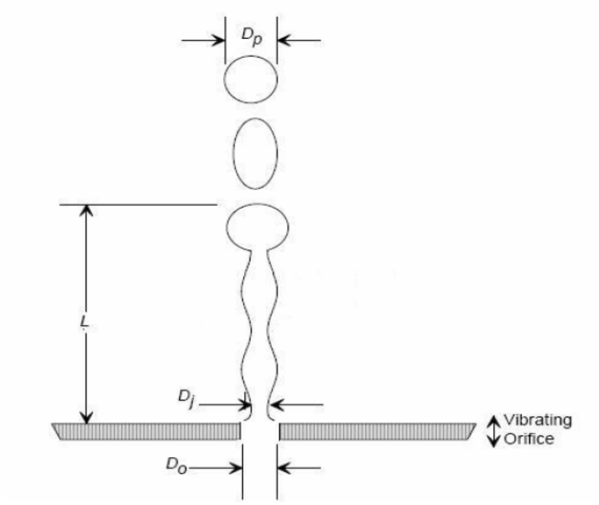

Figure 9 – Scheme of jet break up and droplets formation induced by a mechanical vibration (TSI, 2002).

Lindbland and Schneider calculated the minimum speed ($V_{j,min}$) necessary for the formation of a capillary jet by energy conservation relations considering the liquid surface tension and density (ρ).

$$V_j \geq V_{j,\min} = \left(\frac{8 \cdot \sigma}{\rho \cdot D_j} \right)^{\frac{1}{2}} \tag{4.2}$$

Schneider and Hendricks determined experimentally the possibility to obtain uniform droplets by varying the range of wavelength in the interval.

$$3.5 \cdot D_j \leq \lambda_j = \frac{V_j}{f} \leq 7 \cdot D_j \tag{4.3}$$

A single droplet is produced, in this condition, during each oscillation cycle and its diameter (D_d) is simply obtained by the total jet flow rate (Q).

$$D_d = \left(\frac{6 \cdot Q}{\pi \cdot f} \right)^{1/3} \tag{4.4}$$

Monodisperse particles of diameter D_p are generated from such droplets when the solvent of the solution, containing not volatile solute in a given volume concentration (C), evaporates.

$$D_p = D_d \cdot C^{1/3} \tag{4.5}$$

A scheme of the used VOAG (Model 3450, TSI) is showed in Figure 10 and it consists of two basic systems: a droplets generator of and a flow system.

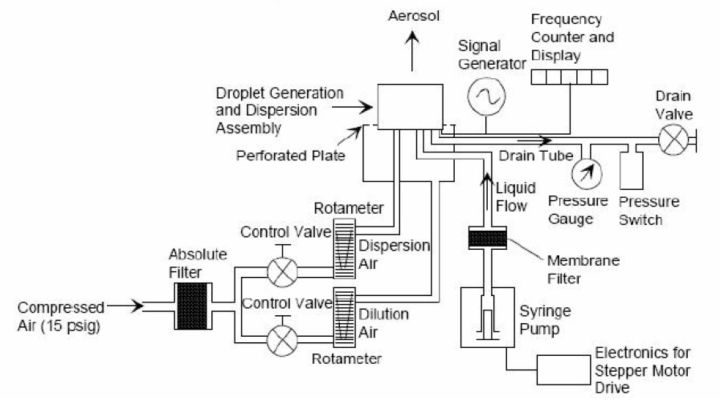

Figure 10 – Components scheme of the used VOAG (TSI, 2002).

The droplets generator consists of a syringe pump, an orifice and a signal generator. An electric stepper motor pushes, at constant velocity, the syringe plunger to inject the solution. The syringe can be equipped with a membrane filter to prevent orifice clogging by impurities. The solution is sent to the droplets generator assembly from which it can be drained opening a valve. Instead, closing the valve, the solution is forced to escape from a calibrated orifice producing a jet. The orifice is mounted on a piezoelectric crystal that can be put in oscillation applying the voltage wave produced by the signal generator. The induced jet instability produces, in right conditions, a monodisperse droplets flow.

The droplets diameter can be adjusted by varying the orifice oscillation frequency and the solution flow rate. The latter is determined, set the syringe internal diameter, by controlling the syringe plunger speed (0.1*10^{-4}cm/s to 9.9-10^{3}cm/s). The square voltage wave produced by the signal generator can be also adjusted both in frequency (1KHz to 1 MHz) and in amplitude (0V to 12V). In this way, monodisperse droplets with diameter between 20μm and 250 μm can be generated using orifices of different sizes (from 10μm to 100μm).

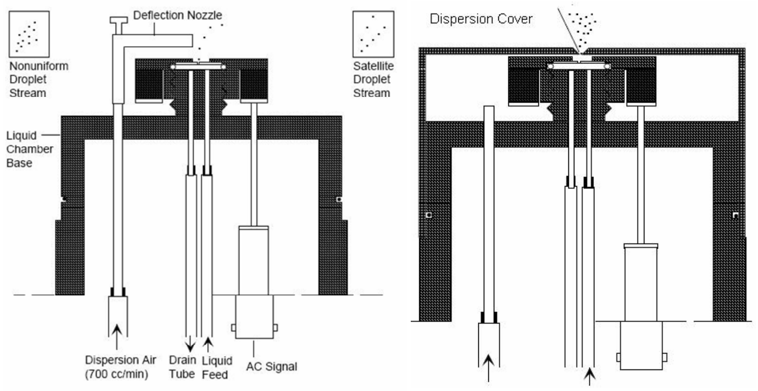

Figure 11 – Right side: deflection test; Left side: droplets dispersion (TSI, 2002).

The flow system is used both to verify the droplets size uniformity and to disperse droplets into a gas stream preventing their coalescence. An air flow of 700cm^3/min deflecting the jet is used to check the droplets monodispersion. The droplets have uniform size if the deflected jet is compact while the presence of two or more deflected streams indicates droplets polydispersion. Figure 11 shows images of the deflection test and the possible circumstances. The droplets monodispersion is obtained properly regulating the vibration frequency and amplitude.

However, the main use of the dispersion flow is to prevent the droplets coalescence. The droplets dispersion in the gaseous flux is obtained using a drilled cap covering the droplet generator assembly. The droplets through the hole carried by the dispersion flux that open the jet and separate the droplets, as shown in Figure 11. The dispersion flux can be adjusted, using a rotameter, between 200cm^3/min and 2500cm^3/min. Generally the optimal value to prevent coalescence is around 1500cm^3/min.

4.1.2 Burners

We used two burners to stabilize the laminar premixed flat flames in which inject the monodisperse droplets.

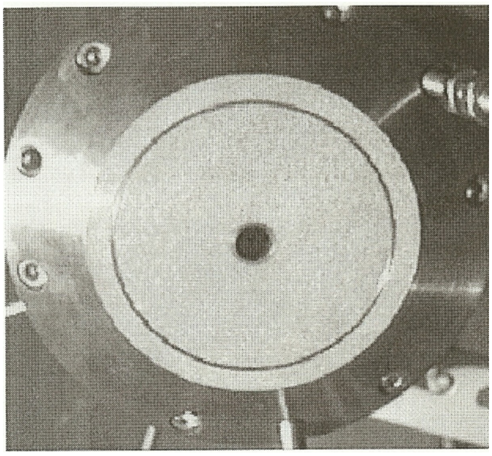

Figure 12 – A picture of modified McKenna Burner.

The first is a bronze porous plug McKenna burner and is shown in Figure 12. The porous plug is 60mm in diameter and it can be cooled by forced water circulation allowing to stabilize flames with several velocities and equivalence ratios. The burner is also equipped with a porous annulus allowing feed a gaseous sheath flow isolating the flame from the environment. The burner was properly modified to feed the droplets. Indeed the porous plug was drilled to insert a cylindrical stainless steel tube coaxially to the burner. The tube, 100mm long and 7.5mm of internal diameter, allows feed the aerosol in the center of the flat flame. The fed aerosol is quickly heated by diffusively mixing with surrounding premixed flame hot exhaust gasses. This burner does not allow realizing a perfect plug flow reactor.

A burner capable both to stabilize the flame and to allow the homogeneous adduction of droplets or particles was properly designed. This burner, quite similar to that used by Arabi-Katbi et al. (2002), realizes a plug flow that is a key feature to simplify both diagnostic selection and the results interpretation.

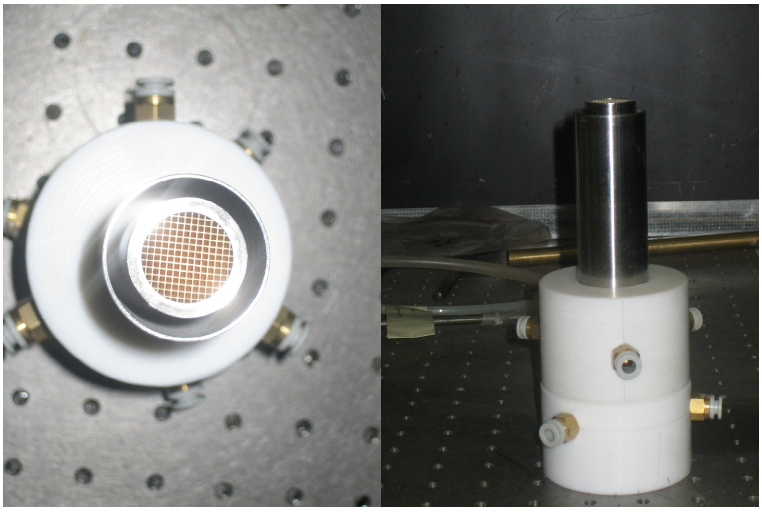

Figure 13 – Images of the designed honeycomb burner.

The burner, shown in Figure 13, consists of two concentric stainless steel tubes. The inner tube has an internal diameter of 18 mm. A 40mm long mullite zirconia honeycomb (400 cpsi, CTI s.a.) both stabilizes the flame and allow the aerosol to flow. The outer tube provides an outside ring (24mm ID and 32mm) used to flow an inert gas whose function is to isolate the flame from the outside environment.

4.2 Atomic Force Microscopy analysis

The Atomic Force Microscopy AFM technique, designed by Binning, Qatar and Gerber in 1986, has recently proved very effective in the study of submicron particles, particularly to atmospheric aerosols (Friedbacher and Grassbauer, 1995 and Köllensperger et al., 1997).

The AFM has many advantages respect to other microscopy techniques:

- ✓ easy operating conditions: the AFM can also operate in ambient condition;
- ✓ three-dimensional topological imaging;
- ✓ quite high resolution imaging, up to the Angstrom;
- ✓ applicability to non-conductive samples;
- ✓ fast imaging procedure.

The AFM operating principle is based on the interaction between a nanometric probe and the sample surface. The probe is not conductive and it is generally made with materials having very high elastic modulus. The probe carries out a scan on the surface to be analyzed, interacting with the sample by attractive or repulsive forces. The sample can be moved with nanometric accuracy by a piezoelectric actuator. The probe tip is placed on a cantilever oscillating close to resonance frequency. The atomic interactions between the tip and sample surface change the cantilever free oscillation frequency. The distance is assured to be constant during the surface scan by a feedback system moving the sample to maintain constant the cantilever free oscillation frequency.

The used AFM microscope is the Nanoscope IIIa ™ Digital Instruments, showed in Figure 14 together with its operating scheme. This instrument can be run in two different operational modes, *contact-mode* and a *tapping-mode*.

The better known *contact-mode* technique consists of scansions performed with the tip directly touching the surface to be analyzed. It assures atomic resolution in ultra high vacuum condition but it is also quite sensitive to ambient humidity because of capillary forces. It is widely used in all cases in which the observed surfaces are resistant to micromechanical solicitations because of quite high interaction force between the tip and the sample (10nN down to few μN).

The *tapping-mode* technique consists of the probe in oscillation close to the sample surface, permitting the tip to touch the surface just slightly. The major advantage of running in *tapping-mode* is that the strong tip sample interactions are avoided. The contact force is reduced to less than 100pN, which allows observation of samples that are not strongly bonded to the substrate surface. Therefore, accidental removal or shifting of the sample on the substrate surface is prevented. It is also worth mentioning that in *tapping-mode* the *phase shift detection* feature allows investigations of the viscoelastic properties of the samples (Ramirez- Aguilar et al., 1999). It consists of measuring the phase shift between the input signal that governs the oscillation and the deflection/oscillation output signal of the cantilever. Both topographic and phase signals can be acquired simultaneously because the feedback acts independently from the modulation.

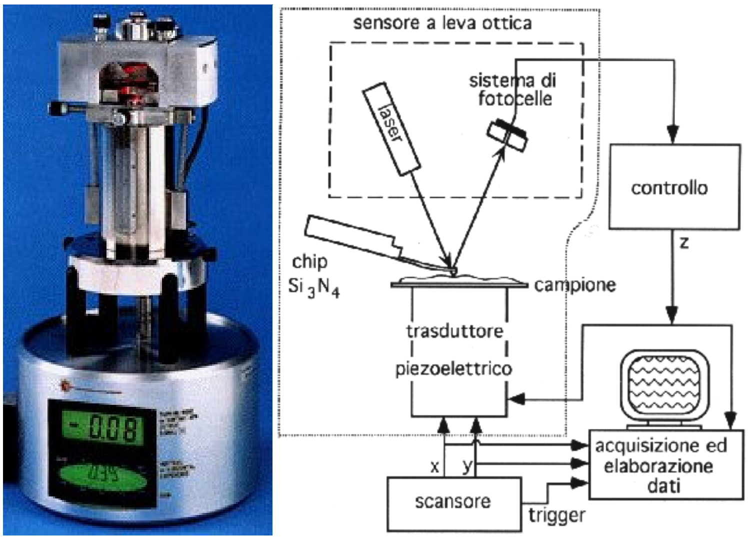

Figure 14 – Nanoscope IIIa ™ (Digital Instruments) AFM and its operating scheme.

The *tapping-mode* technique was preferred in this work because of its many attractive features and because it has been successfully used to analyze flame generated carbonaceous nanoparticles (Barone et al., 2003). Using this mode it is possible to obtain three dimensional images of the collected material, with a resolution of about 1-2 nm along x/y axes and below 0.1nm, in low noise condition, along z axis.

Particles are collected on substrates for the subsequent AFM analysis. The ideal collecting substrate has the following features:

- ✓ Very low roughness (less than 0.2 nm), to distinguish very small structures from the background noise;
- ✓ Elevated mechanical and chemical resistance to high temperatures;

- ✓ The possibility to obtain extremely clean surfaces (cleavable surfaces are preferred).

Mica muscovite disks, with its very good cleavage, were reported to give good results in analyzing thermophoretically collected flame generated carbonaceous particles (Barone et al., 2003). Thus this kind of substrate is used in this study.

Silicon probes (Nanoprobe® Super Sharp Silicon) with apical curvature radius smaller than 4 nm and a sidewall angle of about 20°, were used to minimize the probe-sample convolution effects, schematically illustrated in Figure 15, and to render a good image of collected particles.

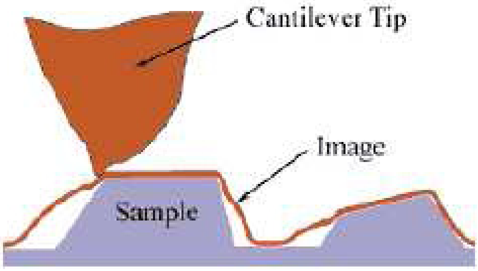

Figure 15 – Scheme of the convolution effects (Silicon-MTD Ltd).

The software produced by Silicon-MTD Ltd. is used to deconvolute the AFM images. The deconvolution aims to eliminate the particles oversized imaging that sometimes is very high because of the not negligible tip shape and size. An advanced image processing software (S.P.I.P.™, ImageMetrology) is used to analyze the deconvoluted images. This software get a virtual separation of particles from the substrate, once assigned a zero detection level to the substrate. The choice of such zero level greatly influences particles sizing. The particle will be oversized if the reference plane cut the substrate or undersized if it cut the particles. The zero level choice is performed on the shift phase images where particles contour are well defined. The software outputs are the main geometrical features of the collected particles, particularly their volume, basal area and height above the substrate. Two main parameters are used in this research:

- ✓ Equivalent Diameter (ED), the diameter of a sphere having volume equal to that of the particle;
- ✓ Aspect Ratio (AR), the height above the substrate to baseline diameter.

Results are converted in ED normalized frequency distribution and subsequently fitted by a weighted sum of lognormal distributions allowing its easy handling.

$$\frac{1}{N}\frac{dN}{dED}=\frac{1}{ED}\cdot\sum_i\frac{w_i}{\sqrt{2\pi}\cdot\log(\sigma_i)}\exp\left\{-\frac{1}{2}\left[\log\left(\frac{ED}{\langle ED_i\rangle}\right)\Big/\log(\sigma_i)\right]^2\right\} \tag{4.6}$$

4.2.1 Thermophoretic sampling

The particles, suspended in a gaseous medium subject to a thermal gradient, experiences a net force which tends to push away from high-temperature region, towards the lower temperature zone. This effect is labeled *thermophoresis* and could be explained by the gas kinetic theory as showed in Figure 16.

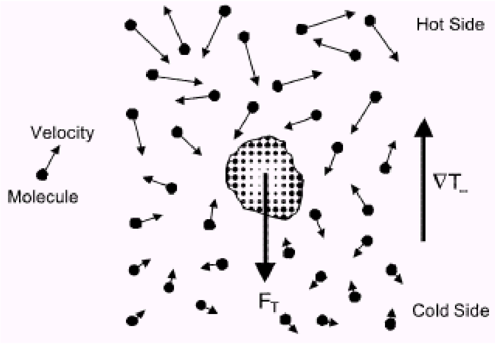

Figure 16 – Particle immersed in a not thermal uniform gaseous medium (Zheng et al., 2002)

The molecules localized in higher temperature areas have higher energy and momentum respect that site in the colder zones. Thus the collisions between gas molecules and the particle are more numerous and of higher energy level on the particles hotter side respect to those occurring on the colder side, resulting in a net thermophoretic force.

A rigorous study of thermophoresis requires the proper solution of the Boltzmann equations to calculate the molecular velocity distribution in a not uniform gas. From such distribution the thermophoretic force could be obtained integrating the momentum transfer on the particle surface. This process is fairly complicated due to the nonlinearity of the equation but a simplified approach may be followed accounting for the Knudsen number (*Kn*). It represents the molecular mean free path (λ) to particles equivalent diameter ratio.

$$Kn = \frac{2 \cdot \lambda}{ED} \tag{4.7}$$

Three different regimes of interaction between the particle and the fluid can be distinguished depending on the Kn value:

- ✓ Kn → 0, continuous regime: the gas behaves as a continuum medium respect to particles (Epstein, 1929);
- ✓ Kn ~ 1 transition or Knudsen: approximate, Boltzmann equation solutions such as the Fuchs and Sutugin solution, are required to account thermophoretic effect (Seinfeld and Pandis, 1998);
- ✓ Kn >> 1 molecular regime: each molecule interacts independently with the particles not disturbing the velocity distribution field.

Brock (1962) proposed an expression for thermophoretic force (F_{th}) depending on thermal gradient (∇T) valid throughout the *Kn* field.

$$F_{th} = 6\pi \cdot D_p \frac{\mu^2}{\rho} \cdot \frac{C_{tc}(\kappa_{gp} + C_t Kn)}{(1 + 3C_s Kn)(1 + 2\kappa_{gp} + 2C_t Kn)} \cdot \frac{-\nabla T}{T} \tag{4.8}$$

T, ρ and μ are the gas temperature, density and dynamic viscosity, respectively while κ_{gp} is the gas (κ_g) to particle (κ_p) thermal conductivity ratio. Finally C_s, C_t and C_{tc} are empirical coefficients which Talbot (1980) reported to be equal to 1.1, 2.2 and 1.2, respectively.

The balance of thermophoretic and medium resistance force allow to calculate the particles thermophoretic velocity (V_{th}) at stationary state (Rosner and Khalil, 2000).

$$V_{th} = 2\frac{\mu}{\rho} \cdot \frac{C_c(\kappa_{gp} + C_t Kn)C_{tc}}{(1 + 3C_s Kn)(1 + 2\kappa_{gp} + 2C_t Kn)} \cdot \frac{-\nabla T}{T} \tag{4.9}$$

C_c is the *Stokes-Cunningham correction factor* depending on Kn itself (Millikan, 1923).

$$C_c = 1 + Kn \cdot \left[1.257 + 0.4 \cdot \exp\left(\frac{-1.1}{Kn}\right)\right] \tag{4.10}$$

Concluding, Waldmann e Schmitt (1966) expressed the thermophoretic velocity dependence on thermal gradient (4.8) in a more compact form using the gas kinematic viscosity (ν) and the *dimensional thermophoretic factor* (K_{th}).

$$\begin{gathered} V_{th} = K_{th} \cdot \nu \cdot \frac{-\nabla T}{T} \\ K_{th} = 2 \cdot \frac{C_c(\kappa_{gp} + C_t Kn)C_{tc}}{(1 + 3C_s Kn)(1 + 2\kappa_{gp} + 2C_t Kn)} \end{gathered} \tag{4.11}$$

In the free molecular regime, that regards particles up to 500nm at flames temperature, such expression greatly simplifies and it coincides with more rigorous derivations.

$$V_{th} = 0.55 \cdot \nu \cdot \frac{-\nabla T}{T} \tag{4.12}$$

The main advantage of using a thermophoretic sampling technique is the thermophoretic sampling speed direct proportionality to the thermal gradient and its independence from the particle sizes in a wide range of particles diameter. The latter feature allows to collect a population of particles that is representative of that into the aerosol. This is the truth all particles are collected with the same efficiency.

For this reason thermophoretic sampling was widely used to collect combustion generated particles for microscopy analysis. Dobbins and Megaridis (1987) firstly used this technique to collect flame generated carbonaceous particles while Kyolu et al. (1997) developed a methodology to calculate particles volume fraction in flame from the total collect matter volume.

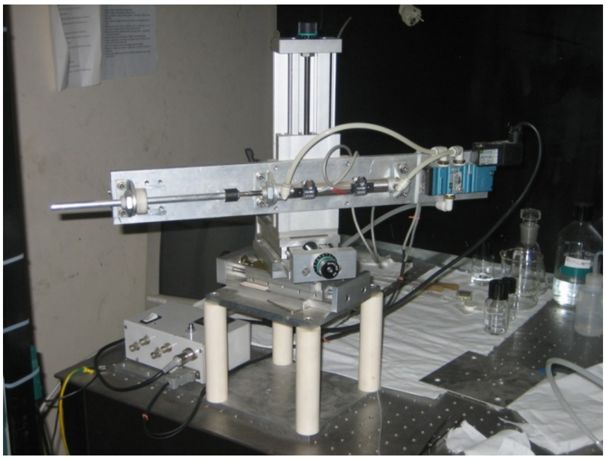

Figure 17 – The pneumatic actuator used to perform thermophoretic samplings.

The particles collecting substrate have to be impulsively inserted in the flame to perform a good sampling. The sampling time (Δt) has to be enough to collect sufficiently high number of particles but not so long to mica heating that reverse the thermophoretic effect. In addition, the flame perturbation by the substrate insertion has to be minimized. A tin substrate holder and a double acting pneumatic actuator, showed in Figure 17, were properly designed to this aims. The actuator assures a quick insertion and a constant sampling time that can be regulated by a minimum of 10ms to a maximum of 1s.

The mica disks were also inserted parallel to the gas streamline to minimize flame perturbation. Since the generated particles are within the free molecular regime, the particles thermophoretic velocity does not depend on particles size and it only depends on the thermal laminar boundary layer thickness (δ_{th}) above mica surface. Indeed, as showed in Figure 18, the temperature gradient between the gas and the substrate is $\nabla T = (T_{gas}-T_{mica})/\delta_{th}$ and depends only on the thermal laminar boundary layer thickness and, consequently, on the hot gas velocity (Hinds, 1999). We always assume mica temperature close to ambient one (T_{mica}~350K) and the boundary layer film temperature for the gasses ($T \sim (T_{mica}+T_{gas})/2$).

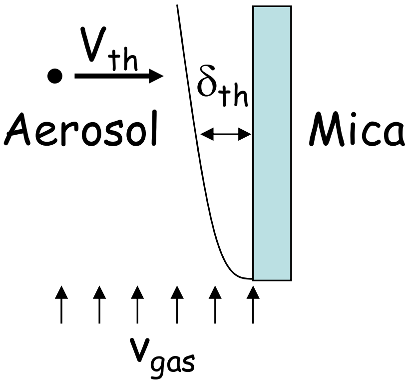

Figure 18 – Scheme of the thermophoretic sampling.

The product of the sampling time, the imaged surface (S_{im}), usually equal to 4μm^2, and thermophoretic velocity gives the aerosol sampled volume.

$$Vol_{sam} = \Delta t \cdot S_{im} \cdot V_{th} = \Delta t \cdot S_{im} \cdot 0.55 \cdot \nu \cdot \frac{-\nabla T}{T} \tag{4.13}$$

Once calculated the sampled aerosol volume it is quite easy to obtain particles volume fraction (fv_{AFM}) and number concentration (N_{AFM}) from the AFM measured particles total volume (Vol_{part}) and number (N_{part}), respectively.

$$
\begin{aligned}
fv_{AFM} &= \frac{Vol_{part}}{Vol_{sam}} \\
N_{AFM} &= \frac{N_{part}}{Vol_{sam}}
\end{aligned}
\qquad (4.14)
$$

These values agree with real fv and N only if each particle, impinging on the substrate, bonds on the substrate. Low value of adhesion/collection efficiency conducts AFM to underestimate fv and N. Furthermore, size dependent adhesion efficiency affects the shape of AFM measured size distribution overestimating the frequency of more effectively collected particles.

4.3 In situ optical diagnostics

Optical diagnostic are widely used for particles sizing and characterization from a long time (Borhen and Huffmann, 1983). They have also extensively used to perform in-situ particles measurements in flames and in combustion environments. Their major advantage respect to other diagnostic is to be highly non intrusive and non invasive. A complete overview of light interaction with matter is beyond the scope of this thesis.

A brief heuristic introduction to Rayleigh elastic light scattering theory is given to interpret the measurements results. This theory, developed in 1871, is a completely classical electromagnetic theory. It is valid only when particles are sufficiently diluted and their sizes are negligible respect to the light wavelength (λ). This is always the case for the experiments get in this research activity. In this hypothesis a particle may be seen as point induced electrical dipole. Such dipole oscillates with the same frequency of the incident electromagnetic wave. The oscillation amplitude depends obviously on incident wave strength and on particles polarizability that for homogeneous particles is proportional to their volume. An oscillating dipole is an electromagnetic wave source itself resulting in the light scattering phenomenon. The intensity of scattered light is proportional to the square of the oscillation amplitude and thus, for homogenous particles, to square of their volume or equivalently to sixth power of the equivalent diameter. The proportionality coefficient depends on particles optical properties, more in detail on its complex refractive index (m).

4.3.1 Static Laser Light Scattering

Light scattering became a powerful diagnostic with the diffusion of Laser light source. Laser light can be considered, with a good approximation, a planar monochromatic linearly polarized electromagnetic wave.

In a classical static light scattering (SLS) experiment whose typical layout is shown in Figure 33, a detector is placed in the horizontal plane in such way that the detected scattered light form a fixed angle (θ) with the exciting light that impinge on the sample with intensity I_0. The detector measures the mean intensity (I_s) of light scattered in a fixed solid angle (Δθ) by the scattering volume (ΔV_s).

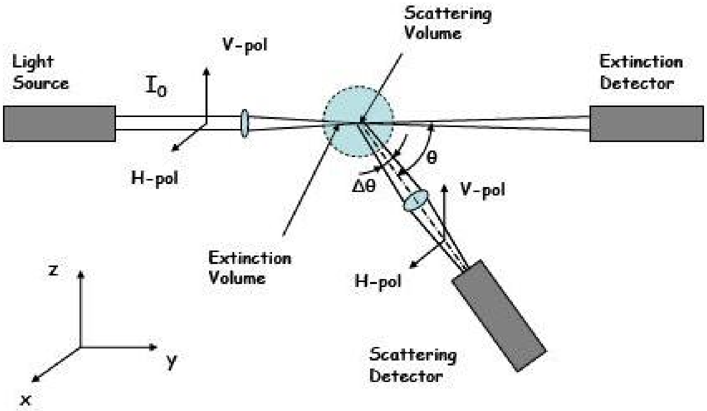

Figure 19 – Light scattering and extinction experimental set-up (Commodo, 2007).

More detailed information can be obtained measuring independently the intensities of the vertical ($I_{s,V}$) and the horizontal ($I_{s,H}$) polarized component of scattered light and using a linearly polarized monochromatic exciting light source. Thus lasers, whose polarization direction is usually chosen to be the vertical one, are widely diffused for light scattering measurements.

Light scattering measurement results are reported in term of the *Rayleigh ratio* or *differential scattering coefficient* (Q_{SI}) because its value is not affected by the experimental geometry or optical efficiency (η_{opt}). The index S and I refer to the considered polarized component of scattered and incident light, respectively.

$$Q_{SI}(\vartheta,\lambda)=\frac{I_{s,S}}{I_{0,I}\cdot\Delta V_s\cdot\Delta\Omega\cdot\eta_{opt}} \tag{4.14}$$

Obviously each particles give a contribution to the scattered light intensity and thus to the scattering coefficient. This contribution is the particles differential *scattering cross section* ($C_{i,SI}$) and it simply sum on the number of particles (n) contained in the scattering volume if they are not interacting, randomly oriented and sufficiently diluted. The result is that the scattering coefficient is proportional to the particles number concentration and to the mean value of scattering cross section.

$$Q_{SI}(\vartheta,\lambda)=\frac{1}{\Delta V_s}\cdot\sum_{i=1}^{n}C_{i,SI}(\vartheta,\lambda)=N\cdot\langle C_{SI}(\vartheta,\lambda)\rangle \tag{4.14}$$

The exact knowledge of the particles scattering cross section dependence on the scattering angle and light wavelength and it requires the solution of the Maxwell electrodynamics equations. Approximate analytical solutions exist for spherical particles and they constitute the Lorentz-Mie scattering theory.

As qualitatively described before, the particle scattering cross section is proportional to the sixth power of particles equivalent diameter when particles size are negligible respect to the light wavelength (Rayleigh limit).

$$\begin{aligned} C_{i,VV} &= \frac{\pi^4}{4\lambda^4}\cdot\left|\frac{m_i^2-1}{m_i^2+2}\right|\cdot ED_i^6 \\ C_{i,HH} &= C_{i,VV}\cdot\cos(\vartheta)^2 \\ C_{i,VH} &= C_{i,HV} = 0 \end{aligned} \tag{4.14}$$

Once assumed the complex refractive index to be uniform among the particles, the scattering coefficient is proportional to their number concentration and to the mean value of the ED sixth power. It can be also expressed proportional to particles volume fraction and to the ratio between the sixth and the third moment of the size distribution, considering the relation: $fv = \frac{\pi}{6}\left\langle ED^3 \right\rangle \cdot N$.

$$Q_{VV} = \frac{\pi^4}{4\lambda^4} \cdot \left| \frac{m^2 - 1}{m^2 + 2} \right| \cdot N \cdot \left\langle ED^6 \right\rangle = \frac{3\pi^4}{2\lambda^4} \cdot \left| \frac{m^2 - 1}{m^2 + 2} \right| \cdot fv \cdot \frac{\left\langle ED^6 \right\rangle}{\left\langle ED^3 \right\rangle} \tag{4.15}$$

4.3.2 Light Extinction

The intensity of light crossing a medium decreases with an exponential law by increasing the distance from its source (x), because of two reasons. Light can be absorbed by the medium itself and it is scattered in all the directions resulting in the attenuation of the propagating wave. Two coefficients, the *absorption* (K_{abs}) and *scattering* (K_{sca}) *coefficients*, account for both the effect and their sum is the total exponential decay rate coefficient, i.e. the extinction coefficient (K_{ext}), in the well known *Lambert Beer law*.

$$\frac{I(x)}{I_0} = \exp\left[- K_{ext} \cdot x\right] = \exp\left[- \left(K_{abs} + K_{sca}\right) \cdot x\right] \tag{4.16}$$

This law also constitute the tool to calculate the extinction coefficient from experimental measurements of light intensity before (I_0) and after ($I(x)$) crossing the medium. Obviously this calculus requires the knowledge of the distance that light cover crossing the medium, better known as *optical path*.

The scattering coefficient is simply equal to the integral, on all scattering angle, of the differential scattering coefficient.

The absorption, similarly to scattering, coefficient is the sum of particles *absorption cross section* accounting to each particles contribution to light absorption.

$$K_{abs}(\lambda) = \frac{1}{\Delta V_{abs}} \cdot \sum_{i=1}^{n} C_{i,abs}(\lambda) = N \cdot \langle C_{abs}(\lambda) \rangle \qquad (4.14)$$

In the Rayleigh limit the absorption cross section is proportional to particles volume thus to the third power of the equivalent diameter.

$$C_{abs} = \frac{\pi^2}{\lambda} \cdot \mathrm{Im}\left\{ \frac{m_i^2 - 1}{m_i^2 + 2} \right\} \cdot ED_i^3 \qquad (4.14)$$

Moreover in such condition of small and diluted particles the scattering coefficient is negligible respect to the absorption coefficient. Thus the particles volume fraction can be easily calculated from the measured extinction coefficient once assumed the complex refractive index to be uniform among the particles.

$$K_{ext} = K_{abs} = \frac{-\pi^2}{\lambda} \cdot \mathrm{Im}\left\{ \frac{m^2 - 1}{m^2 + 2} \right\} \cdot N \cdot \langle ED^3 \rangle = \frac{-6\pi}{\lambda} \cdot \mathrm{Im}\left\{ \frac{m^2 - 1}{m^2 + 2} \right\} \cdot fv \qquad (4.14)$$

4.4 Differential Mobility Analysis

The Differential Mobility Analyzer (DMA), also known as Scanning Mobility Particles Sizer (SMPS), determines the size distribution of charged particles classified according to their electrical mobility. It is traditionally used to study both the combustion generated and atmospheric particles.

Recent advances in technology have extended the DMA range measurements to sizes smaller than 1nm, promoting the DMA as a privileged diagnostic in studying the processes of gas to particles transition.

A DMA classifies charged particles through their motion, induced by electric fields. It selects and count particles in relation to their electrical mobility. Then the particle size distribution can be obtained using appropriate models expressing electrical mobility dependence on particles size.

A DMA is essentially composed of three components: a neutralizer, an electrostatic classifier and a detector.

- ✓ The neutralizer provides to charge particles with a known steady state charge distribution. It usually is a bipolar diffusion charger equipped with a radioactive source releasing the ions into the aerosol. The particles and ions frequent collisions, due to their thermal motion, provide the particles charging (Covert et al., 1997). The main difference among neutralizers consists in their geometry and the ion source, affecting the charging efficiency and, the latter, the steady state charge distribution reproducibility.
- ✓ The electrostatic classifier acts as a filter, selecting particles respect to their electrical mobility and it is schematically shown in Figure 21. It was made of two coaxial cylinders acting as electrodes. The outer cylinder is electrically grounded while the inner one is keep at high voltage. A sheet carrier gas, commonly air, flow through the cylinders. The charged aerosol is injected in from the external cylinder. The electric field, generated by the internal cylinder voltage, induces the charged particles electrophoretic radial motion. The parabolic particles trajectory curvature depends on the gas flow rate and on the particles electrical mobility. The particles with right mobility through the internal electrode slit being selected among the other. The right electrical mobility can be adjusted varying the internal cylinder voltage. The electrostatic classifier resolution mainly depends on its geometry and on the internal streams flow rate.
- ✓ The detector function is to count the selected particles. It can be an electrometer or a Condensation Nucleus Counter (CNC). A CNC is based on charged particles growth by heterogeneous condensation, usually of water or some alcohol, up to size allowing their numerical count by LLS. The CNC have a high sensitivity but, usually, its detection efficiency decrease for size below 5nm (Sgro et al., 2003). The electrometer directly measures the charge thus its detection efficiency does not depend on particles size but its sensitivi-

ty is about three orders of magnitude lower than a CNC. Moreover it allows to be placed just at the classifier exit minimizing the particles losses.

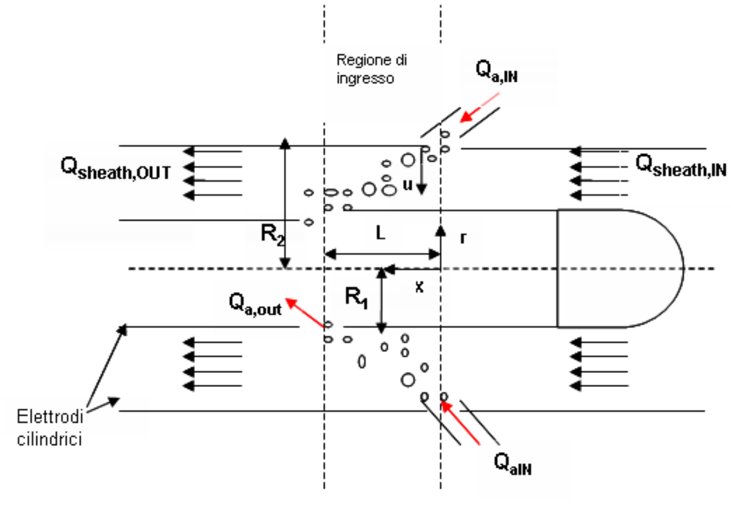

Figure 20 – Scheme of an electrostatic classifier.

Two DMAs are used in this research activity. The widely used is a TapCon DMA 3/150, commonly known as Vienna DMA, with a nominal measurements range between 0.6nm and 28nm or between 2.1nm and 100nm depending on the operating modality. The other is a TSI SMPS model 3936, also known as Nano DMA, with a nominal measurements range between 3nm and 50nm. Their major characteristics are reported in Table 4.

Table 4 – **Major characteristics of used DMAs**.

	TSI 3936	TapCon 3/150
Neutralizer	Bipolar Kr-85	Bipolar Am-241
Sheet flow	20 l/min	50 l/min
Aerosol flow	1.5l/min	5l/min
Detector	Butyl alcohol CNC	Faraday cup Electrometer

A key feature in operating with a DMA is the choice of the aerosol sampling system. It have to be designed in order to maximize the quenching of physical and chemical transformation invalidating the analysis results, such as coagulation, that could occur while the aerosol is carried from the sampling to measurement point.

4.4.1 Electrical mobility dependence on diameter

The electrical mobility (*Z*) is defined to be the ratio between the speed (u) of a charged particle in a gas, induced by an electric field E, and the electric field itself.

$$\vec{u} = Z \cdot \vec{E} \tag{4.15}$$

The relationship between particles electrical mobility and diameter, in the size range below 5nm, was the subject of many theories existing in literature, all assuming particles spherical shape. They are graphically summarized in Figure 21 showing their discrepancy.

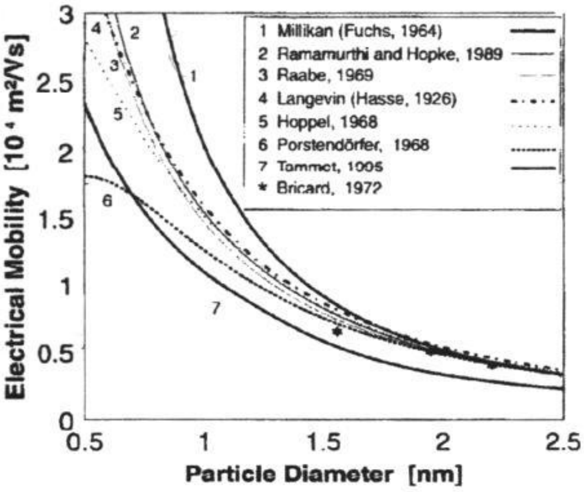

Figure 21 – Discrepancy among several theories in predicting the electrical mobility of particles in the size range below 5nm (Makela et al., 1996).

The Millikan-Fuchs theory is the widely used and it express the ED dependence of the electrical mobility of a particles with a known number (*n*) of elementary electron charge (*e*) moving in viscous (μ) medium.

$$Z = \frac{n \cdot e \cdot C_c}{3\pi \cdot \mu \cdot ED} \tag{4.16}$$

C_c is the Cunningham correction factor whose dependence on Knudsen number is reported in the equation 4.10. In the free molecular limit (Kn>>1) such relation simplify expressing, with the Stokes-Einstein relation, the gaseous medium viscosity (μ) in term of its molecular weight (*m*), Boltzmann constant and gas pressure (*P*).

$$Z = \frac{0.441 \cdot n \cdot e \cdot \left(\frac{K_B T}{m} \right)^{1/2}}{P \cdot MD^2} \tag{4.17}$$

Anyway experimental results showed that the Millikan-Fuchs theory falls in predicting the electrical mobility for ED smaller 10nm (Fernandez de la Mora et al., 1998). For this reason the diameter calculated using the relation (4.17) is commonly labeled *Mobility Diameter* (MD) and it slightly differs from ED.

These experimental results induced Tammet (1995) to develop a new theory expressing the electrical mobility of particles smaller than 5nm. This theory accounts some effects neglected by the Millikan-Fuchs relation. First of all the induced dipole particles interaction were considered. The main point developed in this theory is a detailed description of the molecule interaction with particle accounting for the effective spherical diameter (D_0) of the gaseous medium molecule and the transition from elastic to inelastic interactions. The resulting effect is that the Mobility Diameter of the Millikan-Fuchs theory differs from the Equivalent Diameter because of the carrier gas effective diameter.

$$\begin{gathered} MD = D_0 + ED \\ Z = \frac{0.441 \cdot n \cdot e \cdot \left(\frac{K_B T}{m} \right)^{1/2}}{P \cdot (D_0 + ED)^2} \end{gathered} \tag{4.18}$$

The accounted effects give a significant contribution only for particles ED smaller than 3nm. Indeed the air effective diameter evaluated to be $D_0 \approx 0.6$nm and 0.53nm by Tammet and de la Mora, respectively.

4.4.2 Sampling probes

A great number of on-line sampling probes were developed simultaneously the growing use of DMAs. Burtscher et al. (1993) firstly used capillary quartz to sample flame generated soot. His microprobe allowed a high dilution with air to minimize particles coagulation causing negligible flame disturbance but it quickly became clogged. Siegmann et al. (1995) has further developed the Burtscher microprobe. He increased the measurements spatial resolution by placing the probe perpendicular to the flow.

Subsequently Kasper and Siegmann (1997) proposed an alternative probe consisting of a horizontal stainless steel tube equipped with a pinhole in correspondence of the flame. The aerosol were sampled through the pinhole by creating a slight underpressure in the probe, monitored by two gauges positioned upstream and downstream the pinhole itself. The horizontal set-up mainly shows operating and economic advantages.

Zhao et al. (2003) used a probe similar to that of Kasper to study a laminar premixed flame of ethylene-oxygen-argon. He systematically investigated the probing dilution influence on measurements results and showed local cooling effect of the probe. Zhao et al. (2005) also measured the particle size distribution of TiO_2 nanoparticles generated in a laminar premixed flame doped with titanium tetraisoproxide.

The probes used in this research activity were developed starting from that designed by Zhao. They consist of a 1mm thin, 260mm long stainless steel tube with an internal diameter of 8mm, placed horizontally on the burner. The tube thickness is reduced to 0.5mm in the sampling area where a pinhole was drilled. The probes differ in the pinhole diameter. Three probes are realized with 0.3mm, 0.5mm and 0.7mm pinhole diameters, respectively. The sampling pinhole was vertically aligned on the flame axis while performing the measurements. The probes are also equipped with a water cooled heat exchanger.

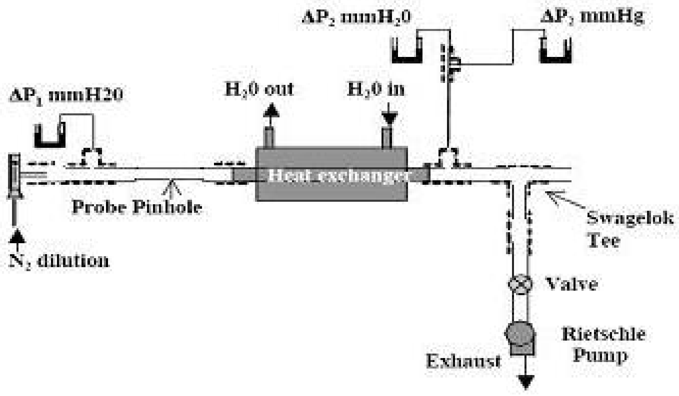

Figure 22 – Scheme of probe operation (De Filippo, 2008).

The aerosol was sampled from the flames by creating an appropriate underpressure near the hole and it is suddenly diluted in the pure nitrogen flowing in the tube. The heat exchanger provides the cooling of aerosol to be analyzed when required.

The nitrogen flow was steady because of the critical orifice placed upstream the probe. It may be adjusted regulating the fed nitrogen pressure and values between 17.6Nl/min and 29.5Nl/min were used in this research activity. The corresponding Reynolds numbers were between 3000 and 5000 and indicate a completely developed turbulent flow.

The flow in excess respect that required by the DMA, is sucked away from the probe by a vacuum pump (Rietschle Thomas, Type VTE8). The sucked flow, manually regulated with a needle valve, also provide the slight underpressure into the probe. Such underpressure was monitored by two water gauges inserted immediately upstream (ΔP_1) and downstream (ΔP_2) the pinhole, respectively. The sampled aerosol flow can be changed approximately from 1ml/min to 10ml/min depending on the underpressure and on the pinhole diameter. The designed probes allowed using a wide range of Dilution Ratio (DR) comprised between 3000 and 30000.

4.5 Scanning Electron Microscopy

Scanning Electron Microscopy (SEM) with Energy Dispersive X-ray Spectrometry (EDXS) is also performed to analyze generated particles. The used SEM is the Philips XL30 SEM with a LaB6 filament equipped with an EDS DX-4i microanalysis.

Particles are deposited or thermophoretically collected on aluminum substrates using the pneumatic actuator previously described in the paragraph 4.2.1. A conductive substrate is always required for SEM analysis. The substrate roughness is not controlled because nanoparticles imaging, using this technique, is beyond the scope of this research.

Two different kind of analysis may be performed both based on scattering of the electron beam focused on the sample and generated by a LaB6 filament. They are:

- ✓ secondary electron detection;
- ✓ backscattered electron detection.

The secondary electrons technique is based on low energy electrons (<50eV) generated at a distance of a few nanometers from the surface. The electrons are detected by a photomultiplier. The two-dimensional intensity distribution is converted in a digital image.

The backscattering technique consists in generating high energy electrons which are reflected or backscatter by the sample. Obviously the analysis involve a sample surface layer some tens of microns in thickness. This technique highlights areas with different chemical composition because the reflected electron energy increases with increasing atomic number.

The sample elemental chemical analysis can be performed detecting the reflected X-rays energy spectrum through the use of the EDXS.

Chapter 5

Metal nitrates doped premixed flame

Some of the results reported in this chapter were presented at:

32nd Symposium on Combustion of The Combustion Institute, 3-8 Agosto 2008, McGill University, Montreal, Canada: Carbone, F., Barone, A., Beretta, F. , D'Anna, A. and D'Alessio, A., *Size Distributions of Nanoparticles Generated from Droplets of Metal Nitrate Aqueous Solutions in Combustion Environments*;

10th International Congress on Combustion by-Products and their Health Effects, 17-20 Giugno 2007, Ischia, Italy, in press on Environmental Engineering Science: Carbone, F., Barone, A., Pagliara, R., Beretta, F. , D'Anna, A. and D'Alessio, A., *Ultrafine Particles Formed by Heating Droplets of Simulated Ash Containing Metals* (Carbone et al. 2008a).

5.1 Operating conditions

A stoichiomentric flat laminar premixed flame of ethylene/air (cold gas flow velocity of 80 mm/s) is stabilized on a water-cooled porous-plug brass burner (McKenna Products) drilled on its axis where a 7.5mm ID stainless-steel tube is inserted. Approximately 40μm monodisperse droplets of metal nitrate solutions, dispersed into 600cm^3/min of air to prevent their coalescence, are coaxially fed into the flame through the tube. The droplets are generated by a Berglund-Liu-type Vibrating Orifice Aerosol Generator (model 3450, TSI) using a 20μm orifice oscillating at a frequency of 60KHz. The solution flow is 0.139cm^3/min but about 30% is lost in the adduction tube, not reaching the flame. This amount is properly drained and quantified.

The system is analyzed using three aqueous solutions with 25% mass concentration of cadmium nitrate ($Cd(NO_3)_2$), nickel(II) nitrate ($Ni(NO_3)_2$) and lead(II) nitrate ($Pb(NO_3)_2$). The solutions are prepared dissolving into bidistilled water cadmium nitrate tetrahydrate ($Cd(NO_3)_2$-$4H_2O$), nickel(II) nitrate hexahydrate ($Ni(NO_3)_2$-$6H_2O$) and $Pb(NO_3)_2$ salts, respectively. These nitrates are chosen because they are quite soluble in water and the metals they contain both cover a wide range of volatilities and are of relevance concerning pollution (Linak and Wendt, 1993). Table 5 reports the metal and their possible products physical properties.

Table 5 – **Metal nitrates and their possible products selected physical properties.**

	Chemical Formula	MW [g/mol]	Melting point [K]	Boiling Point [K]	Solubility %wt (25°C-100°C)	Density [g/cm^3]	m(532nm)
Precursors	$Cd(NO_3)_2$	236.4	633		61.0-87.4	3.6	
	$Ni(NO_3)_2$	182.7			49.8-69.0		
	$Pb(NO_3)_2$	331.2	743		37.4-56.8	4.5	
Possible products	Cd	112.4	594	1040	insoluble	8.6	0.75+4.8i
	CdO	128.4		1832sub	insoluble	8.1	2.5
	Ni	58.7	1728	3186	insoluble	8.9	1.6+3.1i
	NiO	74.7	2230		insoluble	6.7	2.3
	Pb	207.2	600	2022	insoluble	11.3	1..9+2.5i
	$PbO^{Massicot}$	223.2	1163	1750	insoluble	9.6	2.6

The addition of the solution droplets into the flame involves the appearance of a light emitting jet whose flickering, due to external perturbations, is reduced placing a flat plate at 40mm of height above the burner (HAB). This stabilizer is interested by powder deposition not significantly influencing the observable flame structure. An image of the flame and the reactor scheme is shown in Figure 23.

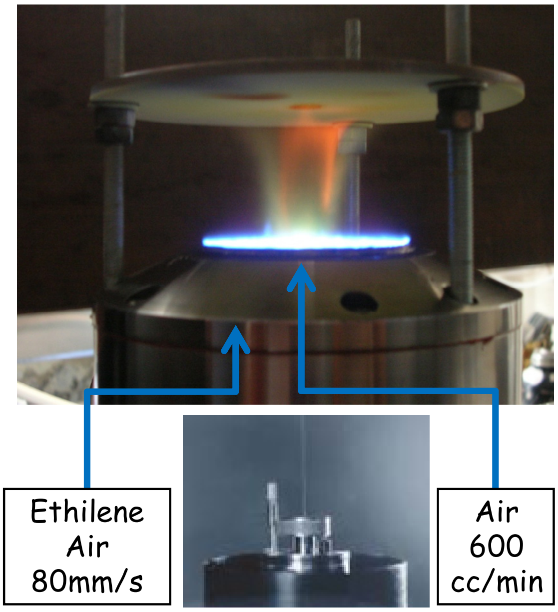

Figure 23 – Doped flame reactor layout. The picture is captured using the $Pb(NO_3)_2$ solution.

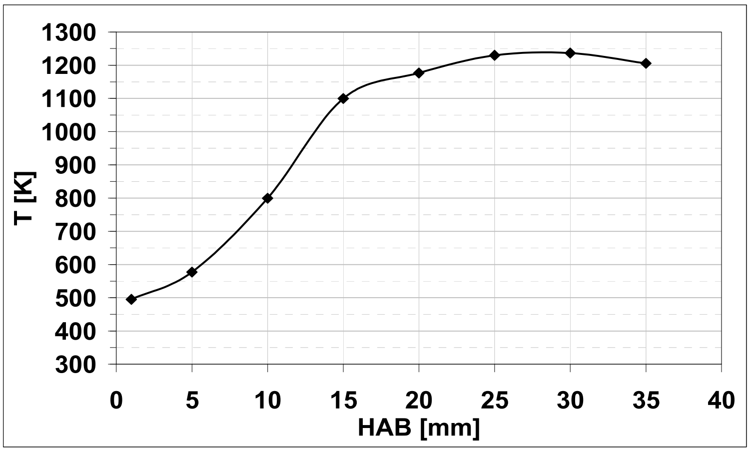

Figure 24 – Axial temperature profile.

Table 6 – **Particles residence time in flame.**

HAB [mm]	20	25	30	35
RT [ms]	20	24	28	32

Flame temperature was measured along the axis by a 125μm Pt/Pt-13%Rh thermocouple (Type R, Omega Engineering), feeding bidistilled water despite solutions to prevent metal particles deposition on the measurement junction. Temperature increases from the droplets injection point to HAB=20mm. Downstream this position it remains almost constant around ~1200K as shown in Figure 24. The evaporation of droplets completes just upstream HAB=20mm, corresponding to a residence time in the flame (RT) of ~20ms. Particles RTs estimated at HABs where samplings were performed were reported in Table 6.

5.2 Performed analysis

Plasma generated in air was used as incoherent light source for the UV-Vis extinction measurements to calculate volume fraction of particles obtained from lead(II) nitrate solution. The plasma is produced by tightly focusing, with an 8 mm F.L. lens, the energy of a Q-switched Nd:YAG laser beam (λ= 1064nm, energy E = 200mJ) leading to an optical breakdown. The light emission from the plasma has an exceptionally high photon flux and a broadband and unstructured spectrum spreading from visible to deep ultraviolet (Borghese and Merola, 1998). The transmitted light intensity is measured by a spectrometer coupled to an intensified and gateable CCD camera. The optical path length was estimated by measuring the radial dimension of the powder layer deposited on the flame stabilizer and of flame light emission. The obtained value of optical path length is used to calculate the extinction coefficient (K_{ext}) from measured signals. The particles volume fraction (fv) was calculated with the Rayleigh approximation.

An expected particles volume fraction (fv_{Ex}), constant along flame axis, by a material balance of fed metal, was also calculated considering that one of the possible products is generated. The particles density was supposed equal to that of bulk material but the main approximation is that metal disperses into 5% of total reacting flow. These assumptions are justified because the value thus calculated agrees with that measured by light extinction using the $Pb(NO_3)_2$ solution (Carbone et al., 2008a).

Particles were thermophoretically collected on mica muscovite disks (3mm diameter) inserted parallel to the gas streamline using a properly designed pneumatic actuator that assures a quick insertion and a constant sampling time (Δt~30ms). Thermophoretic samplings were performed at several HABs to perform AFM images analysis. The obtained size distribution were fitted by a weighted sum of two lognormal distributions, with w_i the weight of the i^{th} mode (obviously $\Sigma w_i=1$). This fitting allows the easy handling of results:

$$\frac{1}{N}\frac{dN}{dED}=\frac{1}{ED}\cdot\sum_i\frac{w_i}{\sqrt{2\pi}\cdot\log(\sigma_i)}\exp\left\{-\frac{1}{2}\left[\log\left(\frac{ED}{\langle ED_i\rangle}\right)\Big/\log(\sigma_i)\right]^2\right\} \tag{5.1}$$

Once obtained the ED distribution, the particles number concentration (N) was evaluated from fv_{Ex}. With this value, it was possible to calculate the particles Brownian collision rate (K_{gk}), due to their gas kinetic thermal motion. Finally, in the case that particles were not too much polidisperse, it was assumed that they are monomodal with sizes equal to that of the first mode. If each collision involve coagulation, this assumption allowed to calculate particles half-life (t_{half}) using the Smoluchosky equation (Hinds, 1999). The mean particles coagulation efficiency (γ_{coag}) was calculated as the gas kinetic to the experimentally observed half-life ratio:

$$\gamma_{coag}=\frac{t_{half}^{gk}}{t_{half}} \tag{5.2}$$

A particles volume fraction (fv_{AFM}) was calculated from the total volume of collected particles measured by AFM. The particles adhesion/collection efficiency (γ_{adh}) was evaluated performing the ratio of collected particles total volume to total volume of particles that thermophoretic force drives to impinge on the substrate (V_{imp}). The latter was simply obtained from fv_{Ex} considering the thermophoretically sampled aerosol volume. The γ_{adh} thus calculated is the mean value on the entire particles ED distribution and it is simply equal to the fv_{AFM} to fv_{Ex} ratio:

$$\gamma_{adh} = \frac{V_{part}}{V_{imp}} = \frac{V_{par}}{fv_{ex} \cdot V_{sam}} = \frac{fv_{AFM}}{fv_{ex}} \tag{5.3}$$

In-situ LLS measurements were performed on the flame axis at several HABs to check the sampling influenced AFM results. Indeed AFM distribution underestimates the normalized frequency of less effectively collected particles. Then the ED63 calculated by AFM ED distribution could be quite different respect to measured LLS ED63. Particularly it will be much higher if larger particles are collected more effectively. The light source was the second harmonic of a Q-switched vertically polarized Nd:YAG laser (λ=532 nm). The vertically polarized component of scattered light was detected by a spectrometer coupled to an intensified and gateable CCD camera, placed in the horizontal plane at 90° with respect to the laser beam, and it was converted into the scattering coefficient (Q_{VV}). Since generated particles are much smaller than the light wavelength, the Rayleigh approximation was applicable. Thus, knowing fv and assuming spherical particles, it was possible to calculate the cubic root of sixth to third moments of size distribution ratio (ED63):

$$ED63 = \frac{\langle ED^6 \rangle}{\langle ED^3 \rangle} = \frac{2\lambda^4}{3\pi^3} \cdot \left| \frac{m(\lambda)^2 + 2}{m(\lambda)^2 - 1} \right| \cdot \frac{Q_{VV}(\lambda)}{fv_{Ex}} \tag{5.4}$$

The bulk complex refractive indices (m(532nm) in Table 5) were used to this aim. ED63 values are calculated for each possible product to account measurements uncertainty.

Preliminary Differential Mobility Analysis of particles obtained from lead(II) nitrate solution were performed with the model 3936 Scanning Mobility Particles Sizer (TSI inc.), with lower detection limit of 3nm, on aerosol drawn from the edge of the flame off-axis, 30 mm from the centerline of the burner and at HAB=25mm, without any dilution to prevent coagulation. The sampling flow rate is 1.5lpm and the residence time in the sampling line was about 2s.

Particles were also collected on an aluminum substrate rapidly inserted on the flame axis at HAB=30mm. This sample was then examined by a Philips XL30 SEM with a LaB6 filament equipped with an EDS DX-4i microanalysis device.

5.3 Lead (II) Nitrate results

Many of the results reported in this paragraph were presented at 10th International Congress on Combustion by-Products and their Health Effects, 17-20 Giugno 2007, Ischia, Italy and were in press on Environmental Engineering Science: Carbone, F., Barone, A., Pagliara, R., Beretta, F. , D'Anna, A. and D'Alessio, A., *Ultrafine Particles Formed by Heating Droplets of Simulated Ash Containing Metals* (Carbone et al. 2008a).

5.3.1 Uv-vis extinction measurements

UV-Vis broadband absorption measurements are performed at several HABs along the diameters of the flame and corrected by $Pb(NO_3)_2$ free flame measured extinction. Once estimating the optical path length, the extinction coefficient was calculated and it was showed in Figure 25. It was in agreement, in the spectral range between 320 nm and 400nm, with that expected from Rayleigh approximation assuming pure liquid lead bulk refractive index.

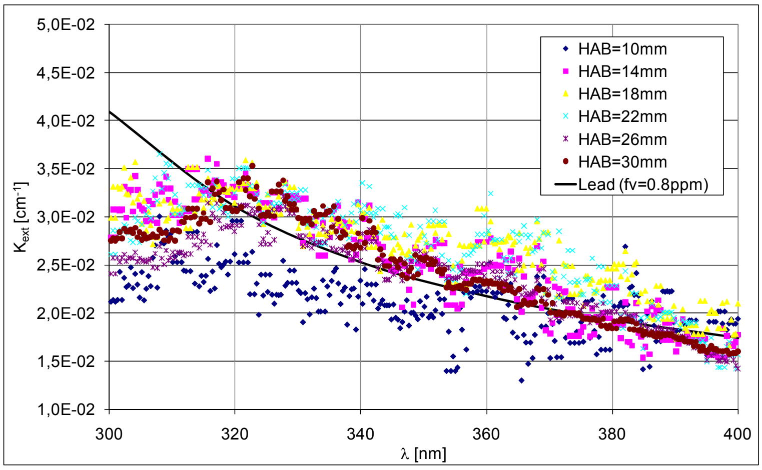

Figure 25 – Measured (point) and Pb particles Rayleigh (solid line) extinction spectrum.

The calculated volume fraction profile along the flame axis is reported in Figure 26. It is almost constant around the value of 0.8ppm. The fv_{Ex} excellently agrees with this value and it is 0.85ppm assuming pure lead particles were generated while the calculated fv_{Ex} of 1.2ppm of massicot lead(II) oxide (PbO) particles is just slightly larger.

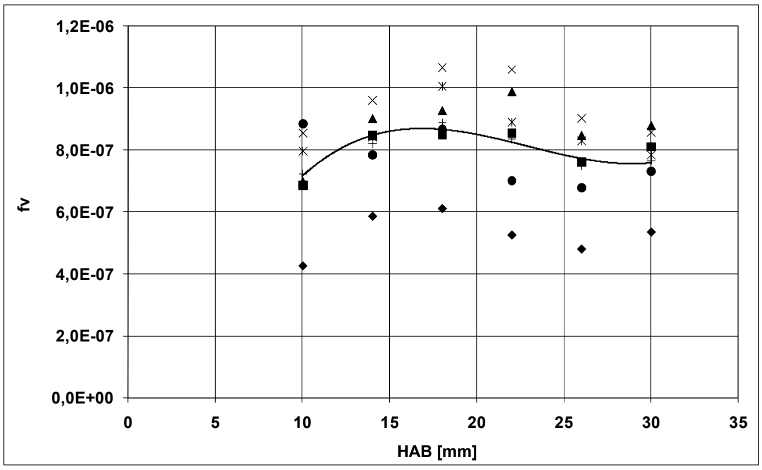

Figure 26 – Particles volume fraction obtained by UV-vis extinction measurements, $Pb(NO_3)_2$.

5.3.2 AFM results

AFM images of samples collected upstream HAB=20mm, shows nanoparticles in a size range from 2.5nm to 13nm emerging from objects having much larger volume, probably not completely evaporated droplets. The presence of not fully evaporated droplets prevents accurate particles sizing and the number of collected particle is not enough to perform a quantitative analysis but just to obtain qualitative information. One of this image is reported in Figure 27 where is also shown a scheme of the possible reason for this image. The speculation was that near saturation conditions $Pb(NO_3)_2$ nucleates close to the droplet surface because of its fast not-uniform heating. They can just slightly grow and coagulate in the liquid medium before to be released in the gas because of left water fast vaporization. This speculation that nanoparticles of some salts may nucleate into solution droplets injected in premixed flames was already proposed in literature (Limaye and Helble, 2002).

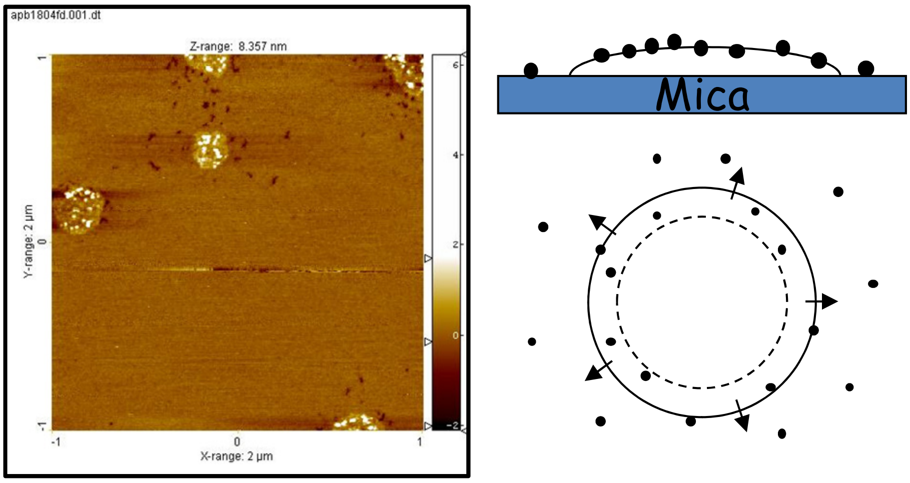

Figure 27 – AFM image of matter sampled at HAB=18mm (right side) and a scheme of nanoparticles formation pathway (left side)

Downstream HAB=20mm AFM images show from 160 to 320 particles/µm^2 on the substrate, depending on the sampling point. Figure 28 shows both an analyzed AFM image and the obtained size distributions with their best fittings (parameters in Table 7). A bi-modal size distribution results at each sampling point. At HAB=20mm the first mode (75% of particles number) has 6.3nm Mean Equivalent Diameter (MED) and 2.7nm Standard Deviation (SD) while a 15.4nm MED and 7.1nm SD second mode is observed. The same size distribution is obtained at HAB=25mm. At HAB=30mm the first mode has a quite smaller MED (4.4nm) and SD (1.5nm) and contains a slightly increased percentage (77%) of particles number. Slightly smaller MED (15.2nm) and SD (6.4nm) are obtained also for the second mode. A further significant reduction of MED and SD of each mode (2.9nm and 12.6nm MD and 0.8nm and 4nm SD, respectively) is observed at HAB=35mm where the relative number of particles into the first mode further increases (80%).

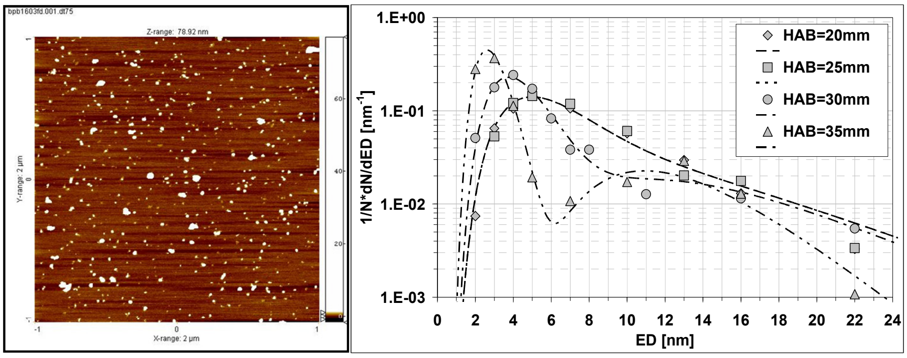

Figure 28 - AFM image of the sample at HAB=20mm (left side) and obtained size distributions, $Pb(NO_3)_2$ (right side, points AFM image analysis, dashed lines best fitting).

Table 7 – **Size distributions fitting parameters, $Pb(NO_3)_2$.**

HAB [mm]	w_I	$<ED_I>$ [nm]	$<ED_{II}>$ [nm]	σ_I	σ_{II}
20	0.75	5.8	14	1.5	1.55
25	0.75	5.8	14	1.5	1.55
30	0.77	4.2	14	1.4	1.5
35	0.8	2.8	12	1.3	1.36

The measured ARs, plotted in Figure 29, seem to be correlated with ED and values ranging from 0.01 to 0.84, at HAB=20mm, and from 0.01 to 0.21, at HAB=25mm, are observed. At HAB=30mm, AR are lower than 0.03 for first mode particles (ED<6nm) and they range from 0.01 to 0.21 for the second mode. At HAB=35mm the first mode (ED<5nm) particles AR range from 0.02 to 0.08. The second mode particles AR are no more clearly correlated with ED and they range from 0.05 to 0.23. An almost circular shaped base of collected particles was observed, suggesting that the particles could be spherical in the flame but they deform on impinging on the substrate because of a liquid like behavior.

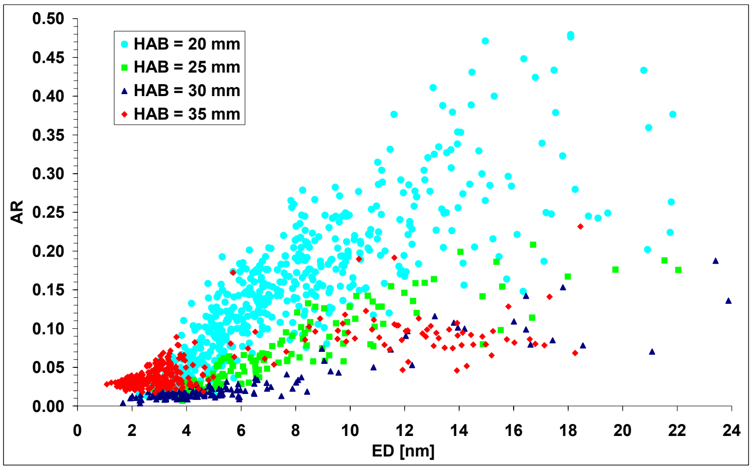

Figure 29 – Particles aspect ratios, $Pb(NO_3)_2$.

The AR lowering, at HAB=25mm, suggests a sort of nanoparticles melting. The particles of both mode shrinking, at HAB=30mm, is justified by $Pb(NO_3)_2$ decomposition to PbO (690K-810K) (Stern 1972) and its subsequent partial evaporation. Indeed the size reduction is compatible with the particles loss of mass involve in $Pb(NO_3)_2$ to PbO decomposition. The second mode particles slower shrinking may be due their lower specific surface area slowing nitrides release. The PbO cannot further thermally decompose at 1200K. Then, thermal decomposition is unable to explain the further size reduction or the progressive relative number increase of smallest particles. For this reason, it seems plausible to assume that the PbO vapor suffers successive homogeneous nucleation generating ~2.5nm particles, at HAB=35mm, where the temperature slightly drops. Also particles bursting, due to explosive decomposition could explain this behavior.

The fv_{AFM}, whose ratio with PbO fv_{Ex} is plotted versus HAB in Figure 30, decreases from ~16.5% to ~2.5% of fv_{Ex}, with increasing HAB, simultaneously with particles size decrease. Upstream of HAB=30mm, the fv_{AFM} is lower than expected also because lead compounds in gas-phase reduce particulate matter amount. The further fv_{AFM} decrease of about one order of magnitude, at HAB=35mm, can be attributed only to lowering of particles sizes because of a size dependent adhesion efficiency quickly decreasing for ED smaller than 5nm. Indeed this ratio represents the mean value of collection/adhesion efficiency on the entire size distribution.

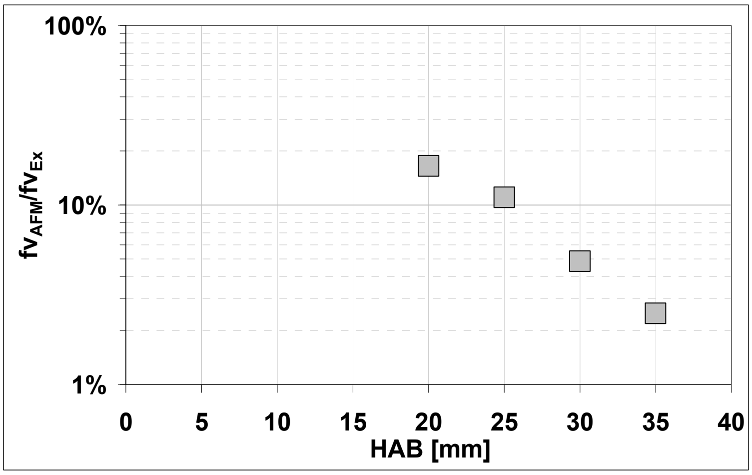

Figure 30 – Mean particles adhesion efficiency versus HAB, $Pb(NO_3)_2$.

5.3.3 LLS results

In-situ measured LLS ED63, shown in Figure 31, slightly decreases with increasing RT because particles shrink faster than coagulate. This behavior could be related to a very low coagulation efficiency of smaller particle. Surprisingly the LLS ED63 is quite smaller than that calculated by AFM ED distribution. D'Alessio et al. (2005) observed a similar discrepancy for carbonaceous nanoparticles which they explained assuming that the number concentration of smallest particles into the flame is much higher than that measured by the particles collected on the substrate. Even the ED63of the first mode of AFM distribution, containing particles with ED larger than 5nm, overestimates LLS ED63 because of the decreasing adhesion efficiency below 5nm already observed with AFM measurements. The in-situ measured value excellently agrees with ED63 calculated using only the branch of AFM distributions with ED smaller than 5nm confirming that such small nanoparticles have a much higher frequency into the flame than that collected on the substrate. Nanoparticles adhesion efficiency quickly decreases with particles size below 5nm. Particles smaller than 5nm are almost the totality of particles in the flame. Moreover, Fig.12 shows that LLS ED63 does not grow with increasing RD because of very low particles coagulation efficiency for monodisperse particles of ~3nm in size detected by LLS. On sample collected upstream HAB=35mm, such small particles may be hidden to AFM imaging because very larger particles are more effectively collected. The monodisperse ~3nm particle detected by LLS have N~8*10^{13}cm^{-3} to account for PbO fv$_{EX}$. Their gas kinetic half-life is ~25μs but LLS detect the same size at all HAB after RT ~12ms. Thus the ~3nm particles coagulation efficiency could be between two and three orders of magnitude lower than unity if other processes such as fragmentation or evaporation are not active.

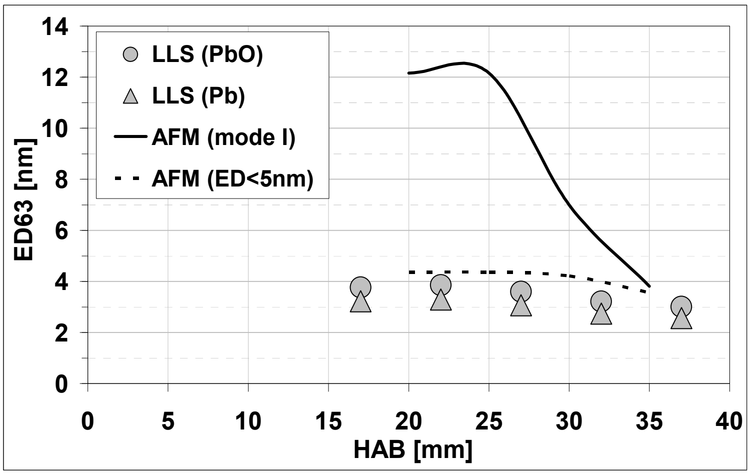

Figure 31 – LLS and AFM measured mean particles diameter versus HAB, $Pb(NO_3)_2$.

5.3.4 DMA results

To verify the supposed low coagulation efficiency of smaller particles we performed a preliminary DMA measurement on aerosol drawn from the edge of the flame without any dilution. The measured size distribution is plotted in Figure 32. The background air signal is also reported. In spite of a very long residence time (≈2 s) in the sampling line and the decreasing detection efficiency of instrumentation below 5 nm, the number of particles smaller than 10 nm is much higher than larger ones. Persistence of smaller particles is probably due to their low coagulation efficiency also in the sampling probe.

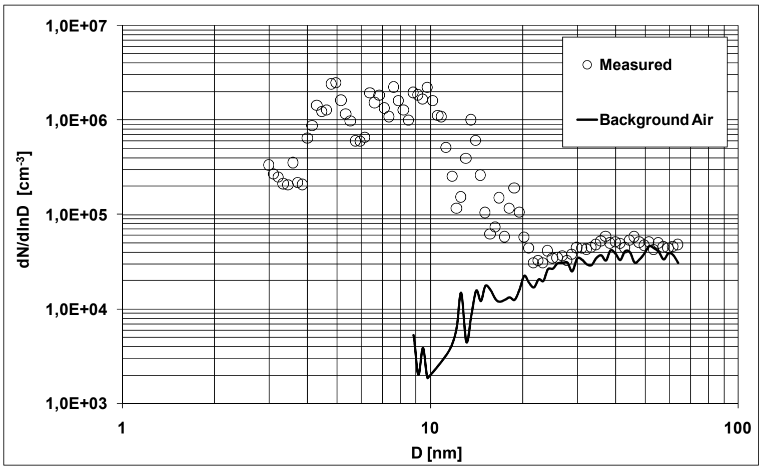

Figure 32 – DMA measured size distribution, $Pb(NO_3)_2$.

5.3.5 *SEM results*

Figure 33 shows a SEM image of matter deposited on an aluminum substrate inserted in the centerline of the flame for about 1s in order to collect enough mass for the analysis. It is possible to observe a background containing a great number of ultrafine particles whose smallest fraction is not clearly focused because of instrumental resolution. The picture also shows the presence of biggest shapeless agglomerates, probably due to the long residence time of the substrate into the flame permitting particles growth. We sometimes found micrometer sized crystals, such as in the shown image. They could be evaporation residual of some larger coalesced droplets that sporadically could enter in the reactor. EDXS reveal, as expected, the presence of a great amount of lead but it is not able to give information about the degree of oxidation of collected particles because of the low resolution in detecting oxygen of the employed instrumentation.

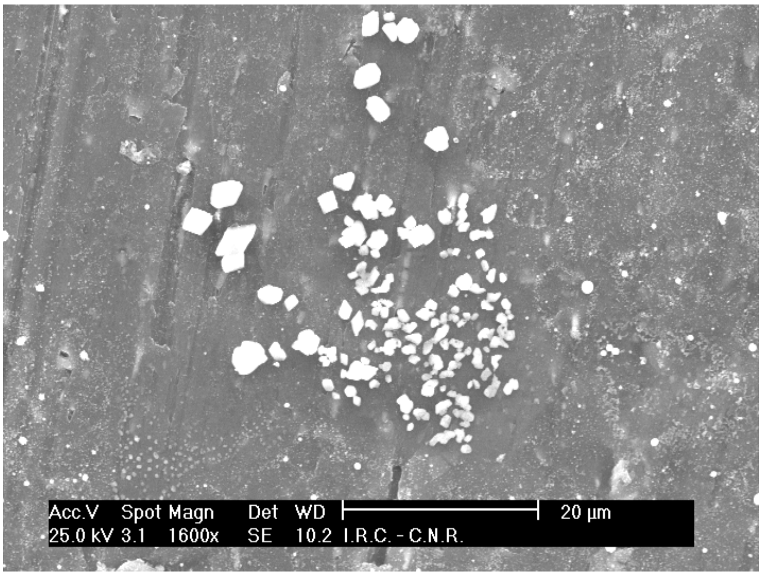

Figure 33 - SEM image of particles collected on aluminum substrate, $Pb(NO_3)_2$.

5.4 Cadmium Nitrate results

Assuming cadmium oxide (CdO) particles are generated from the $Cd(NO_3)_2$ solution, the material balance allow to calculate fv_{Ex}=1.2ppm. It was calculated also fv_{Ex}=0.84ppm for pure cadmium particles.

5.4.1 AFM results

AFM images, quite similar to that obtained using $Pb(NO_3)_2$ solution, of the samples collected upstream HAB=20mm again contains large objects, probably not fully evaporated droplets, as shown in Figure 34. The droplet presence prevents an accurate particles size analysis but it is clear that about 4nm particles emerge from its surface. For this reason it was again speculated that nanoparticles nucleate inside the droplets close to its surface because of fast not-uniform heating. The water left when solution saturation is reached, is in a lower amount respect to $Pb(NO_3)_2$ solution because of $Cd(NO_3)_2$ higher solubility. Thus the time available for nuclei aggregation, growth or diffusion inside the droplet is shorter

($Cd(NO_3)_2$-$4H_2O$ dehydrates at 484K) and generated particles are quite smaller. The complete $Cd(NO_3)_2$ decomposition to CdO (674K) is also fast because of very small sizes (Wojciechowski and Malecky, 1999). Thus the nuclei almost instantaneously shrink after to be released. CdO evaporation can also occur but its further thermal decomposition is not allowed at ~1200K.

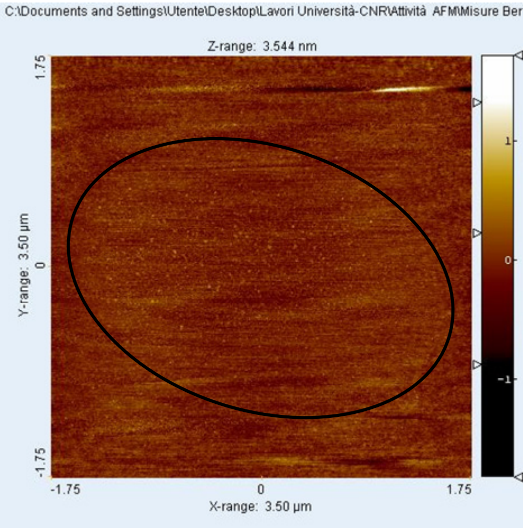

Figure 34 – AFM image of matter sampled at HAB=18mm, $Cd(NO_3)_2$.

AFM images processing of sample collected downstream HAB=20mm recognizes from 200 to 500 particles/μm^2. Figure 35 shows one of these images and the size distributions of collected particles. Points are obtained by AFM and the dotted lines are their best fitting with the parameters reported in Table 8. At HAB=20mm, particles are almost monodisperse with 2.2nm mean diameter (MED) and 0.6nm standard deviation (SD). Almost the same size distribution (2.1nm MED and 0.7nm SD) is obtained at HAB=25mm. The appearance of a second mode in the size distribution having 6.3nm MED and 2.2nm SD, is observed at HAB=30mm. The particles into the second mode represent just 0.5% of total number while the first mode still have 2.3nm MED and 0.8nm SD. At HAB=35mm the first mode slightly grows (3.1nm MED and 1.1nm SD). The relative number of particles into the second mode (1%) doubles with respect to the previous height. MD (12.7nm) and SD (4.4nm) double too.

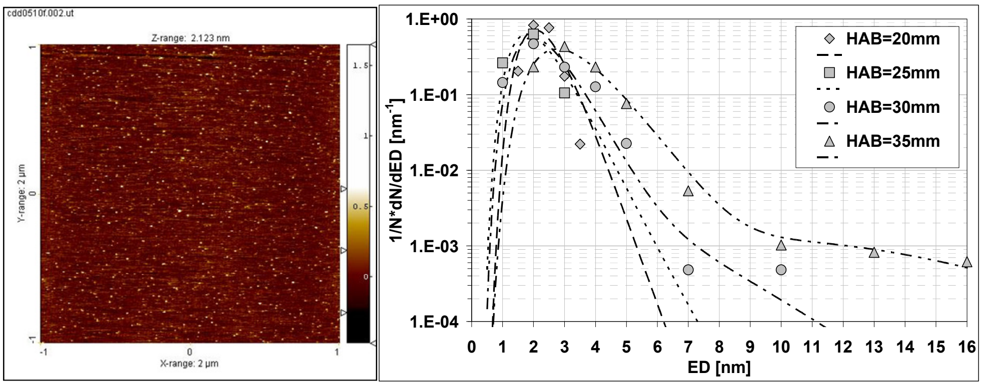

Figure 35 - AFM image of the sample at HAB=25mm (left side) and obtained size distributions, $Cd(NO_3)_2$ (right side, points AFM image analysis, dashed lines best fitting).

Table 8 – **Size distributions fitting parameters, $Cd(NO_3)_2$.**

HAB [mm]	w_I	$<ED_I>$ [nm]	$<ED_{II}>$ [nm]	σ_I	σ_{II}
20	1	2.2	-	1.3	-
25	1	2	-	1.3	-
30	0.995	2.2	6	1.4	1.4
35	0.99	3.1	12	1.4	1.4

The evidence that particles smaller than 5nm persist until HAB=25mm and they slightly grow further downstream implies a coagulation rate much slower than their thermal collision rate. Indeed, the half-life of ~2nm particles, whose N is evaluated to be ~$1.5*10^{14}$cm^{-3}, has to be ~10µs if each collision involves coagulation while it is about two orders of magnitude longer (~10ms). Thus coagulation efficiency of CdO 2nm monodisperse particles is about 10^{-3}. On the other hand, coagulation becomes effective for larger particles that quickly grow after their appearance. This behavior is explained assuming a size dependent coagulation efficiency quickly decreasing for sizes smaller than 6nm.

Particles ARs, plotted in Figure 36, are correlated with ED. Particles belonging to the first mode of size distributions have AR lower than 0.03. The second mode particle AR are also lower than 0.03 at HAB=30mm while they range from 0.03 to 0.1 at HAB=35mm. The observed low values could indicate a liquid-like behavior of nanoparticles. Indeed, their base shows an almost circular shape suggesting they could be spherical into the flame but they deform impinging on the substrate.

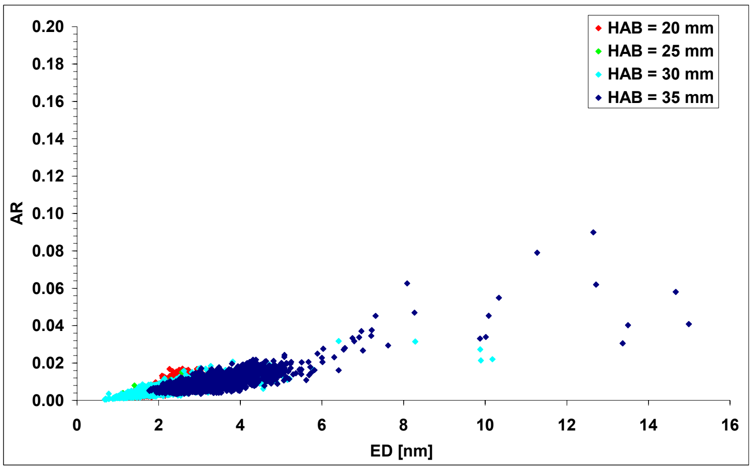

Figure 36 – Particles aspect ratios, $Cd(NO_3)_2$.

The fv_{AFM} to CdO fv_{Ex} ratio, representing the mean value of collection/adhesion efficiency, versus HAB is shown in Figure 37. If we measure only particles smaller than 6nm, upstream HAB=25mm, the thermophoretically collected matter volume is ~0.15% of the CdO expected value. It increases of one order of magnitude, despite possible CdO evaporation, simultaneously the appearance, at HAB=30mm, of larger particles. The fv_{AFM} value is higher (~1.4% of fv_{Ex}) at HAB=35mm where the size and the number of particles larger than 5nm further grow. Then it results clear that adhesion efficiency suddenly decrease for diameter below 5nm and it is about three orders of magnitude lower than unity for monodisperse particles collected at HAB=35mm. It is also surprising that at HAB=35mm the adhesion efficiency assume a value comparable to that obtained using the $Pb(NO_3)_2$ solution. This could be due to a stronger dependence on particles size than on chemical nature. Indeed, the particles obtained from the two nitrates at HAB=35mm have a similar shape of the size distributions.

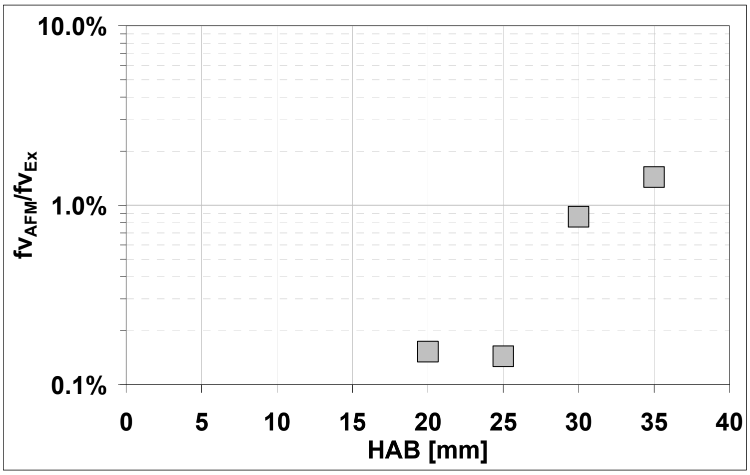

Figure 37 – Mean particles adhesion efficiency versus HAB, $Cd(NO_3)_2$.

5.4.2 LLS results

The LLS measured particles ED63 is plotted as a function of HAB in Figure 38. It does not grow appreciably with increasing RT because 2nm particles coagulation efficiency is three orders of magnitude lower than unity. The resulting profiles agree qualitatively with that obtained by AFM size distribution while, upstream HAB=25mm, the agreement is also quantitative. Further downstream LLS increasingly underestimates ED63 respect to AFM. It is interesting to note that the sizes in-situ measured by LLS excellently agree with those obtained considering only the first mode of AFM size distributions (ED63M1) that is almost completely composed of particles with ED lower than 5nm. The reason of this discrepancy could be a size dependent adhesion/collection efficiency which quickly decreases for particles smaller than 5nm. In this case the number concentration of smallest particles into the flame is much higher than that measured by the particles collected on the substrate causing AFM to overestimate the real ED63. Thus the first mode particles are almost the total of particle in the flame.

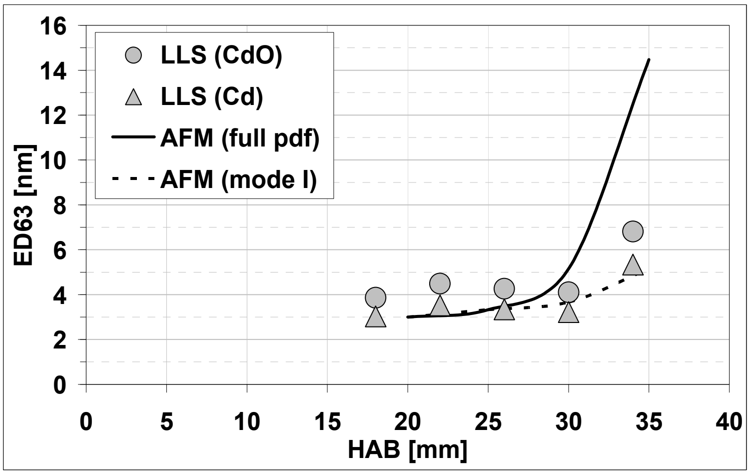

Figure 38 – LLS and AFM measured mean particles diameter versus HAB, $Cd(NO_3)_2$.

5.4.3 SEM results

Particle were collected for SEM imaging on an aluminum substrate, inserted in the centerline of the flame for about 1s in order to collect enough mass for the elemental analysis. The wide window images are quite similar to that obtained using the $Pb(NO_3)_2$ solution. They contain a great number of ultrafine particles some biggest shapeless agglomerates, probably due to the long residence time of the substrate into the flame permitting particles growth. Also in this case some micron sized crystalline particles and not fully evaporated droplets were sporadically found. A magnification of one of the agglomerate is shown in Figure 39 where ultrafine particles are also distinguishable in the background. EDS reveal, as expected, the presence of a great amount of cadmium but it is not able to give information about the degree of oxidation of collected particles because of the low resolution in detecting oxygen of the employed instrumentation.

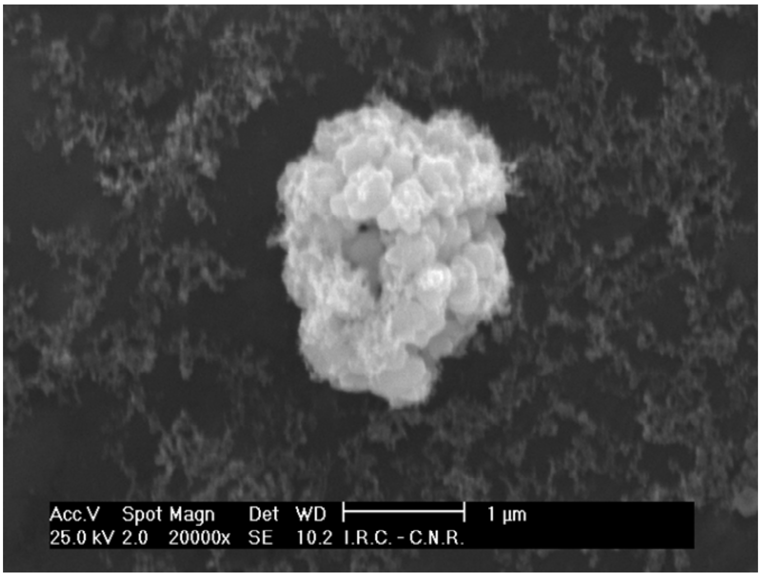

Figure 39 - SEM image of particles collected on aluminum substrate, $Cd(NO_3)_2$**.**

5.5 Nickel (II) Nitrate results

From $Ni(NO_3)_2$ solution, it is expected fv_{Ex}=1ppm of nickel(II) oxide (NiO) particles or fv_{Ex}=0.56ppm of nickel particles by performing the material balance.

5.5.1 AFM results

The speculation that $Ni(NO_3)_2$ nanoparticles nucleate into the droplets similar to $Pb(NO_3)_2$ is again assumed despite it was not possible to obtain similar image of nanoparticles emerging from larger object upstream HAB=20mm using this nitrate solution. This speculation is justified because of $Ni(NO_3)_2$ and $Cd(NO_3)_2$ comparable high value of the solubility in water and of nickel and NiO unvolatility at 1200K.

The AFM particles size distributions and their best fitting, whose parameters are reported in Table 9, are shown in Figure 40. The time evolution of the size distribution shows a similar shrinking trend of $Pb(NO_3)_2$ and an opposite behavior respect to $Cd(NO_3)_2$ since a bimodality is observed from the beginning while particles are monodisperse at longer residence times.

At HAB=20mm the size distribution is characterized by 3.4nm MED and 0.9nm SD for the first mode and by 12nm MED and 5nm SD for the second mode, the latter representing 4% of particles number. At HAB=25mm first mode MED (3.1nm) and SD (0.8nm) are slightly smaller while the second mode (4% of particles number) shrinks significantly (9.7nm MD and 4.1nm SD). At HAB=30mm the first mode still have 3.3nm MED and 0.8nm SD while the second mode, subjected to a further shrink (5.6nm MD and 1.4nm SD), is collapsing into the first mode. The latter completely disappears at HAB=35mm where almost monodisperse particles (4.2nm MD and 1nm SD) are sampled.

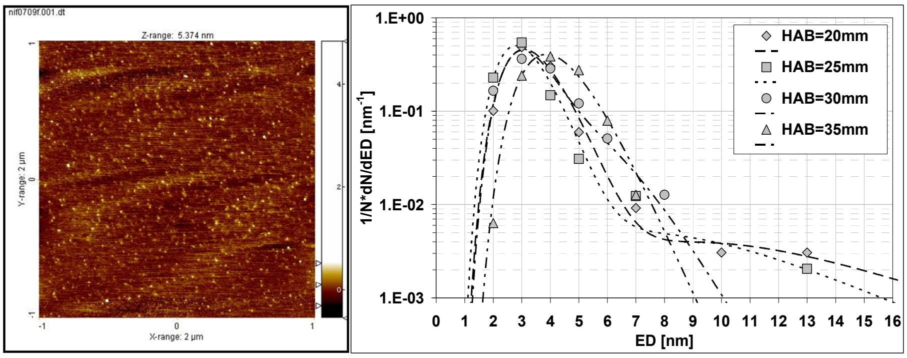

Figure 40 - AFM image of the sample at HAB=25mm (left side) and obtained size distributions, $Ni(NO_3)_2$ (right side, points AFM image analysis, dashed lines best fitting).

Table 9 – **Size distributions fitting parameters, $Ni(NO_3)_2$.**

HAB [mm]	w_I	$\langle ED_I \rangle$ [nm]	$\langle ED_{II} \rangle$ [nm]	σ_I	σ_{II}
20	0.96	3.3	11	1.3	1.5
25	0.96	3	9	1.3	1.5
30	0.85	3.2	5.4	1.28	1.28
35	1	4.1	-	1.28	-

The particle AR, plotted in Figure 41, is again correlated with ED. For particles in the first mode it attains value lower than 0.05 but downstream at HAB=25mm it never exceeds 0.03. The second mode particles show different features having AR ranging from 0.05 to

0.3. Collected particles bases show an almost circular shape as for the $Pb(NO_3)_2$ and the $Cd(NO_3)_2$ cases, again indicating they could be spherical into the flame but deform impinging on the substrate.

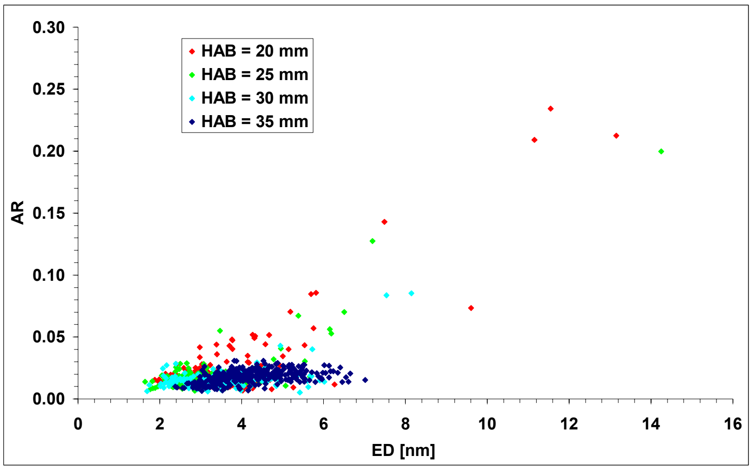

Figure 41 – Particles aspect ratios¸ $Ni(NO_3)_2$.

The incipient bimodal nature of the size distribution probably depends on the $Ni(NO_3)_2$-$6H_2O$ thermal decomposition (Brockner et al., 2007). Its dehydration is achieved at a slightly lower temperature (418K-463K) with respect to $Cd(NO_3)_2$, thus the $Ni(NO_3)_2$ nucleate faster. Therefore, nuclei are able to slightly grow and some of them aggregate forming larger particles before emerging from the droplets. Nevertheless the particles are smaller respect that obtained from the quite less soluble $Pb(NO_3)_2$.

The first mode particles, slightly larger than that generated from $Cd(NO_3)_2$ solution but very smaller than generated from $Pb(NO_3)_2$ solution, are quickly heated and decomposed into NiO (573K). The shrinking of the second mode observed downstream in the flame is compatible with the particles loss of mass involved in $Ni(NO_3)_2$ to NiO decomposition.

The larger particles slower decomposition may be due to their lower specific surface area slowing nitrides release. The NiO evaporation or further thermal decomposition is not allowed at ~1200K.

Also for the $Ni(NO_3)_2$ case the detected ~3nm particles show a ~10ms half-life, much longer than the value of ~35µs calculated assuming each collision, due to particles thermal motion, involve coagulation and evaluating $N\sim4.5*10^{13}cm^{-3}$. Once again the longer lifetime of nanoparticles can be explained assuming a low value of coagulation efficiency decreasing for size lower than 5 nm and assuming a value between 10^{-3} and 10^{-2} for generated NiO 3nm particles. This value is just slightly larger than that observed for the ~2nm CdO nanoparticles.

The fv_{AFM} to NiO fv_{Ex} ratio, representing the mean value of collection/adhesion efficiency, versus HAB is shown in Figure 42. The fv_{AFM} decrease (Fig.4b), from ~1.8% to ~0.6% of fv_{Ex}, simultaneously disappearing of larger particles downstream into the flame. These values are slightly higher than that obtained for particles, having slightly smaller sizes, generated employing the $Cd(NO_3)_2$ solution and smaller than that obtained for larger particles generated from the $Pb(NO_3)_2$ solution. Nevertheless the value obtained at HAB=20mm is comparable with both values measured at HAB=35mm using the other two nitrate solutions because of quite similar size distribution shapes. Thus both adhesion and coagulation efficiency seem to depend stronger on size than on nanoparticles composition, supporting the idea that they have the same physical nature (D'Alessio et al., 2005).

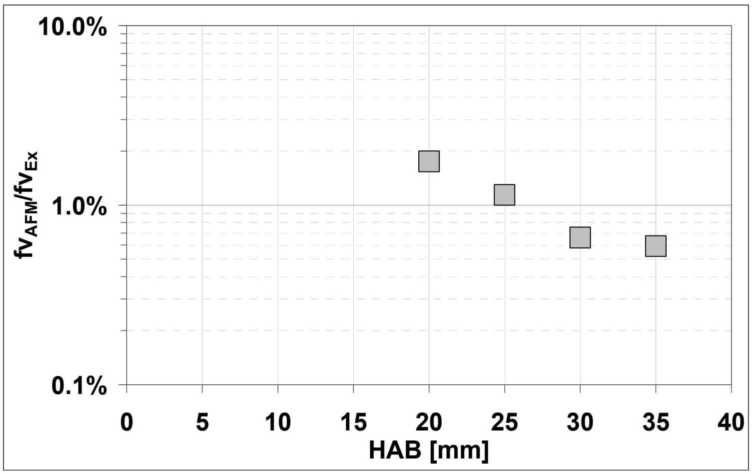

Figure 42 – Mean particles adhesion efficiency versus HAB, $Ni(NO_3)_2$.

5.5.2 LLS results

The Figure 43 shows the LLS in situ measures ED63. It does not grow appreciably with increasing RD because of the observed very low value of 3nm particles coagulation efficiency. Moreover until particles larger than 5nm are detected, upstream of HAB=25mm, AFM overestimates the LLS ED63. Downstream of HAB=25mm a qualitative agreement is obtained, becoming quantitative further downstream. The qualitative disagreement upstream of HAB=25mm probably depends on particles properties changing, in terms of refractive index, also indicated by AR lowering and larger particles shrinking. The quantitative discrepancy can be again explained by the AFM observed size dependent sticking efficiency quickly decreasing for size lower than 5nm. Indeed the LLS ED63 quantitatively agrees with that obtained considering only the first mode of the size distribution composed almost totally by particles smaller than 5nm. The low adhesion efficiency of smaller particles causes, as for the $Cd(NO_3)_2$ and the $Pb(NO_3)_2$ cases, that their relative number is much higher in-situ than on the analyzed substrates (D'Alessio et al., 2005). Particles in the flame are almost totally with size lower than 5nm.

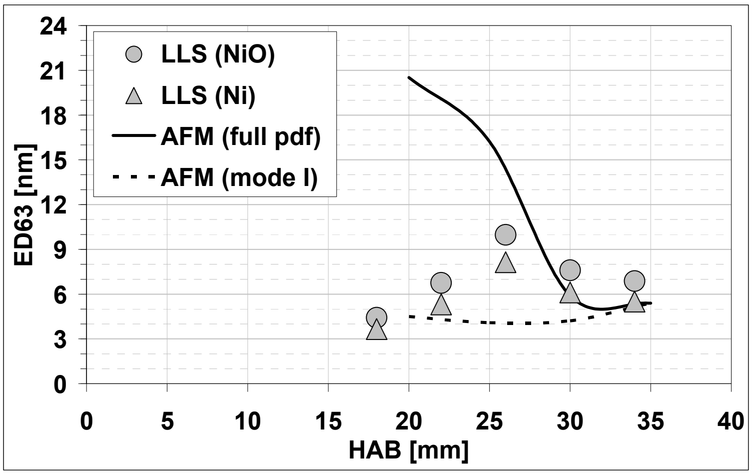

Figure 43 – LLS and AFM measured mean particles diameter versus HAB, $Ni(NO_3)_2$.

5.5.3 SEM results

Particles were collected for SEM imaging on an aluminum substrate, inserted in the centerline of the flame. The sampling time was 1s in order to collect enough mass for the elemental analysis. The wide window images are quite similar to that obtained using the $Pb(NO_3)_2$ and $Cd(NO_3)_2$ solution. They contain a great number of ultrafine particles some biggest shapeless agglomerates, probably due to the long residence time of the substrate into the flame permitting particles growth. Also in this case we sporadically found some micron sized droplet residual.

The samplings were also performed reducing the sampling time to ~30ms to prevent particles aggregation on the substrate. In this case one hundred substrate insertions in flame are required to collect enough matter. An image obtained using this sampling procedure is shown in Figure 44. In the center of this image there is a residual not fully evaporated droplet that seem to dry when the electron beam was focused on it, but the remaining part of the substrate is covered by a layer of ultrafine particles whose size are well below the instrumental resolution. EDS reveal, as expected, the presence of a great amount of nickel but again it is not able to give information about the sampled particles oxidation degree.

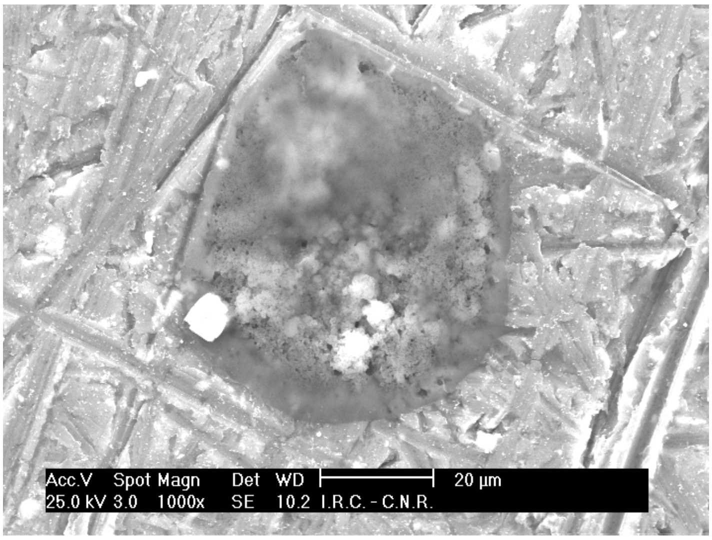

Figure 44 - SEM image of particles collected on aluminum substrate, $Ni(NO_3)_2$.

5.6 Results comparative discussion

The size distributions, in a size range extending below 10nm, of nanoparticles generated by heating lead (II), cadmium and nickel (II) nitrate aqueous solution droplets in a flame, were measured with the AFM technique.

In this chapter it was supposed that nanoparticles nucleate inside the droplets during their fast not-uniform heating. Their size seems correlated with nitrate solubility in water and thermal behavior. Almost monodisperse ~2nm CdO particles were generated using the highest soluble and faster dehydrating $Cd(NO_3)_2$. The bimodal nature and slight larger ED of nanoparticles produced from $Ni(NO_3)_2$, having similar high solubility, depends on its lower dehydrating temperature respect to $Cd(NO_3)_2$ involving faster nitrate nucleation. Therefore, nuclei were able to slightly grow and some of them to coagulate before emerging from the droplets. The smallest ones were almost instantaneously heated and decomposed to NiO ~3nm particles while larger ones decomposition required longer time because of lower specific surface area slowing nitrides release. Bigger first mode particles and higher frequency of second mode were obtained from the less soluble $Pb(NO_3)_2$ because of its faster nucleation into the droplets. This particles shrink because of $Pb(NO_3)_2$ to PbO decomposition. This decomposition is slower respect to that of $Ni(NO_3)_2$ because larger particles were produced.

Despite the different shapes of size distributions, depending on the used solution, particles smaller than 5nm were generated in each investigated case, showing a coagulation rate much slower than their Brownian collision rate. Using the $Pb(NO_3)_2$ solution, this behavior is not very evident from AFM analysis but is observed with by both LLS and preliminary DMA measurements. It depends on the dramatic decrease of coagulation efficiency for ED below 5nm.

AFM also indicate a similar sudden decrease of adhesion/collection efficiency on substrate for ED smaller than 5nm. The in-situ LLS size measurements, compared to AFM ones, confirmed that both particles coagulation and adhesion efficiency on the substrates decrease by orders of magnitude with decreasing diameters below 5nm. The similar decreasing trend both the efficiencies could indicate they have the same physical nature. They strongly depend on particles size while it seems to be less influenced by particles chemical nature. Indeed, from a preliminary analysis, coagulation and adhesion efficiencies values quantitatively agree for all the investigate cases and with those reported in literature for carbonaceous nanoparticles (D'Alessio et al., 2005).

It seems that particles with size between 1nm and 5nm, hardly collectable and having a not-negligible lifetime, are generated anytime the process is enough fast. These results imply that smallest metal nanoparticles produced by combustion devices may be easily dispersed into the atmosphere because they have a much longer life-time than generally assumed and may easily bounce on surfaces or filters. These features imply a not-trivial pollution problem because, having a low volume, they are released and persist in atmosphere in high number concentration even if they represent a small mass percentage of particulate matter.

The SEM results had shown that the injection of metal salts solution in premixed flame may be a promising method to deposits nanopowder or nanocatalyst with primary particles size of few nanometer in size. Problems of the used reactor, regarding the sporadic injection of larger coalesced and not quickly evaporating droplets, had to be solved to this aim.

Chapter 6

Nickel (II) nitrate homogeneously doped premixed flame

Some of the results reported in this chapter were presented at the 2nd Advanced Atmospheric Aerosol Symposium AAAS 2008, 9-12 Novembre 2008, Napoli and were published on Chemical Engineering Transaction 16, 87(Carbone et al, 2008b): Carbone, F., Barone, A., De Filippo, A., Beretta, F. , D'Anna, A. and D'Alessio, A., *Coagulation and Adhesion of Nanoparticles generated in flame from droplets of Nickel Nitrate aqueous solutions*.

6.1 Operating conditions

The investigated reactor is a fuel lean laminar premixed flame (cold gas velocity 300mm/s) of methane/oxygen/nitrogen in the ratios 1/2.6/8, homogeneously doped with metal precursor droplets. The flame was stabilized on a properly designed burner similar to that used by Arabi-Katbi et al. (2002). The burner consist of a 40mm long Mullite Zirconia honeycomb (400CPSI, CTI s.a.) placed on the top of a 18mm ID stainless-steel tube. The honeycomb both stabilizes the flame and it allows the homogeneous addition of the particles precursor droplets. Another stainless steel tube, coaxial to the burner, provides an outside ring (ID 24 mm and OD 32 mm) used for flowing the sheath N_2 (flow rate of 3400 cm^3/min) to minimize the entrainment of the surrounding air. $Ni(NO_3)_2$ aqueous solution, with mass concentration of 4%, droplets of 25μm were dispersed and diluted the into the cold gas mixture. The 0.089 cm^3/min of monodisperse solution droplets are generated by a Berglund-Liu-type Vibrating Orifice Aerosol Generator (model 3450, TSI) using a 10μm orifice oscillating at a frequency of 120KHz. The obtained homogeneously doped premixed flame, showed in Figure 46, may be assumed as a plug flow reactor. Nickel was preferred to other pollutant metals because its oxides, generated by $Ni(NO_3)_2$ thermal decomposition (Brockner et al., 2007), are not volatile at flames temperature (Linak and Wendt, 1993). Therefore the absence of vapor phase avoids particles surface growth and simplifies results interpretation because nanoparticles, once generated, are only able to coagulate.

Figure 45 – A picture of the homogeneously doped flame.

The temperature profile along the flames axis was measured using a 125µm Pt/Pt-13%Rh thermocouple (Type R, Omega Engineering) and substituting the solution with bi-distilled water to prevent nanoparticles deposition on the measurement junction. Measured temperature was corrected for radiative lost. The temperature increases up to ~2050K from the burner surface to just downstream the flame front, then it slowly decreases reaching ~1600K at HAB=50mm. Droplets fully evaporated during less than 2.5ms, upstream HAB=5mm where incipient nanoparticles were early measured. The temperature profile versus HAB is plotted in Figure 46 while Table 10 report RT at several HAB.

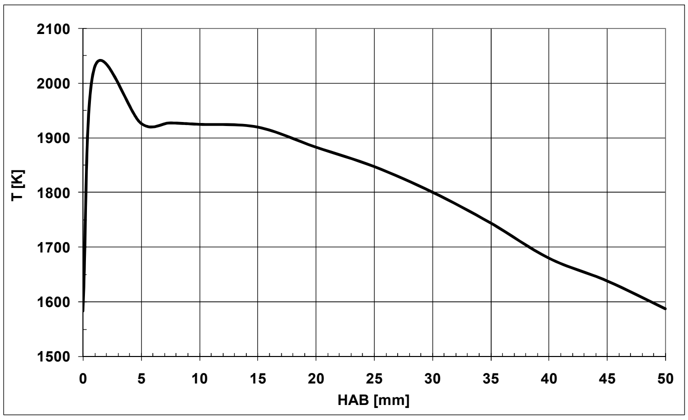

Figure 46 – Axial temperature profile.

Table 10 – **Particles residence time in flame.**

HAB [mm]	5	7.5	10	15	20	25	35	50
RT [ms]	2.5	3.8	5.1	7.7	10.3	13	18.5	27.4

6.2 Performed analysis

Mobility Diameter (MD) distributions of nanoparticles produced with the honeycomb burner are on-line measured using a dilution probe and a TapCon 3/150 DMA system (nominal MD range 0.6–28 nm) equipped with a Faraday Cup Electrometer detector (Sgro et al., 2007). MD is slightly larger than ED in the size range smaller than 3nm because of an effective diameter (D_0= 0.5 nm for air) of particles-free gas sheath in the electrostatic classifier (Fernandez de la Mora, 2003) implying ED=MD- D_0. Results were also converted in ED distributions using this relation. Following published works, we used a horizontal tube rapid dilution probe (8mm ID, 0.5mm wall thickness, 0.3 mm orifice diameter) to transport and cool sampled aerosol (Kasper et al., 1997; Sgro et al. 2007). Earlier work examining dilution probes found that particle coagulation in the probe may significantly change the shape of the size distribution (Kasper et al. 1997, Zhao et al., 2003). Experimentally, particle coagulation is suppressed by varying the dilution ratio (DR) in order to attain a critical value. Above this value the size distribution does not change and the eventual changing of particles number is inverse proportional to the dilution itself. The dilution ratio was controlled by monitoring a slight underpressure in the probe, manually controlled with a rotary vane vacuum pump, while holding the particle free dilution N_2 flow constant at 29.6lpm. The sample flow rate was calibrated (Sgro et al., 2007) by measuring CO_2 concentrations with a non-dispersive infrared analyzer (Hartmann & Braun URAS 10E) drawn in from flames with the probe operating exactly as it was during particle size distribution measurements (Zhao et al., 2003). The number concentration and the volume fraction of particles in selected size ranges are calculated by integrating the measured size distribution.

Particles are thermophoretically collected on mica muscovite disks (3mm diameter) inserted parallel to the gas streamline using a properly designed pneumatic actuator that assures a quick insertion and a constant sampling time ($\Delta t \sim 30$ms). Samplings are performed at several HAB to perform AFM images analysis as described in Chapter 4. AFM results are converted in ED normalized frequency distribution subsequently fitted by a weighted sum of lognormal distributions allowing its easy handling. Unormalized AFM size distributions are obtained using the particle number concentration (N_{AFM}) obtained from the total number of collected particles:

We perform the same data analysis described in chapter 5. Furthermore we are able to obtain the adhesion efficiency profile versus ED by simply performing the ratio between AFM and DMA size distribution.

$$\gamma_{adh}(ED) = \frac{\left(dN/dED \right)_{AFM}}{\left(dN/dED \right)_{DMA}} \tag{6.1}$$

Particles are also collected on an aluminum substrate rapidly inserted on the flame axis at HAB=30mm. This sample is then examined by a Philips XL30 SEM with a LaB6 filament equipped with an EDS DX-4i microanalysis device.

6.3 DMA Results

The DMA analyzes sampled aerosol in a nominal size range between 0.6nm and 28nm. The first task is to understand how many of the acquired signal can be associated to particles. Background measurements were performed to this aim on pure nitrogen and on gases sampled at HAB=15mm of the flame doped with water despite solution droplets. The resulting size distributions are shown in Figure 47 together with that measured in nickel nitrate doped flame using the same DR used for water doped flame, both not corrected for the DR.

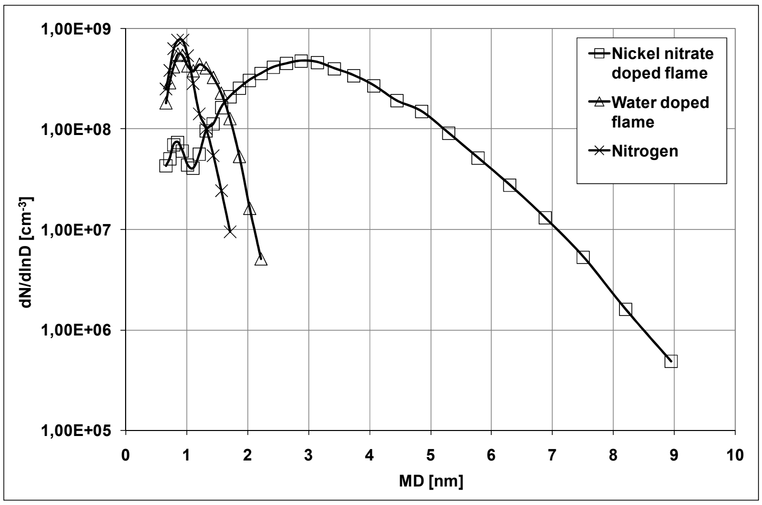

Figure 47 – DMA measured and background size distributions.

The measured size distribution always show a sub-nanometer peak whose intensity decreases with the increase of larger particles number concentration. This peak is probably due to formation of molecular clusters during ionization process that transfer their charge to particles, if present (Sgro et al., 2007).

The number concentration of nitrogen clusters is negligible respect to doped flame products for MD lower than 1.2nm while the cluster generated from water doped flame are slightly larger being negligible for MD lower than 1.6nm. For this reason it was considered that only the branch of size distributions with MD larger than 1.6nm, i.e. ED larger than 1.1nm, represents particles. The not considered sub-nanometer peak gives a negligible contribution to fv calculation while it always contains the largest number of object.

6.3.1 Optimal sampling dilution

The DMA analyzes sampled and diluted aerosol downstream of a sampling line of 1.1m in length. Coagulation, condensation and loss of diffusive nature can occur in this probe before products reach the DMA, mainly during the dilution downstream the pinhole, altering qualitatively or quantitatively the size distribution of particles sampled in flame. The coagulation generally results in the particles size growth and number concentration reduction without changing their volume fraction. The condensation, not active in this experiment, results in both particles sizes and volume fraction increase without changing their number concentration. The diffusive losses are mainly localized in the pinhole and they depends on probed aerosol flow-rate in the pinhole itself and then on the DR reciprocal.

Measurements were performed by varying dilution ratio and to determine an optimum value of the dilution ratio that minimize the sampling effects on the results. A too high dilution corresponds to low sampled aerosol and significant losses while low dilution involves aerosol coagulation in the probe. Some representative size distribution measured at HAB=5mm and corrected for the several used Dilution Ratios (DRs), are shown in Figure 48. It is clear in this plot that the size distribution moves towards smaller MD and contain a smaller number of particles by increasing DR

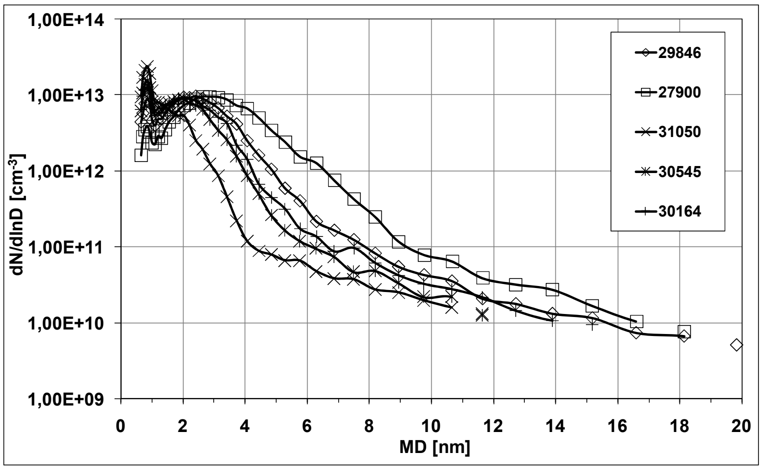

Figure 48 – DMA measured size distributions at HAB=5mm using several Dilution Ratios (◊ DR=29846; □ DR=27900; x DR=31050; ∗ DR=30545; + DR= 30164).

To better understand the probing effect we plot, in Figure 49 and Figure 50, the particles number concentration and volume fraction versus the sampling DR, respectively. Both the value are calculated for the entire size distribution, the subnanometric peak (MD<1.6nm), the particles size distribution (MD>1.6nm), and the eventual second mode particles (MD>10nm).

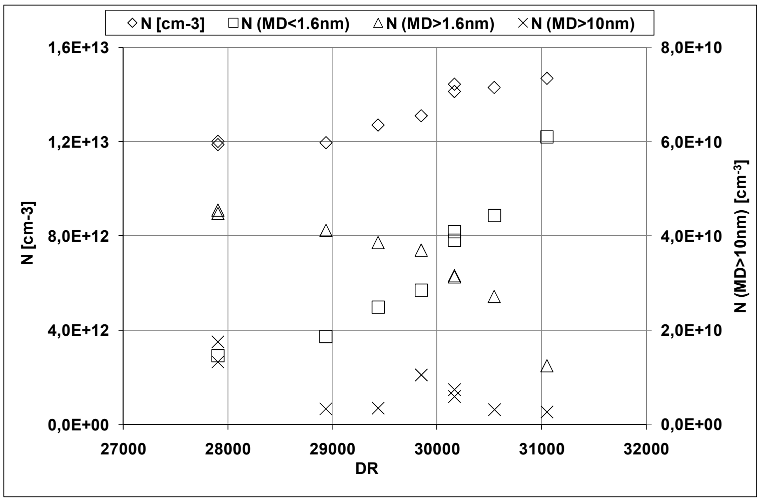

Figure 49 – Particles number concentration measured at HAB=5mm versus DR.

The total number is almost constant varying DR ad it just slightly grows with increasing DR because of dilution correction. Indeed, the total number of charges is constant and depends on the used ionizer. The particles (MD>1.6nm) number concentration slightly decreases and the volume fraction is almost constant up to DR=30000 then they both suddenly decreases because of diffusive lost for higher DR. Simultaneously the number concentration of subnanometric object, whose volume fraction is always negligible, increases for DR higher than 30000 because of particles losses. Observing the size distribution reported in Figure 48, it is clear that such losses are more effective for larger particles that firstly disappear with increasing DR. The slight increase of particles number concentration with decreasing DR below 30000 is probably associated with particles coagulation into the probe.

Indeed the second mode particles (MD>10nm) increase both in number and in volume with decreasing DR below 29000.

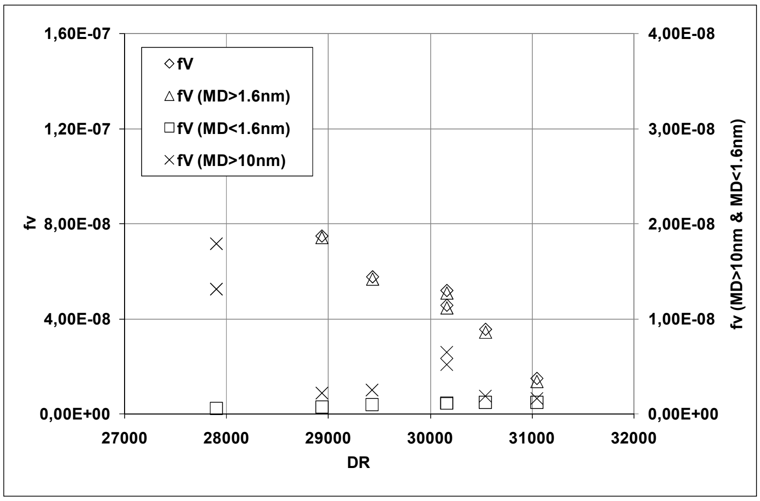

Figure 50 – Particles volume fraction measured at HAB=5mm versus DR.

The optimal dilution, to measure the particles size distribution in flame, obtained from these results is comprised between 29000 and 30000. The lower limit corresponds to the need of reducing coagulation and the higher to that of preventing the particles losses.

The same procedure is performed by changing the sampling HAB. The size distribution, particles number concentration and volume fraction measure at HAB=15mm are plotted, as another representative example, in Figure 51, Figure 52 and Figure 53, respectively. The trend and the corresponding interpretation of results are quite similar to that obtained at HAB=5mm despite particles larger than 10nm are never measured.

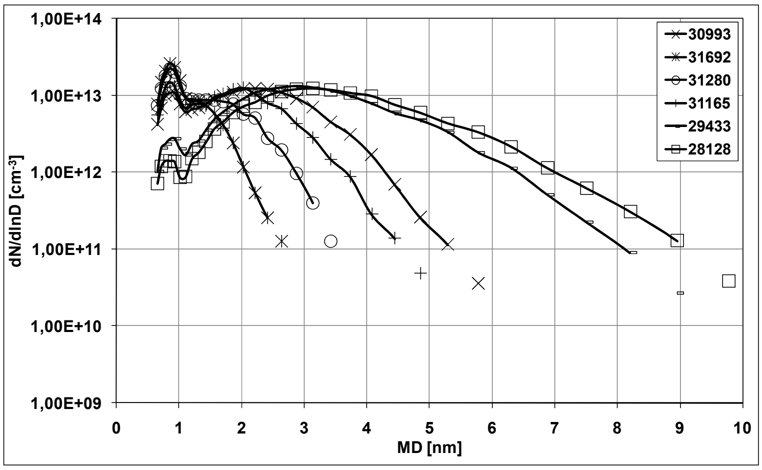

Figure 51 – DMA measured size distributions at HAB=15mm using several Dilution Ratios (x DR=30193; ∗ DR=31692; o DR=31280; + DR=31165; - DR=29433; □ DR=28128).

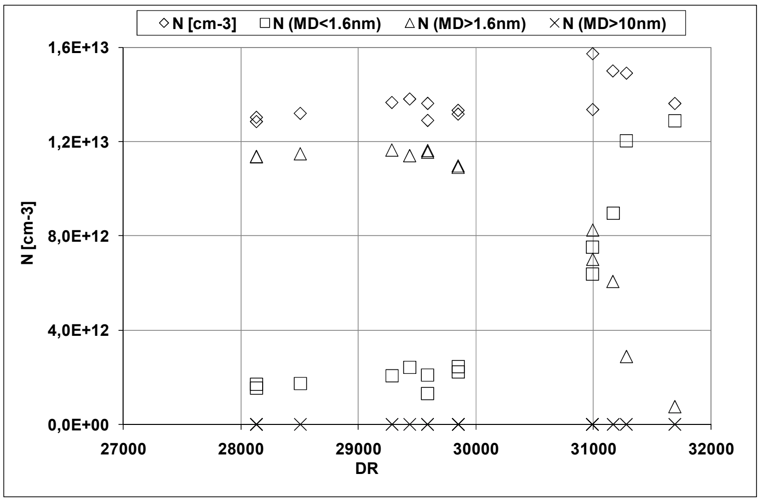

Figure 52 – Particles number concentration measured at HAB=15mm versus DR.

It is possible to conclude that the optimal DR to measure the particles size distribution in flame is between 29000 and 30000. These DRs optimal values are in good agreement with that used to measure carbonaceous nanoparticles produced by slightly sooting flames (Sgro et. al., 2007). They allow to follow faithfully the size distribution of the smaller nanoparticles, in the size range between 1nm and 5nm, but they reduce the number concentration in the probe of larger particles (MD > 10 nm) to be right at the limit of the dynamic range of the electrometer, and thus their measurement to be very noisy.

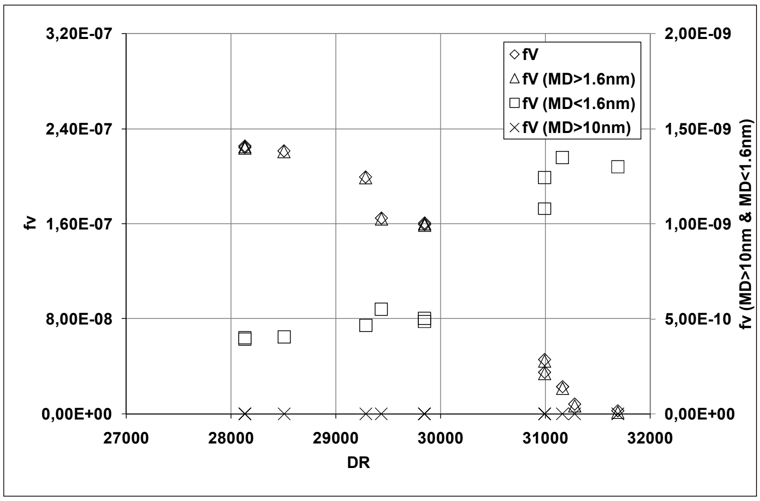

Figure 53 – Particles volume fraction measured at HAB=15mm versus DR.

6.3.2 Size distribution functions at several HAB

On-line aerosol measurements were performed by DMA at several HAB using the optimal DR. Some representative measured distributions are reported in Figure 54. They always show a sub-nanometer peak detected also in particles free gasses and probably due to formation of molecular clusters during ionization process (Sgro et al., 2007). This sub-nanometer peak also gives a negligible contribution to fv calculation, thus is not considered to represent particles and it is not further discussed. The particles distributions show a behavior quite similar to that observed for the doped flame described in chapter 4. Indeed it is bimodal at HAB=5mm while particles are monodisperse at longer RD. At HAB=5mm (RD=0ms) first mode MED and SD are 2.8nm and 1.2nm, respectively while second mode, about 0.1% of total particles number, have 13nm MED and 3.2nm SD. Particles larger than 10nm quickly disappear after RD~1.4ms (at HAB=7.5mm) and almost the same monomodal distribution (2.7nm-2.9nm MED and 1nm-1.3nm SD) is measured up to HAB=50mm (RD~25ms). In fig.3a two distributions measured at HAB=15mm at the beginning (I) and at the end (II) of the experiment were also reported. They show a negligible loss of particles (1%), especially for larger ED, due to a slight clogging of probing pinhole after about 2 hours of measurements and they also indicate measurements uncertainty.

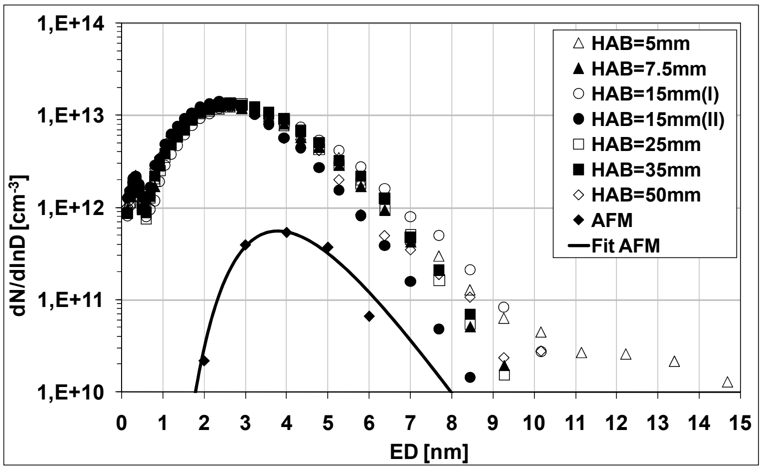

Figure 54 – DMA and AFM measured size distributions.

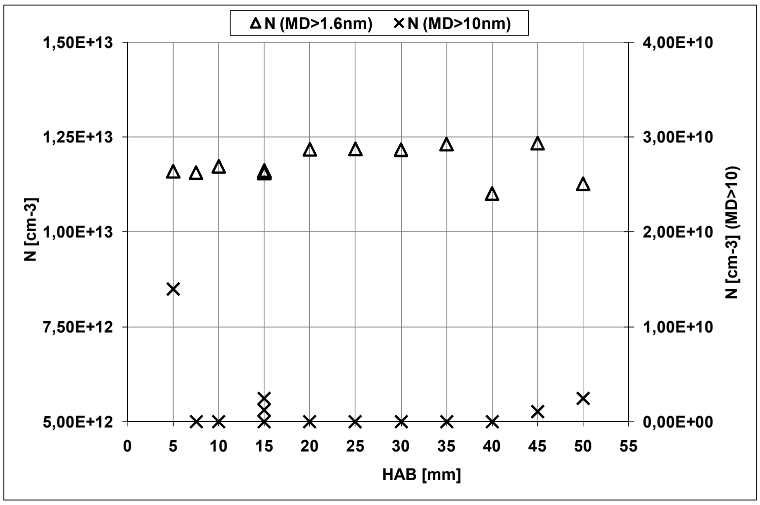

Figure 55 – DMA measured particles number concentration versus HAB.

Integrating the measured distributions, it was calculated an almost constant of fv~0.22ppm and N~$1.2*10^{13}cm^{-3}$ axial profiles, as shown in Figure 55 and Figure 56. Thus it is evident that, once generated, the ED~2.8nm particles do not coagulate in spite gas kinetic theory implies, at the measured N and T, a half-life of about 150μs for those Brownian particles (Hinds, 1999). The unchanging of distribution during the investigated RD~28ms, involves values of coagulation efficiency at least tree orders of magnitude lower than unity for ED~2.8nm.

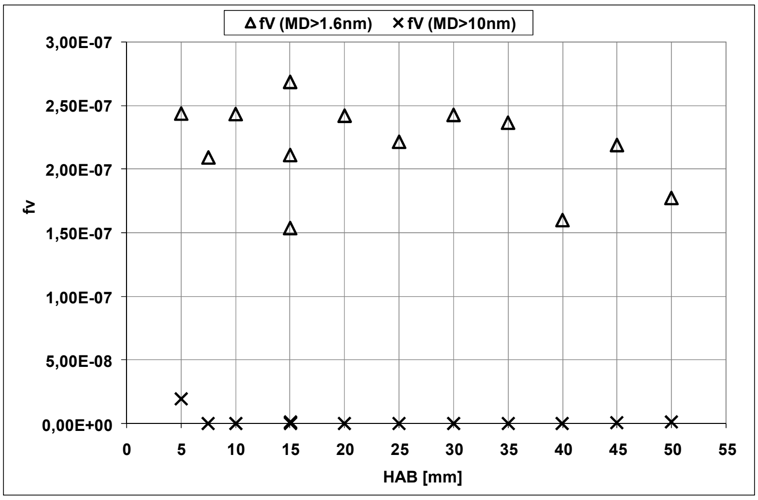

Figure 56 – DMA measured particles volume fraction versus HAB.

6.4 AFM results

We also collected 500-600particles/μm^2 on mica substrates at several HAB to perform their AFM image analysis. An AFM image of collected particle is shown in Figure 57. Roughly the same monomodal aerosol distribution was obtained at all HAB. That distribution obtained at HAB=15mm is also reported in Figure 54 together with DMA ones. It is representative of distribution at each HAB and it has MED=3.9nm and SD=1nm. Points represent ED absolute frequency and the line is the best fitting.

Almost constant value of N_{AFM}~3.5*10^{11}cm^{-3} and fv_{AFM}~10ppb were calculated. Then also AFM results show the not coagulating behavior of those nanoparticles with size lower than 5nm. Furthermore N_{AFM} and fv_{AFM} values are much lower than that on-line measured by DMA because the mean adhesion efficiency is about two orders of magnitude lower than unity.

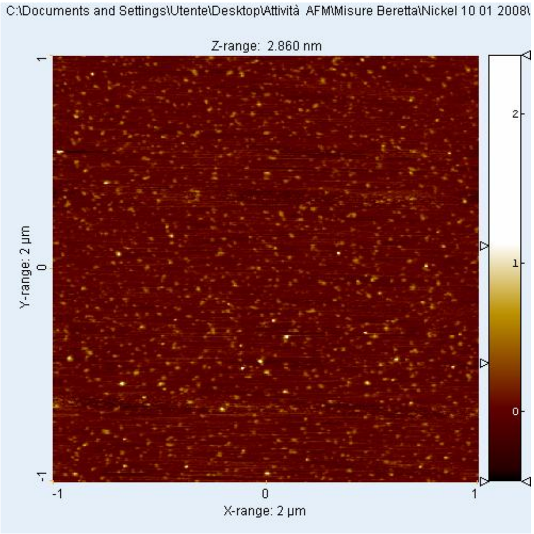

Figure 57 – AFM image of collected particles.

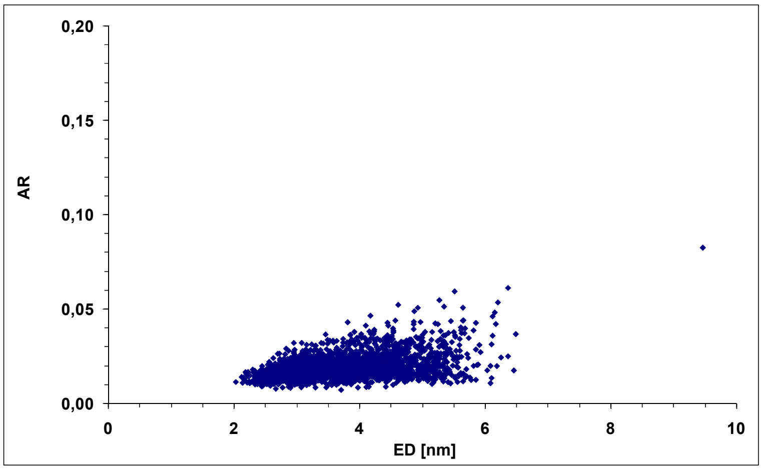

Figure 58 – Particles aspect ratios.

The particle AR, plotted in Figure 58, is again correlated with ED but it never exceeds 0.05. Collected particles bases show an almost circular shape as for the doped flame reactor, described in chapter 4, again indicating they could be spherical into the flame but deform impinging on the substrate because of a liquid like behavior.

6.4.1 Adhesion efficiency

Comparison of AFM with DMA distributions shows that the larger amounts of uncollected particles are those with lowest ED because of size dependent collection efficiency. The ED dependence of adhesion efficiency was obtained by the AFM to DMA distributions ratio and is showed in Figure 59. It quickly decreases for ED lower than 5nm reaching values about two orders of magnitude lower than unity for ED~2.5nm. This behavior, quite similar to that observed for carbonaceous nanoparticles (D'Alessio et al., 2005), conducts AFM to overestimate the real MED.

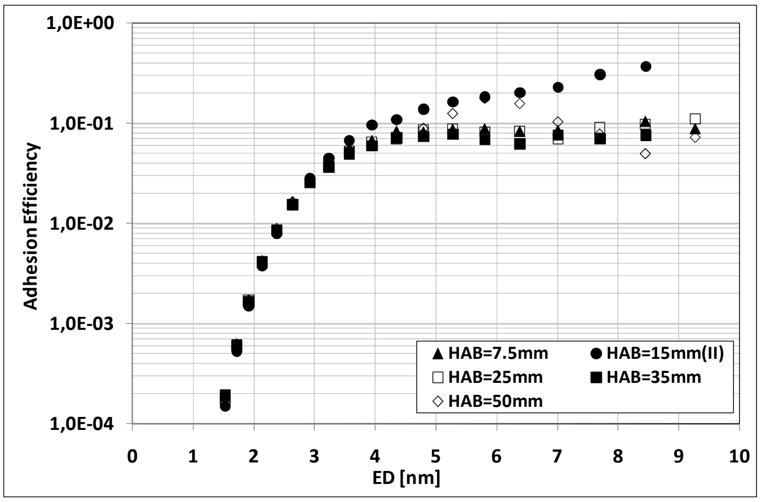

Figure 59 – Adhesion efficiency size dependence.

6.1 SEM results

Particles were collected for SEM imaging on an aluminum substrate, inserted in the centerline of the flame at HAB=30mm. The sampling time is ~30ms to prevent particles aggregation on the substrate but one hundred substrate insertion in flame are required to collect enough matter for elemental analysis. The obtained SEM images, one shown in Figure 60, contain a relative low number of submicronic particles. The amount of collected matter identifiable in the SEM images was not enough to perform a wide image elemental analysis. Surprisingly, the wide image elemental analysis recognizes a big amount of deposited nickel that is hidden in the images. It is probably contained in a thin powder layer whose primary particles have size much smaller than our SEM resolution.

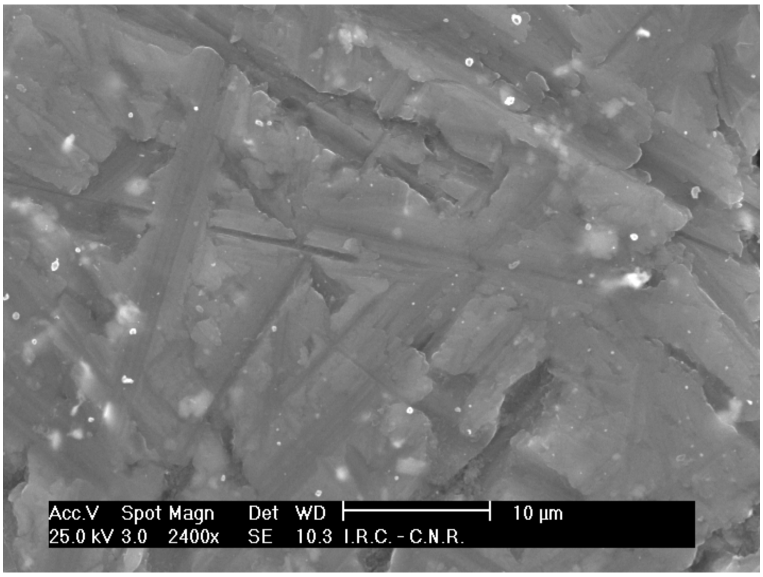

Figure 60 - SEM image of particles collected on aluminum substrate.

6.2 Results comparative discussion

Results obtained on the two different reactors described in this and in the previous chapter are quite similar in spite of different temperature values. The formation of such small nanoparticles seems to be related more on droplets heating rate than on temperature itself. A vapor phase nanoparticles formation pathway is to be excluded also because NiO and Ni are not volatile at the measured temperatures (Linak and Wendt, 1993). We speculate that nanoparticles nucleation occurs inside the droplets, as already proposed in literature (Limaye and Helble, 2002). The nuclei are released into the gas before their aggregation, growth or diffusion inside the droplet can occur because of evaporation quickness. The smallest nuclei are almost instantaneously heated and decomposed (573K) (Brockner et al., 2007) to NiO ~2.5nm particles while larger ones decomposition requires longer time because of their lower specific surface area slowing nitrides release. The nanoparticles loss of mass, involved during this decomposition, is compatible with the measured second mode shrinking observed in both experiment and it is faster for honeycomb burner because of its higher temperature. Furthermore particles larger than 10nm measured by DMA at HAB=5mm of the Honeycomb burner are not detected by AFM measurements. This may be an effect of flame cooling by DMA dilution probe slowing the nitrate decomposition.

Comparing DMA and AFM results we calculate the adhesion efficiency dependence on particles size. It decreases by orders of magnitude with decreasing diameters below 5nm. The obtained adhesion efficiency is quite similar to that observed by D'Alessio et al. (2005) for carbonaceous particles indicating that its decrease is most influenced by size effect than by particles chemical nature.

Deposition for SEM analysis showed that this experimental configuration may be suitable to perform deposition nanopowder or nanocatalyst with primary particles of few nanometers in size.

Chapter 7

Pulverized coal homogeneously doped premixed flame

7.1 Operating conditions

A pulverized coal suspension, in the form 80μm droplets and with 1.88% mass concentration in ethanol, was dispersed into 2.1l/min of oxygen. The 0.3cm^3/min of monodisperse droplets were generated by a Berglund-Liu-type Vibrating Orifice Aerosol Generator (model 3450, TSI) using a 40μm orifice oscillating at a frequency of 20KHz. The coal was milled in a Planetary Mono Mill (Pulverisette 6, Fritsch) and, successively, suspended in ethanol. The suspension was intensively sonicated to fragment agglomerated particles. A granulometric analysis (Hydro 2000S, Malvern Instrument) reveal that 95% of the coal have size lower the 30μm, allowing to use the VOAG. An ultrasonic bath provides to stabilize the dispersion during the measurements. This assures the steady coal flow preventing particles agglomeration into the syringe pump and the consequent orifice clogging.

The droplets dispersion in oxygen was fed in a properly designed burner similar to that used by Arabi-Katbi et al. (2002). The burner consist of a 40mm long Mullite Zirconia honeycomb (400CPSI, CTI s.a.) placed on the top of a 18mm ID stainless-steel tube and both to stabilize the flame and to homogeneous fed the pulverized coal. The ethanol vaporizes through the burner and acts as the flat premixed flame fuel. About 4.5g/min of 20μm agglomerated coal particles were added into the oxy-ethanol flame (~150mm/s cold gas velocity, ~0.15 equivalence ratio). The resulting coal doped flame is shown in Figure 61. The coal particles ignition causes the emission of a yellow visible light up to HAB=3mm. The choice of using a large oxygen excess was performed to optimize coal carbon content oxidation focusing on inorganic particles formation.

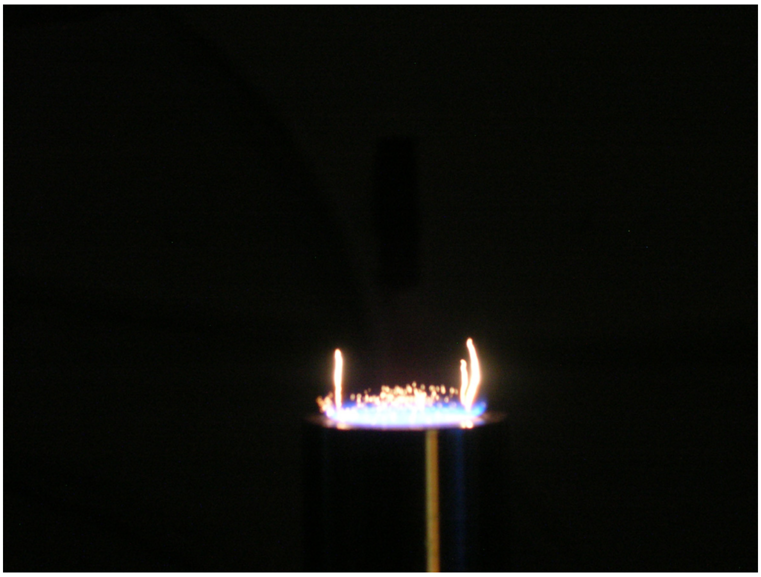

Figure 61 – A picture of the homogeneously coal doped flame.

Measurements are performed using three different bituminous coals whose proximate analysis is reported in Table 11.

Table 11 – **Used coals proximate analysis.**

	Coal-10025	Coal-10046	Coal-8556
Moisture [%]	3.11	4.90	2.20
Volatile [%]	40.20	38.31	26.76
Ashes at 750°C [%]	7.40	6.11	13.99
Fixed carbon [%]	49.29	50.68	57.64
C [%]	71.68	70.95	69.43
H [%]	5.62	5.32	4.50
N [%]	1.38	1.32	1.92
S [%]	0.53	0.40	0.44
Cl [ppm]	164.00	100.70	30.80
F [ppm]	45.30	16.10	271.00
Hg [ppm]	0.08	0.06	0.08
HHV [Kcal/Kg]	7245.25	6862.00	6724.80
LHV [Kcal/Kg]	6938.00	6560.00	6493.60

7.1 Performed analysis

Generated particles Mobility Diameter (MD) distributions are on-line measured using a dilution probe and a TapCon 3/150 DMA system equipped with a Faraday Cup Electrometer detector (Sgro et al., 2007). The measurements were performed in two DMA operative conditions with nominal MD range 0.6nm to 28nm and 2.1nm to 100nm, respectively.

Following published work, we used two horizontal tube rapid dilution probes (8mm ID, 0.5mm wall thickness) to transport and cool sampled aerosol (Kasper et al., 1997), with 0.5mm and 0.7mm orifice diameters, respectively. Earlier work examining dilution probes found that particle coagulation in the probe may significantly change the shape of the size distribution (Kasper et al. 1997, Zhao et al., 2003). The dilution ratio was controlled by both monitoring a slight underpressure in the probe, manually controlled with a rotary vane vacuum pump and adjusting the particle free dilution N_2 flow. The sample flow rate (Q_{sam}) was evaluated by scaling, with a Bernoulli approximation, the calibrated value obtained with the 0.3mm probe (Sgro et al. 2007) to account the different pinhole diameter (D_{pin}).

$$Q_{sam} = \left(\frac{D_{pin}}{0.3} \right)^2 \cdot \left(Q_{sam} \right)_{D_{pin}=0.3} \tag{7.1}$$

Dilution Ratios (DRs) around ~5000 and ~9000 were attained with the 0.7mm and 0.5mm pinhole, respectively, using 29.6lpmin dilution N_2 flow. DRs around ~3000 were also obtained with the 0.7mm pinhole decreasing the dilution flow to17.5l/min. The latter dilution was coupled with the DMA operating in the nominal MD range between 2.1nm and 100nm while the higher DRs are used with the DMA operating in the 0.6nm to 28nm range.

The particles volume fraction distribution are obtained by simply multiplying the numeric size distribution for the particles volume assuming ED=MD-0.5nm (Fernandez de la Mora, 2003).

$$\frac{dfv}{d\ln D}(MD) = \frac{\pi}{6} \cdot ED^3 \cdot \frac{dN}{d\ln D}(MD) \tag{7.2}$$

The number concentration and the volume fraction of particles in selected size ranges are calculated by integrating the measured size distribution.

Preliminary measurements were performed at HAB=50mm, corresponding to residence time of about 60ms, to assure that coal devolatilization and char matrix ignition and oxidation have completely run out.

7.2 DMA Results

The first task is to understand how many of the acquired signal can be associated to particles when the DMA operates in the nominal size range between 0.6nm and 28nm. Background measurements were performed to this aim on ambient air. The resulting size distribution is shown in Figure 62 together with one measured in the coal doped flame, not corrected for the DR.

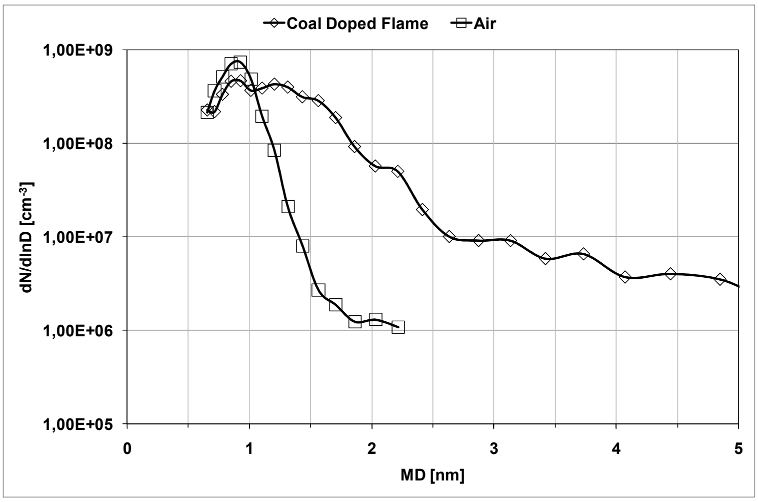

Figure 62 – DMA measured and background size distributions, Coal-10025.

The measured size distributions always show a sub-nanometer peak whose intensity decreases with the increase of larger particles number concentration. This peak is probably due to formation of molecular clusters during ionization process that transfer their charge to particles, if present (Sgro et al., 2007). The number concentration of air clusters is negligible respect to doped flame products for MD lower than 1.1nm. For this reason we will consider only the branch of size distributions with MD larger than 1.1nm to represent particles. The not considered sub-nanometer peak gives a negligible contribution to fv calculation.

When DMA operates in the 2nm to 100nm nominal range the acquired air background signal is always below the Electrometer sensitivity and could be considered to be negligible.

7.2.1 Sampling dilution effects

The DMA analyzes sampled and diluted aerosol downstream of a sampling line of 1.1m in length. Coagulation, condensation and loss of diffusive nature can occur in this probe before products reach the DMA, mainly during the dilution downstream the pinhole, altering qualitatively or quantitatively the size distribution of particles sampled in flame. The coagulation generally results in the particles size growth and number concentration reduction without changing their volume fraction. The condensation results in both particles sizes and volume fraction increase without changing their number concentration. The diffusive losses are mainly localized in the pinhole and they depends on probed aerosol flowrate in the pinhole itself and then on the DR reciprocal.

Another operating effect have to be considered when generated particles are widely polydisperse because the larger particles are in very smaller numerical concentration respect to smaller ones. The latter concentration can decrease below the DMA sensitivity when large DRs are used to prevent smaller particles coagulation.

Some representative size distribution measured at HAB=50mm using the Coal-10025 and corrected for the several used DR, are shown in Figure 63. Figure 64 report the same distribution in term of volume.

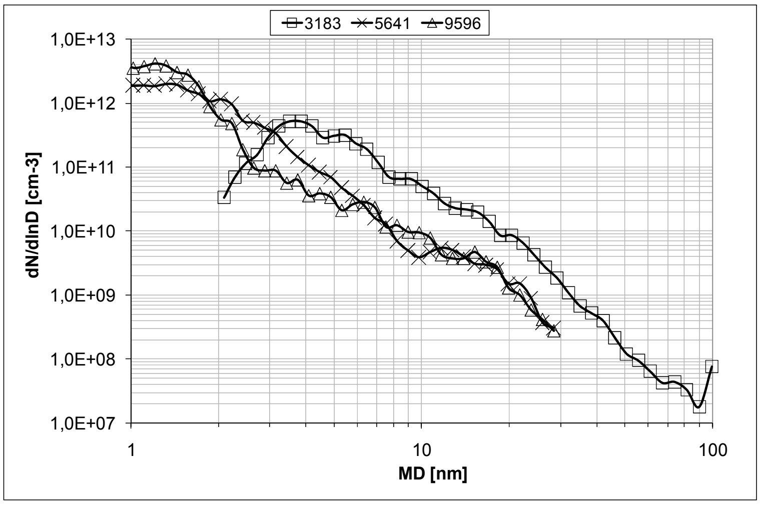

Figure 63 – DMA measured size distributions at HAB=50mm using several Dilution Ratios (□DR=3183; x DR=5641; Δ DR=9596), Coal-10025.

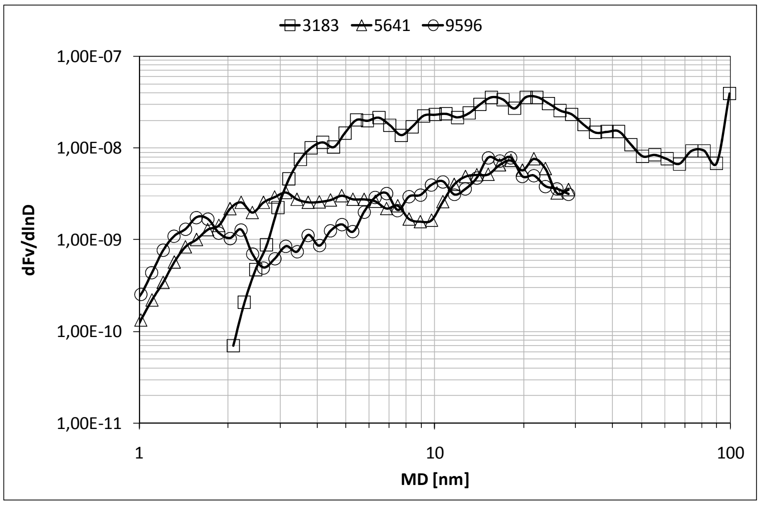

Figure 64 – Volumetric size distributions at HAB=50mm using several Dilution Ratios (□ DR=3183; Δ DR=5641; o DR=9596), Coal-10025.

It is clear in these plots that the size distribution moves towards smaller MD by increasing DR. Moreover particles larger than 30nm are not revealed using the highest DR because their number concentration decreases below the DMA sensitivity. The biggest difference among the results is observable for size smaller than 4nm while the size distribution shows almost the same profile for MD larger than 10nm. Four mode of size distribution can be recognize at about 5nm, 10nm, 20nm and 80nm while a 1.5nm mode can be observed only using the highest dilution.

To better understand the probing effect we plot, in Figure 65 and Figure 66, the particles number concentration and volume fraction versus the sampling DR, respectively. The number concentration slightly decreases with decreasing of DR because of smaller particles coagulation. Such coagulation involves the first mode disappearing with the lowest dilution. The particles volume fraction suddenly increases at the lower DR because in this case we are able to measure also particles larger than 30nm that are below the Electrometer sensitivity at higher DR. Indeed the largest particles significantly contribute to total volume fraction in spite their lower numerical concentration respect to smaller ones.

These results suggest that the highest dilution allow preventing particles coagulation but a lower dilution is required to measure the size distribution up to 100nm. It was not possible, with the used Faraday cup electrometer, to found an optimal dilution ratio to simultaneously measure the size distribution in the entire ultrafine sizes range. The use of a CNC could solve this problem.

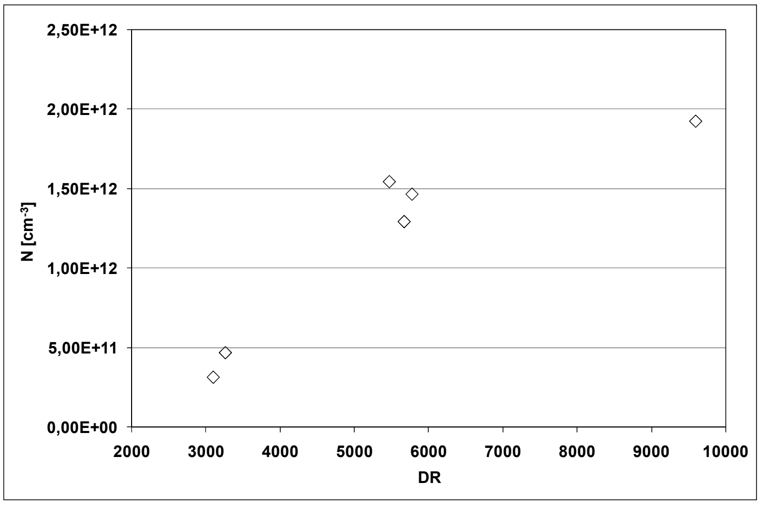

Figure 65 – Particles number concentration measured at HAB=50mm versus DR, Coal-10025.

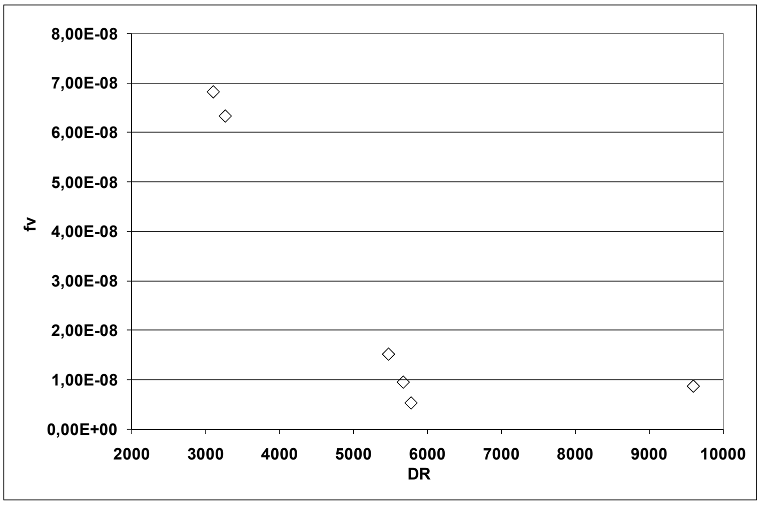

Figure 66 – Particles volume fraction measured at HAB=50mm versus DR, Coal-10025.

7.2.2 Coal type effects

On-line aerosol measurements were performed by DMA at HAB=50mm using tree different bituminous coals whose proximate analysis were shown in Table 11. The main differences among the coals are the ashes, volatile and chlorine content. The coal-10025, already examined in the previous paragraph, has the highest chlorine and volatile content while the coal 8556 is the most enriched in ashes. The coal 10045 is an intermediate one. This thesis is focused on nanoparticles smaller than 10nm and on the vaporization nucleation pathway. Thus the highest DR (~9000) is used to prevent particles coagulation in the probe despite it does not allow to detect particles larger than 30nm.

Figure 67 and Figure 68 show the numerical and volumetric size distributions, respectively. They are quite similar despite the coals differences. Three modes, at 1.5nm, 5nm and 20nm, are distinguishable in both distributions. The size distribution obtained using the coal 10025 slight differ from the others because of larger amount of particles in the size range above 3nm. This is probably due to the higher chlorine and volatile content that promote the vaporization nucleation pathway respect to the residual pathway.

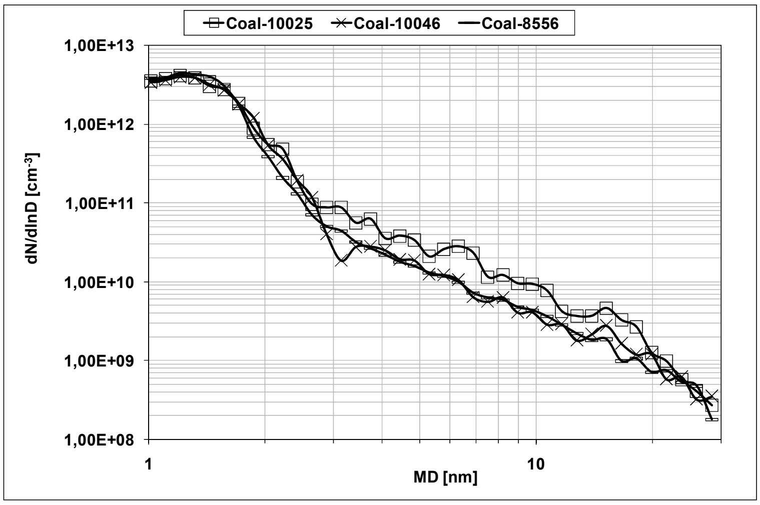

Figure 67 – DMA measured size distributions at HAB=50mm using several coals.

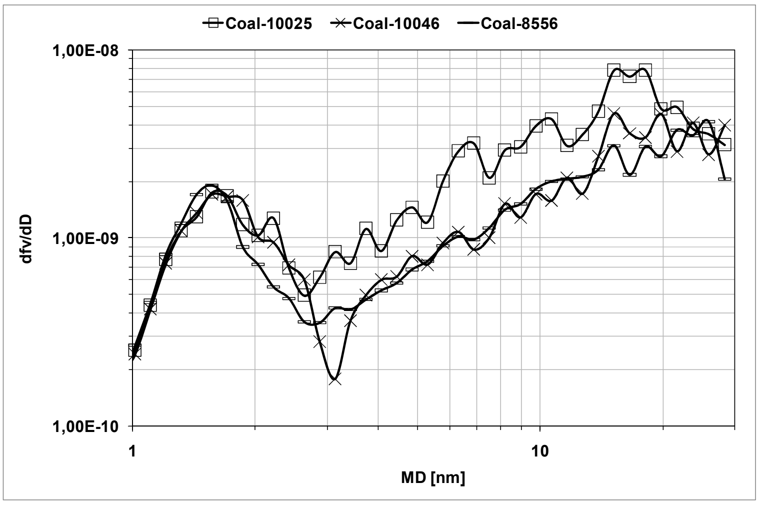

Figure 68 – Volumetric size distributions at HAB=50mm using several coals.

Unfortunately these preliminary results do not allow distinguishing the amount of matter volatile at flame temperature nucleating into the probe respect that already nucleated into the flame. In any case such matter seems to preferentially homogeneously nucleate respect to involve particles growth into the probe and probably it responsible for the smallest mode of the size distributions with modal mobility diameter of 1.5nm.

In any case the results clearly showed that the particles nucleation modes are characterized by a size distribution almost independent from the coal composition, at least in the investigated cases. The particles smaller than 5nm are the most abundant in number. Moreover they also give a not negligible contribution to total volume fraction. These results are quite interesting and require to be further studied.

Chapter 8

Conclusions

8.1 Summary and final remarks

New laboratory reactors were developed allowing to study combustion generated inorganic nanoparticles in a well controlled environment in term of temperature profile and gaseous species mixture. The reactors consist of an atmospheric pressure flat laminar premixed flame doped with real fuels or toxic metal particles precursors. Such configuration allow to investigate nanoparticles formation with in-situ or online diagnostics techniques, i.e. LLS and DMA, having much higher sensitivity to smallest particles respect that of instrumental apparatus commonly used at the exhaust of real combustors.

The incipient particles aerosol dynamic in the high temperature flame environment, can be easily followed during the first tens of milliseconds by performing measurements at several height above the burner with an approach quite similar to that widely used to study carbonaceous particles formation (Bockhorn et al. 2008) or functional metal nanoparticles synthesis in flames (Roth, 2007). Moreover the use of an extra situ technique, such as AFM, allows obtaining information on nanoparticles collection efficiency (D'Alessio et al, 2005).

Preliminary ultrafine particles size distribution measurements using an on line sampling probe high resolution DMA technique (Sgro et al., 2007) were performed in an oxy-ethanol fuel lean premixed flame doped with pulverized coals. The choice of the high oxygen excess, far from real coal combustion condition, and of the sampling point far downstream in the flame assures a complete oxidation of carbonaceous matter allowing to focus on inorganic particles. The results clearly indicate some important aspects.

- ✓ Pulverized coal combustion involves the formation of inorganic particles smaller than 10nm.
- ✓ The nanometric fraction of the generated particulate matter is by far the most abundant in term of numeric concentration.
- ✓ Nanoparticles also give a not negligible contribution to the total ultrafine particles volume fraction.
- ✓ The size distribution shape of the nucleation mode seems to be unaffected by coal chemical composition. These results indicate that the processes conducting to particles inception could be more generically studied, regardless the specific case of interest, while the characteristics of larger released particles are determined by the slower aerosol dynamic into the combustors and influenced by exhaust vapor chemical composition.

A premixed flame doped with nickel (II) nitrate aqueous solution droplets was also studied to gain more insight on the behavior of metal oxide particles of few nanometers in size, particularly to understand whether they can pose a pollution problem surviving exhaust condition. Measurements at several heights above the burner were performed with the on line sampling probe high resolution DMA and thermophoretic sampling AFM techniques. The results showed the following main characteristics.

- ✓ Almost all generated nickel oxide particles have size smaller than 10nm and they are formed very quickly in less than 2.5ms.
- ✓ The generated ~3nm monodisperse particles persist, at ~1800K, very longer than their gas kinetic half-life implying their coagulation efficiency is at least three orders of magnitude lower than unity at this temperature.
- ✓ The amount of particles thermophoretically collected on the substrates is about two order of magnitude less than that impinging on it and calculated from the on line measured numerical concentration because of very low collection efficiency.
- ✓ A collection/adhesion efficiency sudden decrease of orders of magnitude, qualitatively and quantitatively agreeing with that of carbonaceous particles

(D'Alessio et al., 2005), was observed for size smaller than 5nm comparing the extra situ and the on line measured size distributions.

- ✓ Such nickel oxide nanoparticles, once generated in a combustor, could be dispersed into the atmosphere because they have a long life-time and very low collection efficiency on filters surfaces.

Three different kind of metals nanoparticles were generated at a lower temperature (~1200K) in another premixed flame doped with lead(II) nitrate, cadmium and nickel(II) aqueous solution droplets, respectively. Extra-situ thermophoretic sampling AFM analysis and in situ LLS measurements were performed at several heights above the burner and the results reveal quite important feature of generated particles.

- ✓ Collapsing to ~4nm monodisperse particles, slowly coagulating ~2.5nm monodisperse particles and shrinking bidisperse particles are generated from the nickel, cadmium and lead-containing solutions, respectively.
- ✓ A not negligible amount of particles with sizes lower than 5nm is quickly generated in less than 20ms, regardless of the used metal salt solution.
- ✓ The nanoparticles show a lifetime much longer than the gas kinetic one because of coagulation efficiency orders of magnitude lower than unity.
- ✓ The collection efficiency on the substrates results orders of magnitude lower than unity for both three generated nanoparticles kinds.
- ✓ Both coagulation and adhesion efficiency are strongly influenced by particles size and not by their chemical nature because the observed values quantitatively agree for the three kinds of particles and with those reported in literature for carbonaceous particles (D'Alessio et al., 2005).
- ✓ Particles smaller than 5nm could survive exhaust condition and be dispersed into the atmosphere regardless of their chemical nature because both coagulation and adhesion efficiencies assume very low values.

The results obtained on both the metal salts solution droplets doped flames indicate that the nanoparticles nucleation occur inside the droplets because of their fast not uniform heating. The formation of very small nanoparticles seems to be related more on droplets heating rate than on temperature itself as results comparing the results on the two nickel (II) nitrate doped flames. It is assumed that the metal salt nucleation occur close to the droplet interface when solution reached the saturation condition. The nuclei are released into the gas before their growth or diffusion inside the droplet can occur because of the solvent fast evaporation.

The validity of this hypothesis has two main important implications and thus requires to be further studied. First of all nanoparticles inception in combustion devices could occur directly in the liquid or solid phase close to interface surfaces and not only into the gas phase trough the vaporization pathway as commonly believed.

The second aspect regards the flame synthesis of functional nanoparticles. The fast heating of metal salt solution droplets in premixed flames could be an effective and cheap method to produce nanopowder and nanocatalyst with primary particles of few nanometers in size. From this point of view the obtained preliminary SEM results on thermophoretically deposited particles seem enough encouraging.

8.2 Research perspectives

The designed reactors allow a wide spectrum of operating condition opening to study nanoparticles formation in a very detailed manner.

Regarding the particulate matter produced from real fuel, measurements will be performed on the coal doped flame at several heights above the burner to study generated particles dynamic. Moreover condition more similar to that of real coal furnaces will be realized changing the laminar flame cold gas mixture. Air and carbon dioxide oxygen mixtures will be used as oxidizing agent despite pure oxygen. Other fuels such as petrol oils will be investigated.

Regarding the solution droplets configuration other metal salts and metallorganic compounds will be used to have a more complete matrix of basic information. Binary and complex metal salts solution mixtures will be also used despite single component solution. The chlorine influence will be investigated. Moreover carbonaceous to inorganic particles interaction will be studied using slightly fuel rich premixed flames doped with metal salt solutions.

Finally more detailed analysis will be performed on collect nanopowder to verify the effectiveness of the developed doped premixed flame reactors to produce functional nanoparticles. Some attempts to dope an industrial premixed combustor will be also performed.

References

ALTMAN, I.S., AGRANOVSKI, I.E. AND CHOI, M., 2004, Physical Review E. 70, 062603.

APHEIS, 2002, *Health Impact Assessment on the Benefits of Reducing $PM_{2.5}$ in 26 European Cities*, France, APHEIS.

APHEIS, 2006, *Health Impact Assessment of Air Pollution In 26 European Cities*, France, APHEIS.

ARABI-KATBI, O.I., WEGNER, K. AND PRATSINIS, S.E., 2002, Ann. Chim. Sci. Mat. 27, 37.

BARONE, A.C., D'ALESSIO, A. AND D'ANNA, A., 2003, Combust. Flame 132, 181.

BERGLUND, R.N. AND LIU, B.Y. H., 1973, Environ. Sci. Technol. 7, 147.

BINNING, G., QUATE, C.F. AND GERBER, C., 1986, Phys. Rev. Lett. 56, 930.

BISWAS, P. AND ZACHARIAH, M.R., 1997, Environ. Sci. Technol. 31, 2455.

BOCKHORN, H., 1994, *Soot Formation in Combustion: Mechanism and Model*, Heidelberg, Springer Verlag.

BOCKHORN, H., D'ANNA, A., SAROFIM, A.F. AND WANG, H., 2008, *Combustion Generated Fine Carbonaceous Particles*, Karlsruhe, Karlsruhe University Press.

BORGHESE, A. AND MEROLA, S.S., 1998, Appl. Opt. 37, 3977.

BORHEN, C.F. AND HUFFMAN, D.R., 1983, *Absorption and Scattering of Light by Small Particles.* New York, John Wiley & Son.

BROCK J.R., 1962, J. Colloid Sci. 17, 768.

BROCKNER, W., EHRHARDT, C. AND GJIKAJ, M., 2007 Thermochimica Acta 456, 64.

BROWN, D.M., WILSON, M.L., MACNEE, W., STONE, W. AND DONALDSON, K., 2001, Toxicology and Applied Pharmacology. 175, 191.

BUCKLEY, S., SAWYER, R., KOSHLAND, C. AND LUCAS, D., 2002, Combust. Flame. 128, 435.

BURTSCHER H., MATTER, D. AND SIEGMANN, H. C., 1993, Atoms. Envir. 27, 1255.

CARBONE, F., BARONE, A.C., PAGLIARA, R., BERETTA, F., D'ANNA, A. AND D'ALESSIO, A., 2008a, Environ. Eng. Sci. in press.

CARBONE, F., BARONE, A.C., DE FILIPPO, A., BERETTA, F., D'ANNA, A. AND D'ALESSIO, A., 2008b, Chemical Engineering Transactions, 16, 87.

COMMODO, M., 2007, PhD thesis: Diagnostic for the characterization of nanometric structures in high temperature reactive systems, Napoli, Dipartimento di Ingegneria Chimica Università degli Studi di Napoli Federico II.

COVERT, D., WIEDENSOHLER, A. AND RUSSEL, R., 1997, Aerosol Sci. Technol. 27, 206.

D'ALESSIO, A., D'ANNA, A., D'ORSI, A., MINUTOLO, P., BARBELLA, R. AND CIAJOLO, A., 1992, Proc. Combust. Inst., 24, 973.

D'ALESSIO, A., D'ANNA, A., GAMBI, G. AND MINUTOLO, P., 1998, J. Aerosol Sci., 29, 397.

D'ALESSIO, A., BARONE, A.C., CAU, R., D'ANNA, A. AND MINUTOLO, P., 2005, Proc. Combust. Inst. 30, 2595.

D'ANNA, A., KURZ, M. AND MEROLA, S.S., 1998, Part. Part. Syst. Charact. 15, 237.

D'ANNA, A., VIOLI, A., D'ALESSIO, A. AND SAROFIM A. F., 2001, Combust. Flame, 127, 1995.

D'ANNA, A., 2008, *Ultrafine Particles from Combustion Sources,* Thessalonoki, European Aerosol Conference 2008 HELEXPO.

DE FILIPPO, A., 2008, PhD thesis: Caratterizzazione delle funzioni di distribuzione di nanoparticelle carboniose (1-10nm) prodotte da fiamme, motori multijet "Common Rail" e presenti in atmosfera, Napoli, Dipartimento di Ingegneria Chimica Università degli Studi di Napoli Federico II.

DOBBINS, R.A., AND MEGARIDIS C.M., 1987, Langmuir. 3, 254.

DOBBINS, R.A. AND SUBRAMANIASIVAM , H., 1994, *Soot Precursor Particles in Flames*, Heidelberg, Springer Verlag.

EHRMAN, S.H. AND FRIEDLANDER, S.K., 1999, Aerosol Sci. Tech. 30, 259.

EPA, 2004, The Particle Pollution Report Current Understanding of Air Quality and Emissions through 2003, North Carolina, U.S. Environmental Protection Agency.

EPSTEIN, P.S., 1929, Z Physik. 54, 537.

FENNELL, P.S., DENNIS, J.S. AND HAYHURST, A.N., 2007, Proc. Combust. Inst. 31, 1939.

FENNELL, P.S., DENNIS, J.S. AND HAYHURST, A.N., 2007, Combust. Flame 151, 560.

FERNANDEZ DE LA MORA, J., DE JUAN, L., EICHLER, T. AND ROSSEL, J., 1998, Trends in Anal. Chem. 17, 328.

FERNADEZ DE LA MORA, J.J., DE JUAN, L.L., LIEDTKE, K. AND SCHMIDT-OTT, A., 2003, J. Aerosol Sci. 34, 79.

FLAGAN, R.C. AND FRIEDLANDER, S.K., 1978, *Recent Developments in Aerosol Science*, New York, John Wiley & Son.

FRIEDLANDER, S.K. AND WANG, 1966, J. Colloid. Interface Sci. 22, 126.

FRIEDLANDER, S. K., 1977, *Smoke, Dust and Haze*, New York, John Wiley & Son.

FRIEDBACHER, G. AND GRASSERBAUER, M., 1995, J.Anal.Chem. 67(10), 1749.

FUCHS, N.A., 1964, *The Mechanics of Aerosol*, New York, Pergamon Press.

FUCHS, N. A. AND SUTUGIN, A. G., 1971, *Topics in current aerosol research*, New York, Pergamon Press.

GAY, J. G. AND BERNE, B. J., 1986, J. Colloid Interface Sci. 109, 90.

GELBARD,F. AND SEINFEILD, J.H., 1980, J. Colloid Interface Sci. 78, 485.

HAMAKER, H. C., 1937, Physica IV 10, 1058.

HARRIS AND S. J. E KENNEDY, I. M., 1988, Comb. Sci. and Tech. 59, 443.

HAYNES, B.S. AND WAGNER, H. GG., 1981, Prog. Energy Combust. Sci. 7,229.

HELBLE, J. J. AND SAROFIM, A. F.,1989, J. Colloid Interface Sci. 128, 348.

HELBLE, J. J., 1998, J. Aerosol Sci. 29, 721.

HINDS, W. C., 1999, *Aerosol Technology: Properties,Behavior and Measurement of Airborne Particles*, New York, John Wiley & Son.

KANG, S.G., HELBLE, J.J. SAROFIM, A.F. AND BÉER, J.M., 1988, Proc. Combust. Inst. 22, 231.

KASPER, M., SIEGMANN, K. AND SATTLER, K., 1997, J. Aerosol Sci. 28, 1569.

KELLY, R. AND PADLEY, P.J., 1967, Nature. 216, 258.

KENNEDY, I.M., 2007, Proc. Combust. Inst. 31, 2757.

KOLLENSPERGER, G., FRIEDBACHER, G., GRASSERBAUER, M. AND DORFFNER, L., 1997, Fresenius J. Anal. Chem., 358(1-2), 268.

KÖLLENSPERGER, G., FRIEDBACHER, G., KRAMMER, A. AND GRASSERBAUER, M., 1999, J. Fresenius Anal. Chem. 363, 323.

KOYLU, U.O., MCENALLY, C.S., ROSNER, D.E. AND PFEFFERLE, L.D., 1997, Combust. Flame 110, 494.

KURZ, M., D'ANNA, A., D'ALESSIO A., MEROLA, S.S AND BORGHESE A., 1999, Part. Part. Syst. Charact. 16, 77.

KURZ, M., D'ANNA, A., D'ALESSIO, A., MEROLA, S.S. AND BORGHESE, A., 1999, 6th International Congress on Toxic Combustion By Products, Karlsruhe, Germany.

JACOBSON, M.Z., 2001, Nature. 409, 695.

LANOTTE, L., AUSANIO, G., BARONE, A.C., HISON, C., IANNOTTI, V., AMORUSO, S., BRUZZESE, R., VITIELLO, M., D'INCAU, M. AND SCARDI, P., 2006, J. Opt. Adv. Mater. 8, 1672.

LEE, D., MILLER, A., KITTELSON, D. AND ZACHARIAH, M.R., 2006, J. Aerosol Sci. 37, 88.

LIGHTY, S., VERANTH, J.M. AND SAROFIM, A.F., 2000, J. Air & Waste Manage. Assoc. 50, 1565.

LIMAYE, A.U. AND HELBLE, J.J., 2002, J. Am. Ceram. Soc. 85, 1127.

LINAK, W.P. AND WENDT, J.O.L., 1993, Prog. Energy Combust. Sci. 19, 145.

LINAK, W.P., ZHU, W., WENDT, J.O.L., HUGGINS, F.E., CHEN, Y., SHAH, N., HUFFMAN, G.P. AND GILMOUR, M.I., 2007, Proc. Combust. Inst. 31, 1929.

MADLER, R., KAMMLER, H.K., MUELLER, R. AND PRATSINIS, S.E., 2002, J. Aerosol Sci 33, 369.

MAKELA, J.M., RIHELA, M., UKKONEN, A., JOKINEN, T. AND KESKINEN, J., 1996, J. Chem. Physics. 105, 1562.

MEROLA, S.S., KURZ, M., BORGHESE, A., D'ANNA, A. AND D'ALESSIO, A., 1998, Combust. Sci. Tech. 134, 221.

MILLER, J. AND MELIUS, H., 1992, Combust. Flame 91, 21.

MILLIKAN R.A., 1923, Phys. Chem. 22, 1.

MULHOLLAND, J.A. AND SAROFIM, A.F., 1991, Environ. Sci. Technol. 25, 268.

OBERDORSTER, G., SHARP, Z., ATUDOREI, V., ELDER, A., GELEIN, R., LUNTS, A., KREYLING, W. AND COX, C., 2002, J. Toxic Env. Health. 65, 1531.

OBERDORSTER, G., OBERDORSTER, E. AND OBERDORSTER, J., 2005, J. Environ. Health Perspectives 113, 823.

OXTOBY, D.W., 1992, J. Phys. Condens. Matter. 4,7627.

PARK, C., APPLETON, J.P., 1973, Combust. Flame, 20, 369.

PARK, S.H., LEE, K.W., OTTO, E. AND FISSAN, F., 1999, J. Aeros. Sci. 30, 3.

PRATSINIS, S.E.,1998, Prog. Energy Combust. Sci. 19, 145.

QUANN, R.J. AND SAROFIM, A.F., 1982, Proc. Combust. Inst. 19, 1429.

RAMIREZ-AGUILAR, K.A., LEHMPUHL, D.W., MICHEL, A.E., BIRKS, J.W. AND ROWLEN, K.L., 1999, Ultramicroscopy. 77,187.

RAYLEIGH, J. W. S., 1879, Prof. Roy. Soc. 29, 7.

ROSNER, D.E. AND KHALIL Y.F., 2000, J. Aeros. Sci. 31(3), 273.

ROSNER, D.E, 2005, Ind. Eng. Chem. Res. 44, 6045.

ROTH, P. , 2007, Proc. Combust. Inst. 31, 1773.

SAROFIM, A.F., HOWARD, J.B. AND PADIA, A.S., 1977, Combust. Sci. Technol., 16, 187.

SEAMES, W.S. AND WENDT, J.O.L., 2000, Fuel Process. Technol. 63, 179.

SEINFELD, J.H. AND PANDIS, S.N., 1998, *Atmospheric Chemistry and Physics: From Air Pollution to Climate Change.* New York, John Wiley & Son.

SGRO., L.A., BASILE, G., BARONE, A.C., D'ANNA, A., MINUTOLO, P., BORGHESE, A. AND D'ALESSIO, A., 2003, Chemosphere. 51(10), 1079.

SGRO, L.A., DE FILIPPO, A., LANZUOLO G. AND D'ALESSIO, A., 2007, Proc. Combust. Inst. 31, 631.

SMOLUCHOWSKI, M.V., 1917, Z. *Phys. Chem. 92*, 129.

STARK, W.J. AND PRATSINIS, S.E., 2002, Powder Technol. 126, 103.

STERN, K. H., 1972, J. Phys. Chem. Ref. Data 1, 747.

SIEGMANN, K., HEPP, H. AND SATTLER, K., 1995, Comb. Sci. Technol. 109, 165.

TALBOT, L., 1980, *Proc.12th Int.Symp. on Rarefied Gasdynamics*, Washington D.C., AIAA Publishers.

TAMMET, H., 1995, J. Aeros. Sci. 26, 459.

TOGNOTTI, L., LONGWELL, J.P. AND SAROFIM, A.F., 1991a, Proc. Combust. Inst. 23, 1207.

TOGNOTTI, L., STEPHANOPOULO, M.F. AND SAROFIM, A.F., 1991b, Environ. Sci. Technol. 25, 104.

TSI INCORPORATED, 2002, Model 3450 Vibrating Orifice Aerosol Generator - Instruction Manual, Shoreview, TSI Incorporated.

ULRICH, G.D., 1984, Chem. and Engr. News. August 6, 22.

WALDMANN, L., AND SCHMITT, K.H., 1966, *Aerosol Science.* London, Academic Press.

WIINIKKA, H., GEBART, R., BOMAN, C., BOSTRÖM, D., NORDIN, A. AND ÖHMAN, 2006, Combust. Flame. 147, 278.

WOJCIECHOWSKI, K. T. AND MALECKI, A., 1999, Thermochimica Acta 331, 73.

WOOLDRIDGE, M.S., 1998, Prog. Energy Combust. Sci., 24, 63.

YU S., JONES, A.D., CHANG, D.P.Y., KELLY, P.B. AND KENNEDY, I.M., 1998, Proc. Combust. Inst. 27, 1639.

ZHAO, B., YANG, Z., JOHNSTON, M.V., WANG, H., WEXLER, A. S., BALTHASAR, M. AND KRAFT, M., 2003a, Combustion and Flame 133, 173.

ZHAO, B., YANG, Z., WANG, J., JOHNSTON, M.V. AND WANG, H., 2003b, Aerosol Sci. Technol. 37, 611.

ZHAO, B., UCHIKAWA, K., MCCORMICK, J. R., NI, C. Y., CHEN, J. G. AND WANG, H., 2005, Proc. Combust. Inst. 30, 2569.

ZHAO, B., UCHIKAWA, K. AND WANG, H., 2007, Proc. Combust. Inst. 31, 851.

ZHENG, F., 2002, Advances in Colloid and Interface Science. 97, 255.

ZHUANG, Y., KIM, Y. J., LEE, T.G. AND BISWAS, P., 2000, Journal of Electrostatics 48, 245.

List of Papers associated to the Thesis

PUBLICATIONS:

CARBONE, F., BARONE, A.C., PAGLIARA, R., BERETTA, F., D'ANNA, A. AND D'ALESSIO, A., 2008a, *Ultrafine Particles Formed by Heating Droplets of Simulated Ash Containing Metals*, Environ. Eng. Sci. in press.

CARBONE, F., BARONE, A.C., DE FILIPPO, A., BERETTA, F., D'ANNA, A. AND D'ALESSIO, A., 2008b, *Coagulation and Adhesion of Nanoparticles generated in flame from droplets of Nickel Nitrate aqueous solutions*, Chemical Engineering Transactions, 16, 87.

CONFERENCES:

CARBONE, F., BARONE, A.C., PAGLIARA, R., BERETTA, F., D'ANNA, A. AND D'ALESSIO, A., *Ultrafine Particles formed by Heating-up of droplets of simulated Ash containing Metals*, 10th International Congress on Combustion by-Products and their Health Effects, 17-20 June, Ischia, Italy.

CARBONE, F., BARONE, A.C., PAGLIARA, R., BERETTA, F., D'ANNA, A. AND D'ALESSIO, A., *Flame Engineered Nanoparticles from Metal Salt Solutions*, XXX Meeting on Combustion of Italian Section of Combustion Institute, 20-23 Giugno 2007, Ischia, Italy.

CARBONE, F., BARONE, R., BERETTA, F., D'ANNA, A. AND D'ALESSIO, A., *Size Distributions of Nanoparticles Generated from Droplets of Metal Nitrate Aqueous Solutions in Combustion*, XXI Combustion Meeting of Italian Section of Combustion Institute, 17-20 Giugno 2008, Torino, Italy

CARBONE, F., BARONE, R., BERETTA, F., D'ANNA, A. AND D'ALESSIO, A., *Size Distributions of Nanoparticles Generated from Droplets of Metal Nitrate Aqueous Solutions in Combustion Environments*, 32nd Symposium on Combustion of The Combustion Institute, 3-8 Agosto 2008, McGill University, Montreal, Canada.

CARBONE, F., BARONE, A.C., DE FILIPPO, A., BERETTA, F., D'ANNA, A. AND D'ALESSIO, A., *Coagulation and Adhesion of Nanoparticles generated in flame from droplets of Nickel Nitrate aqueous solutions*, 2nd Advanced Atmospheric Aerosol Symposium AAAS 2008, 9-12 Novembre 2008, Napoli.